ABSTRACT

GRANT, BRANDON PAUL. Exploring Renewable Wave Energy in North Carolina and its Impact on Coastal Processes. (Under the direction of Dr. Billy L. Edge).

The State of North Carolina is actively pursuing sources of renewable energy. Given North Carolina's location on the eastern seaboard, wave energy can be utilized. Many devices have been developed using many different techniques to transfer the wave motion into grid ready energy. This study will first examine the different technologies available for two specific categories of wave energy converters (WECs). This analysis will lead to identifying the technology that would best fit the North Carolina coast. This study found that the nearshore surge device would be the technology that best suits North Carolina. For North Carolina to implement wave energy as a viable source, an accurate representation of the resource must be made. Jennette's pier, which is located in Nags Head, has been identified as a test location for WECs. The next section of this study identified the wave energy resource by examining the historical wave record from two main sources; the US Army Corps of Engineers (USACE) wave buoys and the Wave Information Studies (WIS) hindcasting model. The buoy data was used to describe the wave climate at the testing site and determine seasonal effects. The distribution of wave power along the North Carolina coast was calculated using the WIS data. The total yearly power was found to be 0.110 GW-hr/m/year at the testing location. Finally, the nearshore wave model, SWAN (Simulating WAves Nearshore), was used to analyze any shoreline change that might be caused by an array of WECs deployed offshore at Jennette's Pier. This WEC array will be modeled in SWAN as a group of obstacles with a given transmission coefficient for each device. To show the impact on coastal processes, three different wave conditions were used to analyze the influence on

significant wave height, longshore current, and longshore transport due to the WEC array. The effects from the WEC array were found to be localized to the region behind the array and dependent on the size of the array, proximity to shore, transmission coefficient assigned, and the incident wave angle.

Exploring Renewable Wave Energy in North Carolina and its Impact on Coastal Processes

by
Brandon Paul Grant

A thesis submitted to the Graduate Faculty of
North Carolina State University
in partial fulfillment of the
requirements for the degree of
Master of Science

Civil Engineering

Raleigh, North Carolina

2012

APPROVED BY:

_____	_____
Dr. Billy L. Edge Committee Chair	Dr. Margery F. Overton
_____	
Dr. Helena Mitasova	

BIOGRAPHY

Brandon was born and raised in Jacksonville, Florida where his parents instilled in him the love of water from an early age when he lived aboard a boat until the age of four. He completed his undergraduate studies in December of 2009 in Civil Engineering with an emphasis in water resources at the University of Florida. From there, He and his wife moved to North Carolina to start his master's degree at NC State in Civil Engineering with an emphasis in Coastal Engineering. His advisor welcomed him into the program and made the transition from Florida very smooth.

ACKNOWLEDGMENTS

First of all I would like to thank my advisor, Dr. Billy Edge, for his guidance and encouragement throughout my time here at NC State. It has been an honor working with him on such an emerging and fascinating topic over the past few years. I would also like to thank Dr. Margery Overton and Dr. Helena Mitasova for their continued support through my studies and imparting their extensive knowledge of the coastal realm to me.

Next, I would like to thank my amazing wife for her sacrificial love and encouragement throughout this process. This has been a long road and I could not have done it without her by my side. To my loving parents and in-laws, I greatly appreciate all of the encouragement they gave me to make this thesis a reality. Also to my friends and colleagues: Adam Clinch, Qiang Jin, Onur Kurum, Ross Oliver, and Nick Spore in the office, for their insight and making the long weekends in the office manageable especially on game day.

TABLE OF CONTENTS

LIST OF TABLES

LIST OF FIGURES

CHAPTER 1: Wave Energy Converters

1.1 Introduction

In recent history, there has been an emphasis on seeking out sources of renewable energy. Given North Carolina's position on the eastern seaboard, it is in a prime location to explore wave energy. Devices have been developed to optimize energy extraction by examining the basic principles of wave motion. The European Marine Energy Centre (EMEC), located in Orkney, Scotland has recorded 147 different wave energy devices (European Marine Energy Centre, 2012). EMEC is one of the lead testing centers for full scale wave energy converters in the world. Most devices are site specific; therefore, there is not one device that will work for every location. Three main technologies that were reviewed include the attenuator and the heave and surge point absorbers. Of the 147 devices recorded by EMEC worldwide, 53 are heave point absorbers, 8 are surge point absorbers, and 30 are attenuators. Each of these devices interacts differently with the passing ocean waves and therefore their optimal working environment will vary.

Jennette's pier in Nags Head, North Carolina has been identified as a testing site for WECs. A thorough analysis of most of the available technologies has been made by Falcao (2010). This study will exam the attenuator and point absorber and identify a specific technology that is most applicable to this specific location on the Outer Banks.

1.2 Classification of Wave Energy Converters

1.2.1 Attenuator

An attenuator is a floating device that is made up of two or more sections that pivot with the passing waves. This is a type of oscillating-body system that depends on the relative rotation of the bodies for energy conversion (Falcao, 2010). This type of device essentially rides the wave and at the joint of each body there are pistons which harness the pivoting motion of the device to drive the power take off (PTO) system. The optimal orientation would be perpendicular to the wave crest. If the waves were coming in at an angle relative to the device, then the device would need to be adjusted to maximize its energy capture. With this type of motion needing to be captured, the driving wave parameter is the steepness. These devices will be joined together to create a farm, where each device will be slack moored to enable free motion without drifting away. The electricity generated from the devices will be transmitted to the shore via subsea cables. The Pelamis device, shown below in Figure I-2.1, is one example of a successful design of an attenuator WEC. It has completed a one year full scale sea trial at EMEC's Billia Croo wave test site where it successfully provided electricity to the national grid.

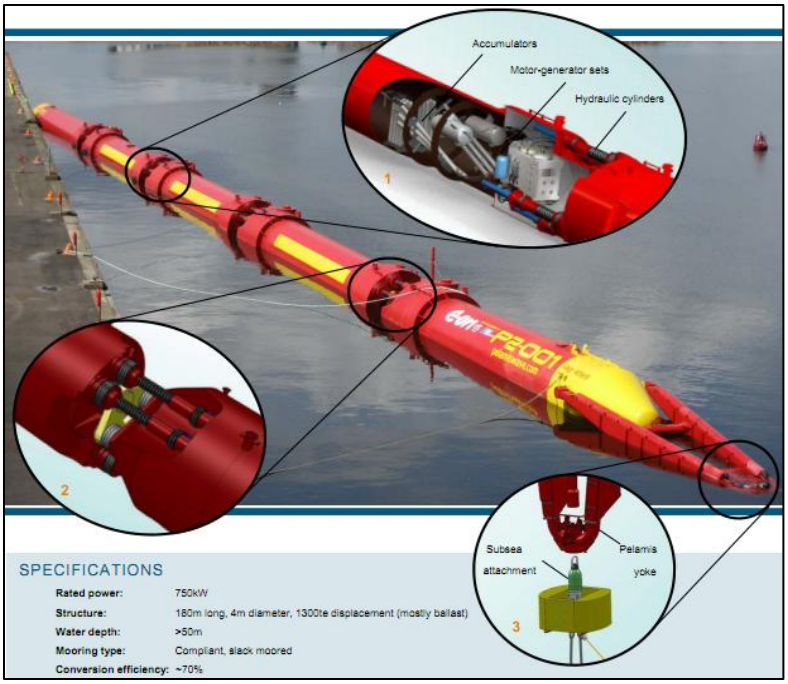

Figure I-2.1: P2 Wave Energy converter (Pelamis Wave Power, 2012)

The Pelamis P2 device measures 180 meters long with five sections, each four meters in diameter. At each of these four joints, there is a power module which houses the hydraulic PTO system. This system uses the wave driven articulation of the device to pump fluid into hydraulic accumulators which store the high pressure fluid (Pelamis Wave Power, 2012). The accumulator allows for a consistent release of the fluid through a hydraulic motor which powers a generator to create electricity. Each device has a peak power rating of 750 kilowatts. The joints at each section allow for two degrees of freedom which captures the up and down as well as the side to side pivoting of the device which is shown in Figure I-2.2.

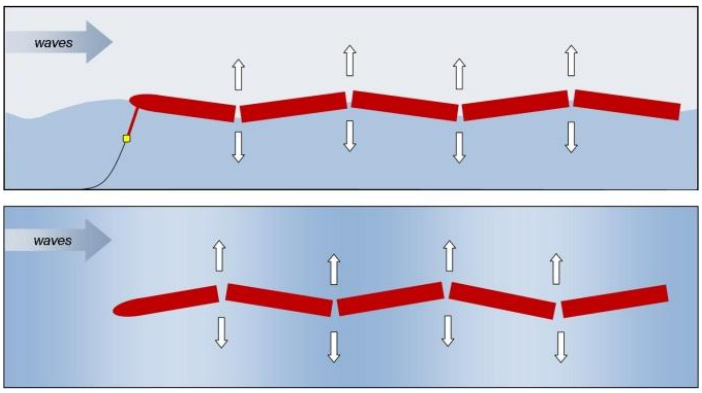

Figure I-2.2: Pelamis Motion: 2 Degrees of Freedom (Pelamis Wave Power, 2012)

The Pelamis device claims a conversion efficiency of 70% (Pelamis Wave Power, 2012). The deployment depth required for this device is greater than 50 meters and the typical site footprint can vary between 1-2 km^2 depending on the number of devices deployed.

1.2.2 Point Absorber

A point absorber describes a device whose width is relatively smaller than the passing wave length (Falcao, 2010). These devices focus on transferring the fundamental particle motion of waves into usable mechanical motion to generate electricity. Linear wave theory describes a progressive wave in which the water particles move in an elliptical orbit which can be broken down into the horizontal and vertical components (Dean & Dalrymple, 2002). A point absorber will focus on one of these components and therefore can be broken down into the following two sub categories; Heave devices, which focus on the vertical motion, and Surge devices, which focus on the horizontal motion.

1.2.2.1 Heave

A heave device utilizes a float to capture the vertical motion of passing waves. Unlike the attenuator device, heave devices are not dependent on wave direction. This is advantageous given the random nature of ocean waves. The most simple heave device utilizes a single body system where the float oscillates along a support which is fixed to the ocean floor (Falcao, 2010). Currently, the majority of heave devices incorporate the two body system. The two bodies that make up this system are a float and a submerged body. The basic principle of this system is that energy is captured in the heave direction from the relative motion of the two bodies (Falcao, 2010). This motion is then used to drive a PTO system similarly to the attenuator, or drive a linear electric generator. Then the electricity is transferred to shore via subsea cables. In order to obtain maximum power absorption from this system, the two bodies should work near resonance (van den Berg, Ricci, Santos, Rico, & Lopez, 2010). One company that has had success with the two body heave device is Ocean Power Technologies (OPT). Their PowerBuoy 150 (PB150), shown below in Figure I-2.3, is a second generation device which has a peak power rating of 150 kilowatts (Ocean Power Technologies, 2012).

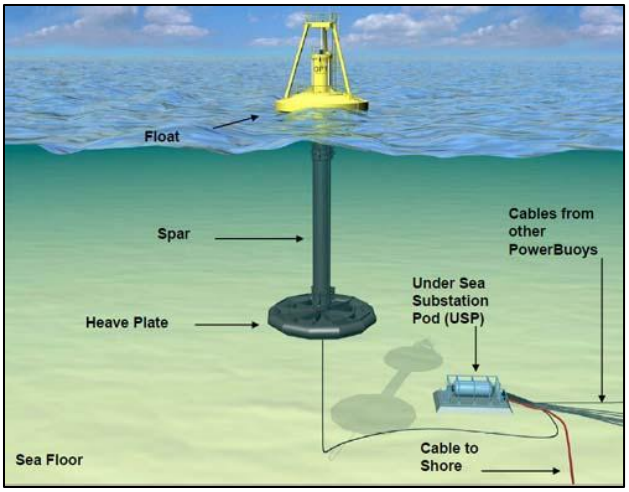

Figure I-2.3: Ocean Power Technologies Power Buoy Wave Energy Converter (Ocean Power Technologies, 2012)

OPT claims that the PB150 has a typical capacity factor, which is the ratio of actual power output to peak rated power output, which ranges between 30% and 45% (Ocean Power Technologies, 2012). The dimensions of the device are 44 meters tall, with 35 below the water surface and 9 meters above the water surface, 11 meters in diameter at the float, and 14 meters in diameter at the submerged heave plate. The power generated from this device is transmitted to the Underwater Substation Pod (USP), which can accommodate up to ten devices, then transmitted to shore via subsea cables. The required wave height and depth for the PB150 to produce power is between 1.5 and 7 meters and between 30 and 50 meters respectively. The PB150 underwent successful ocean trials at off the coast of Santoña, Spain in July of 2006 and at the Billia Croo site at EMEC in April 2011. The PB150 exceeded expectations in its ocean trials in Scotland. Power generation peaked above the 150 kilowatts rating exceeding 400 kilowatts during storm events (Ocean Power Technologies, 2012). When wave heights decreased to 2 meters, the PB150 produced on average 45 kilowatts

power production, which shows the grid connection capabilities of this device (Ocean Power Technologies, 2012). Currently OPT is developing its third generation device, the PowerTower (PB500), which has a peak power rating of 500 kilowatts and should be complete in 2013.

1.2.2.2 Surge

A surge WEC is a submerged device that harnesses the horizontal motion of the wave, which is converted into electricity. The motion of this type of device is very similar to the motion of a pendulum. The base of the device is anchored to the seafloor and a flap oscillates back and forth capturing the surge motion of the wave. These types of devices are designed to operate in the shallow water region. In shallow water, the wave orbitals are elliptical in shape and the horizontal displacement of the water particle changes little with depth (Dean & Dalrymple, 1991). These devices were designed around this concept.

One successful design that utilized the surge motion of the waves was the Oyster, which was developed by Aquamarine Power shown in Figure I-2.3 below.

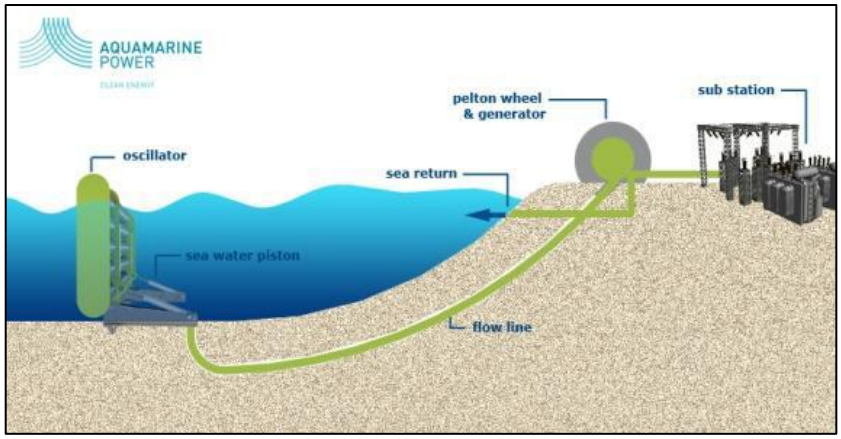

Figure I-2.4: Aquamarine Power Oyster Wave Energy Converter (Whittaker, et al., 2005)

The Oyster utilizes a unique technology which consists of a buoyant flap that when oscillated will compress a hydraulic cylinder that drives high pressure sea water to shore via a directional bored flow line (Whittaker, et al., 2005). When the pressurized water reaches shore, it powers a Pelton wheel turbine generator (Whittaker, et al., 2005). This flow is regulated by hydraulic accumulators, an adjustable valve, and a flywheel to produce a consistent electrical output to allow for grid connection (Whittaker, et al., 2005). The dimensions of the third generation Oyster 800 consist of a 26 meter wide by 12 meter tall flap that should be installed in water depths between 10 and 15 meters. The Oyster 800 has a peak power rating of 800 kilowatts. Previous models of the Oyster have undergone over 6000 hours of ocean trials at multiple testing locations including the Billia Croo site at EMEC. In August of 2011, the Oyster 800 was deployed for installation at the Billia Croo site at EMEC to undergo its first set of ocean trials.

Another example of a surge WEC is the Waveroller developed by AW-Energy shown in Figure I-2.4 below.

Figure I-2.5: AW-Energy WaveRoller Wave Energy Converter (AW-Energy, 2012)

This device works in a similar manner as the oyster in that it is a bottom mounted pivoting flap; however, there are three flaps attached to one mounting plate and the plate is completely submerged. The motion of the flaps drives a piston pump and a hydraulic motor/generator combination to produce electricity (AW-Energy, 2012). The power rating for each plate is 300 kilowatts, where each flap produces 100 kilowatts. This device has undergone multiple laboratory and sea trials at EMEC. As of August 11, 2012, the first WaveRoller power plant was deployed near Peniche, Portugal (AW-Energy, 2012). The power plant consists of 3 WaveRoller devices which are currently operational and connected to the Portuguese national grid via sub-sea cables.

Resolute Marine Energy (RME) is another company that has developed a surge device. RME completed its first round of ocean tests on their SurgeWEC device at Jennette's pier in December of 2011, as shown in Figure I-2.5 below.

Figure I-2.6: Resolute Marine Energy SurgeWEC Deployment at Jennette's Pier in Nags Head, NC (Coastal Studies Institute, 2012)

They are currently planning another round of ocean tests off the coast of Nantucket Island. RME participated in the South African trade mission in hopes to use this technology to power desalinization plants for coastal communities in South Africa (Resolute Marine Energy, 2012).

1.3 Application for North Carolina

North Carolina has approximately 510 kilometers of ocean shoreline. The northern section of North Carolina from Cape Lookout to the Virginia boarder is known for having higher

wave activity. Further discussion on this activity will come in the following chapter. One of the major factors that limit the applicable devices to a specific site is the bathymetry. Figure I-3.1 shows the bathymetry throughout this section.

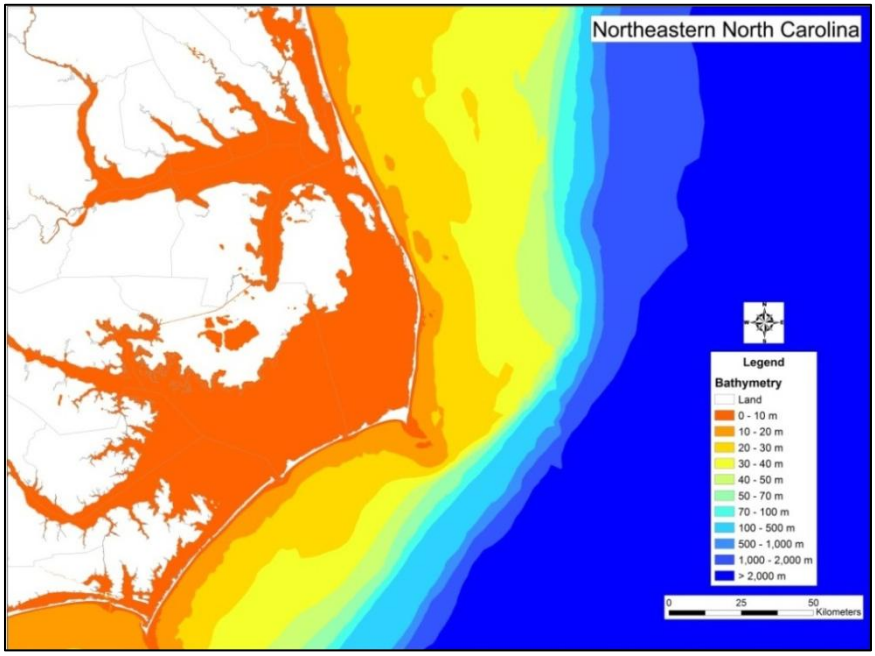

Figure I-3.1: Northeaster North Carolina Bathymetry

There is a very mild slope directly offshore out to the 50 meter contour. This contour is closest to the shoreline approximately 22.5 kilometers off of Cape Hatteras. At the site of interest in Nags Head, the 50 meter contour is approximately 56.5 kilometers offshore. Given that both the PowerBouy and Pelamis devices require a depth of 50 meters or greater for deployment, and the Pelamis device recommends a deployment distance offshore between 2 and 10 kilometers, these devices would not be feasible for North Carolina to pursue in their present form. WECs deployed in deeper water would have access to a more energetic wave climate; however, this would pose higher costs in other areas. It has been

shown by Folley et al. (2007) that the change in the amount of exploitable wave energy from deep water to the nearshore was typically between 5% and 10% and not 20% as was thought previously. The exploitable wave energy resource is thought to represent the amount of wave energy that is extractable by WECs more accurately than the omni-directional wave energy resource (Folley & Whittaker, 2009). A location closer to shore would reduce the cost of equipment for the transmission of power back to shore, as well as reduce the power losses in the cable in the transmission (Folley, Whittaker, & Henry, 2005). A device located nearshore would reduce the travel time for installation and maintenance, which would reduce the cost and increase plant availability (Folley, Whittaker, & Henry, 2005). This could be a significant advantage with operation and maintenance costs accounting for 40% of the net cost of a WEC (The Royal Academy of Engineering, 2004).

The technology that best suits North Carolina's coast is the nearshore surge device because of the shallow sloping bathymetry. Another advantage to the nearshore device is that larger waves will break which reduces the maximum loads required for survival (Folley, Whittaker, & Henry, 2005). If there were a large storm event with the WEC located within the breaking zone, the device would go into survival mode and not harness any energy. Also, from Snell's Law, wave crests become more parallel to the bottom contours as they propagate onshore due to the refraction process. The maximum efficiency of a power absorbing body was defined by Evans (1976) as the proportion of the available power per unit frontage of the incident wave. Installing the surge devices parallel with the bottom contours will allow for maximum energy capture and for minimal adjustment to device orientation while maintaining

maximum efficiencies. Many other types of devices require monitoring and adjusting to account for the change in wave angle.

CHAPTER 2: North Carolina Wave Energy Resource

2.1 Introduction

For North Carolina to implement wave energy as a viable source of renewable energy, an accurate representation of the resource must be made. An assessment of the wave energy resource is a basic prerequisite for the strategic planning of its utilization and for the design of wave energy devices (Falcao, 2010). The Electric Power Research Institute (EPRI) notes three characteristics of waves that are of importance when seeking to pursue wave energy, which are power density, intermittency, and predictability (Bedard, et al., 2005). Understanding the historical wave climate will give an accurate assessment of the available resource. The wave climate will be identified by examining the historical wave record from two main sources: The United States Army Corps of Engineers (USACE) wave buoys and Wave Information Studies (WIS) hindcasting model. The USACE Field Research Facility (FRF), located in Duck, North Carolina, has deployed wave gages at multiple locations along the North Carolina coast. Two locations of interest for this study are at the FRF and at Jennette's Pier in Nags Head, North Carolina. These two gages were used to describe the average historical wave parameters, including energy based wave height (H_{mo}), peak period (T_p), and mean wave direction, at each location. These parameters were then compared at the two locations to determine a correlation. The buoy data was then analyzed to show any form of intermittency or seasonality. The WIS project generates wave parameters from historical wind fields. This data was used to calculate the wave power density throughout the northern section of the North Carolina Outer Banks from Cape Fear in the south, to the North Carolina

Virginia boarder. From the EPRI report, wave energy predictability is done on the order of a few days (Bedard, et al., 2005).

2.2 Wave Climate Analysis

2.2.1 Data Source

The FRF buoy at Duck is located 34 kilometers northwest of the Jennette's Pier Acoustic Wave And Current (AWAC) profiler. The Jennette's pier AWAC is of importance due to its proximity to the Pier, which has been identified as a testing facility for WEC devices. An accurate description of the wave climate at a testing location is important to the developers of these devices. The Jennette's Pier AWAC is located in a depth of 11.3 meters whereas the Waverider 630 is in a depth of 17.4 meters. The coordinates of these two sites used in this analysis are shown in Table II-2.1.

Table II-2.1: USACE FRF wave buoy locations and depth

Source	Station ID	Latitude	Longitude	Depth (m)
FRF	Jennette's Pier AWAC	35°54.740' N	75°35.205 W	11.3
FRF	Waverider 630	36°11.993' N	75°42.843 W	17.4

The wave record at the Waverider 630 buoy has an extensive history dating back to 1987. From 1987 to 1996 the buoy only measured energy based wave height and peak period on an hourly basis. The buoy was replaced in November 1996 with an updated version, which included the measurement of wave direction. These parameters are based on a frequency analysis of the measured wave spectrum. Assuming the wave height distribution follows a

Rayleigh distribution, the wave height can be computed from the zero moment (m_0) of the wave spectrum (Kamphuis, 2010). The zero moment is found by calculating the area under the spectrum curve given by:

$$m_0 = \int_{f=0}^{f=\infty} S(f)df \tag{2.1}$$

where $S(f)$ is the wave variance spectral density. The energy based wave height can then be found by:

$$H_{m0} = 4\sqrt{m_0} \tag{2.2}$$

The peak wave period (T_p) is the period that is associated with the peak of the energy spectrum curve. The mean wave direction is measured as the direction of wave propagation with respect to true north. The Jennette's pier AWAC was deployed from 2008 to 2010. Figure II-2.1 shows the spatial relationship of the Waverider 630 to the Jennette's Pier AWAC with respect to water depth.

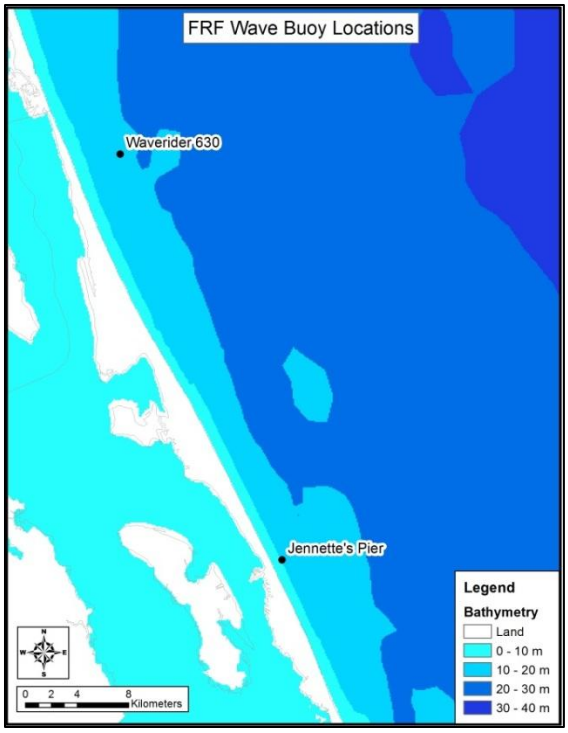

Figure II-2.1: USACE FRF wave stations

2.2.1.1 Correlation Between Sites

Due to the minimal historical wave record at Jennette's Pier AWAC, an accurate representation of the wave climate cannot be made solely based on this one site. The Waverider 630 was compared to the available record at the Jennette's Pier AWAC to see if there was any spatial correlation. Wave parameter data was obtained from both buoys between the dates of August 1, 2009 and August 14, 2010. This date range was chosen to incorporate a full year of data from the available record from each location. There were three gaps in the data for the Jennette's Pier AWAC between the chosen dates, which can be seen by the absence of data in red in Figure II-2.2.

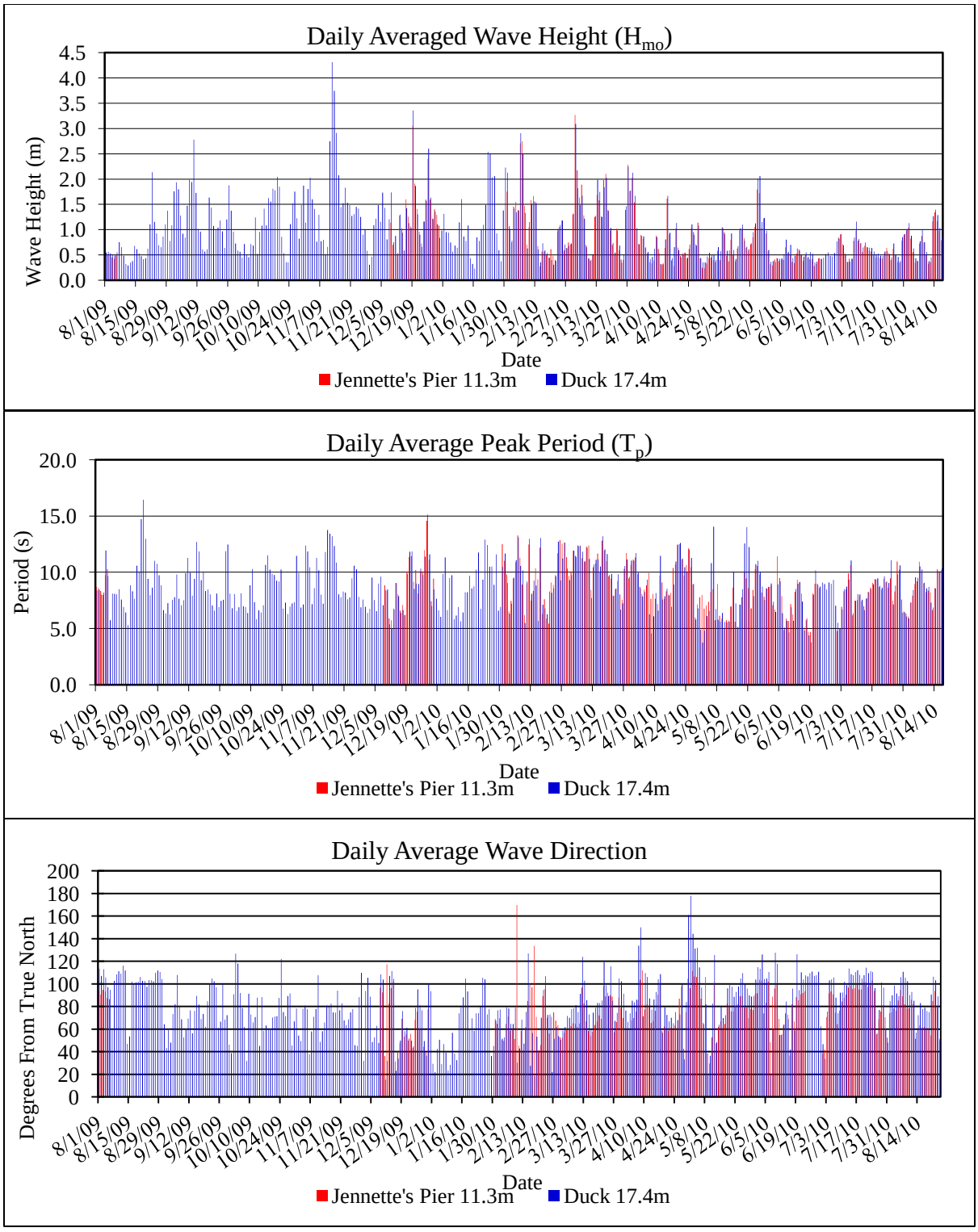

Figure II-2.2: Daily Average Wave Height (Hmo), Peak Period (Tp), and Wave Direction of Waverider 630 buoy and Jennette's pier meter shown over the available history for Jennette's Pier 8/1/2009 – 8/14/2010

The Jennette's Pier AWAC went offline between the dates of 8/7/2009 to 12/8/2009, 1/1/2010 to 1/30/2010, and 6/24/2010 to 6/302010. An average was taken of the hourly recordings over one day at each buoy to give the daily average for each parameter. To make the comparison between the two locations, the difference was taken between each daily averaged wave parameter for the entire data set and plotted in a histogram. The difference was taken as the Waverider 630 wave height minus the Jennette's Pier AWAC wave height. A positive difference indicates a larger wave height at the Waverider 630 and a negative difference indicates a larger wave height at the Jennette's Pier AWAC. After examining the histogram for the energy based wave height, shown in Figure II-2.3, it seems that there is a positive skew in the data, where 68% of the wave heights were slightly larger at the Waverider 630.

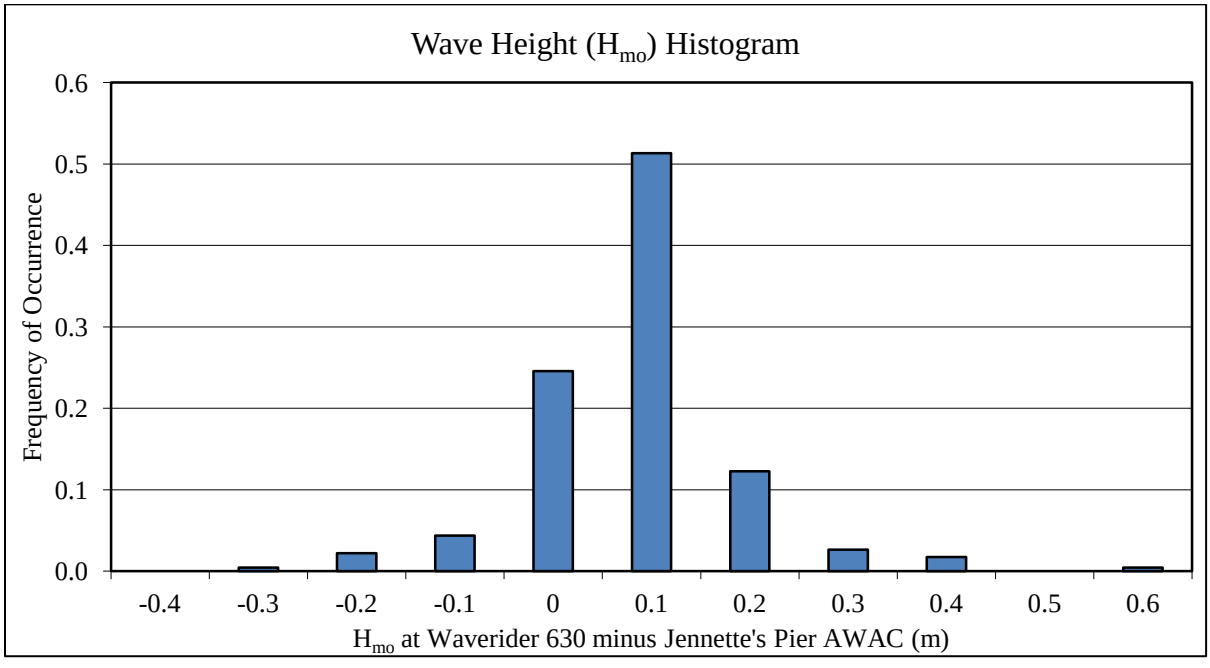

Figure II-2.3: Histogram of Wave Height (H_{mo}) differences

The average value for the wave height differences is 0.03 meters and the standard deviation is 0.1 meters. The average percent difference for the wave height was 11.2%. These values indicate a high correlation for wave height for the two locations and would be appropriate to use the data from the Waverider 630 buoy as an approximation for the conditions at Jennette's pier AWAC. This same process was repeated for the peak wave period and wave direction. The histograms created for the difference in peak wave period and wave direction were also taken as the Waverider 630 parameter minus the Jennette's Pier AWAC parameter. The peak period histogram is shown below in Figure II-2.4.

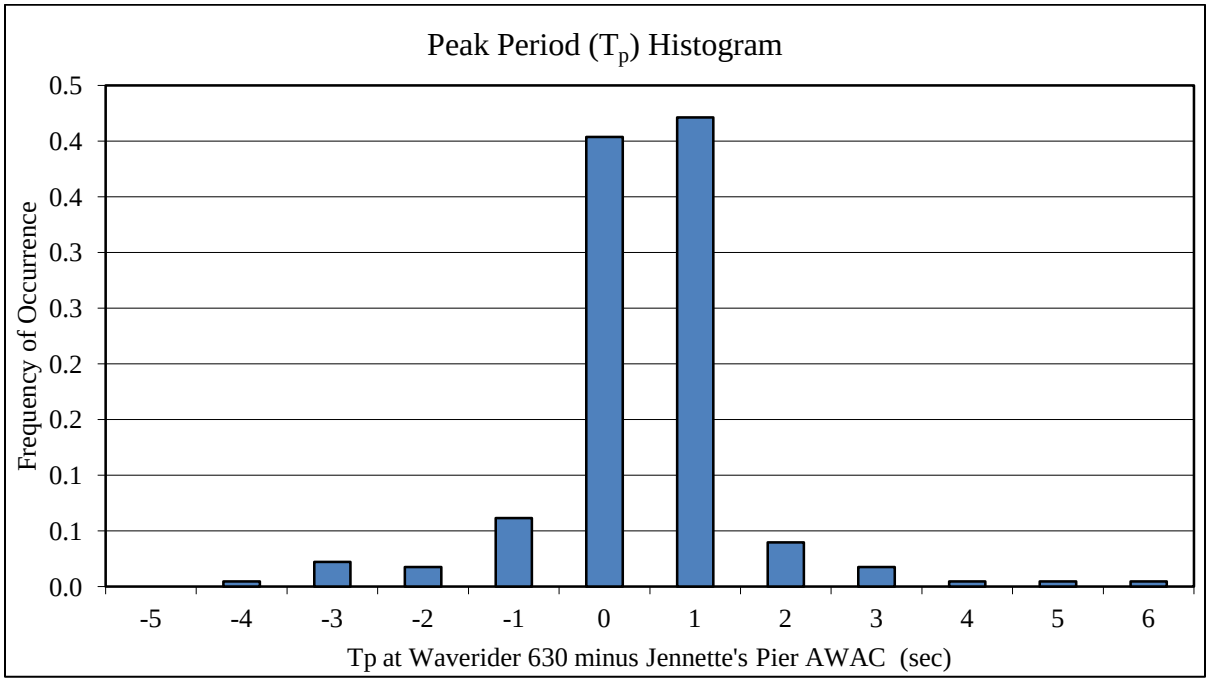

Figure II-2.4: Histogram of Peak Period (T_p) differences

The histogram of the peak wave period differences is almost split evenly where 51% of the time the wave period is larger at the Jennette's Pier AWAC, which correlates to a mean difference value of -0.05 seconds. The majority of the differences fall within one standard

deviation, which was found to be 1.08 seconds of the mean. The peak period at the Waverider 630 correlated very well to the peak period at the Jennette's Pier AWAC with the lowest average percent difference of 7.6%. Out of the three parameters, wave direction had the most variability, which is shown in the wave direction histogram in Figure II-2.5.

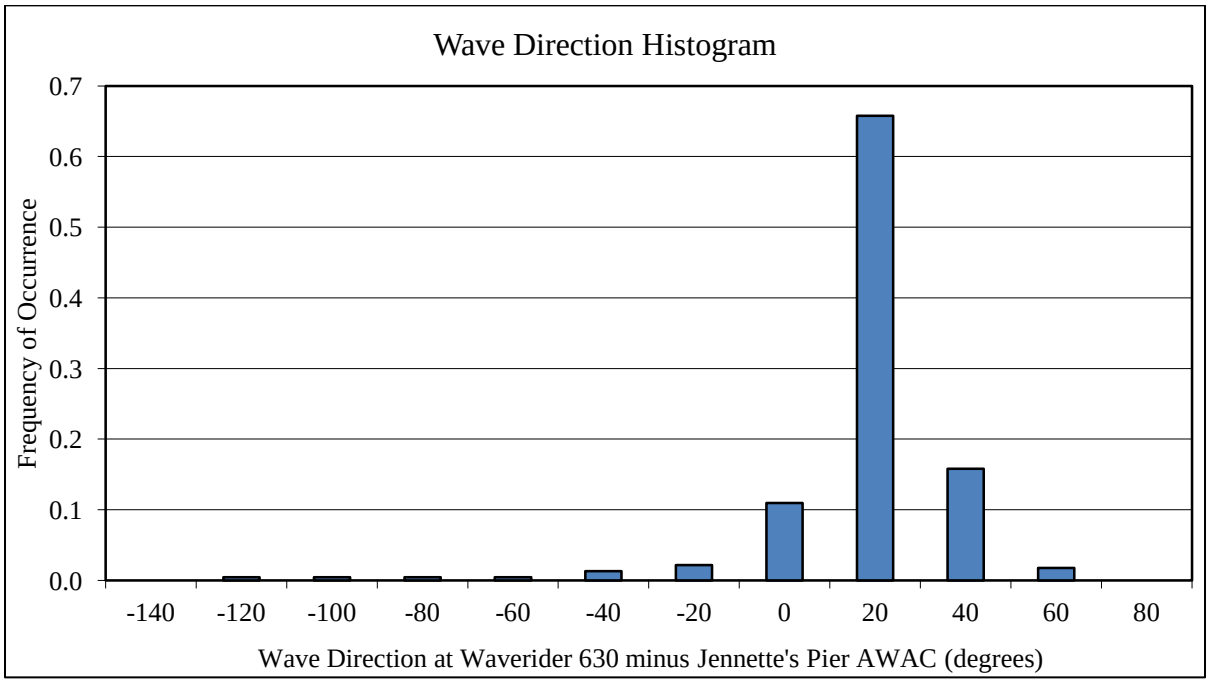

Figure II-2.5: Histogram of Wave Direction differences

Between the two sites, 84% of the differences were positive with a mean difference of 8.7°. This was expected due to the orientation of the shoreline at the two locations. The shoreline at the FRF research pier in Duck and Jennette's pier in Nags Head face east northeast with an approximate shoreline orientation of 161° and 155° from true north respectively. This yields a difference of 6°, which correlates well to the mean difference found from the histogram. From Snell's law, as a wave front propagates onshore at an angle, the wave crest will tend to orient itself with the bathymetric contours. In this location, the nearshore bathymetric

contours are regular and shore parallel (US Army Corps of Engineers, 2012). With these conditions, the differences should be larger at Duck producing a positive difference of at least 6° on average. A positive value indicates that the incoming waves at Jennette's Pier had an angle that was farther clockwise from the waves at Duck. There were also some extreme differences between the two sites. This could possibly be explained by a localized storm that only impacted one site and not the other. However, for very small H_{mo} ($\leq$ 0.5 m), the direction is difficult to determine and rather useless. The maximum positive and negative difference and the average percent difference for each parameter as well as the wave parameter statistics are listed in the Table II-2.2 below.

Table II-2.2: Wave parameter summary statistics

Wave Parameter	Mean Difference	Standard Deviation Difference	Maximum Positive Difference	Maximum Negative Difference	Average Percent Difference
Wave Height (H_{mo}, m)	0.03	0.1	0.56	-0.35	11.2%
Peak Period (T_p, sec)	-0.05	1.08	5.57	-4.22	7.6%
Wave Direction (deg)	8.7	21.0	81.5	-139.7	20.5%

All three parameters seemed to correlate well between the two sites when examining the histograms. The majority of the data seemed to be located around zero meaning the difference between the locations was very small. Each parameter had a few outliers where the Wavrider 630 data was much larger than Jennette's Pier AWAC data and vice versa. For wave height and peak period, the differences were relatively small; therefore, the values

measured at the Waverider 630 would accurately represent the conditions at Jennette's Pier in a statistical sense. The direction seemed to have the most variability which was verified by it having the largest average percent error of 20.5%. This was most likely a result of varying shoreline orientation between Duck and Jennette's Pier. When the outliers do occur, the error can be large and not accurately represent the wave direction at Jennette's Pier.

2.2.2 Wave Climate

The comparative analysis found that the wave climate at Jennette's pier was comparable to the wave climate at Duck. Therefore, the historical wave record at the Waverider 630 buoy can be used to represent the wave climate at Jennette's pier. With Jennette's Pier acting as a potential testing site for WECs, a thorough analysis of the wave climate is crucial in order to give developers an idea of the wave environment their device will be deployed in for testing. To accomplish this, the historical wave record for the Waverider 630 buoy between the dates of January 1, 1997 through December 31, 2011 was acquired from the FRF website. The hourly data for each wave parameter was averaged over each month of the year. The range of the monthly averaged values over the entire history were plotted along with the mean value for each parameter over the history. These results are plotted in Figure II-2.6.

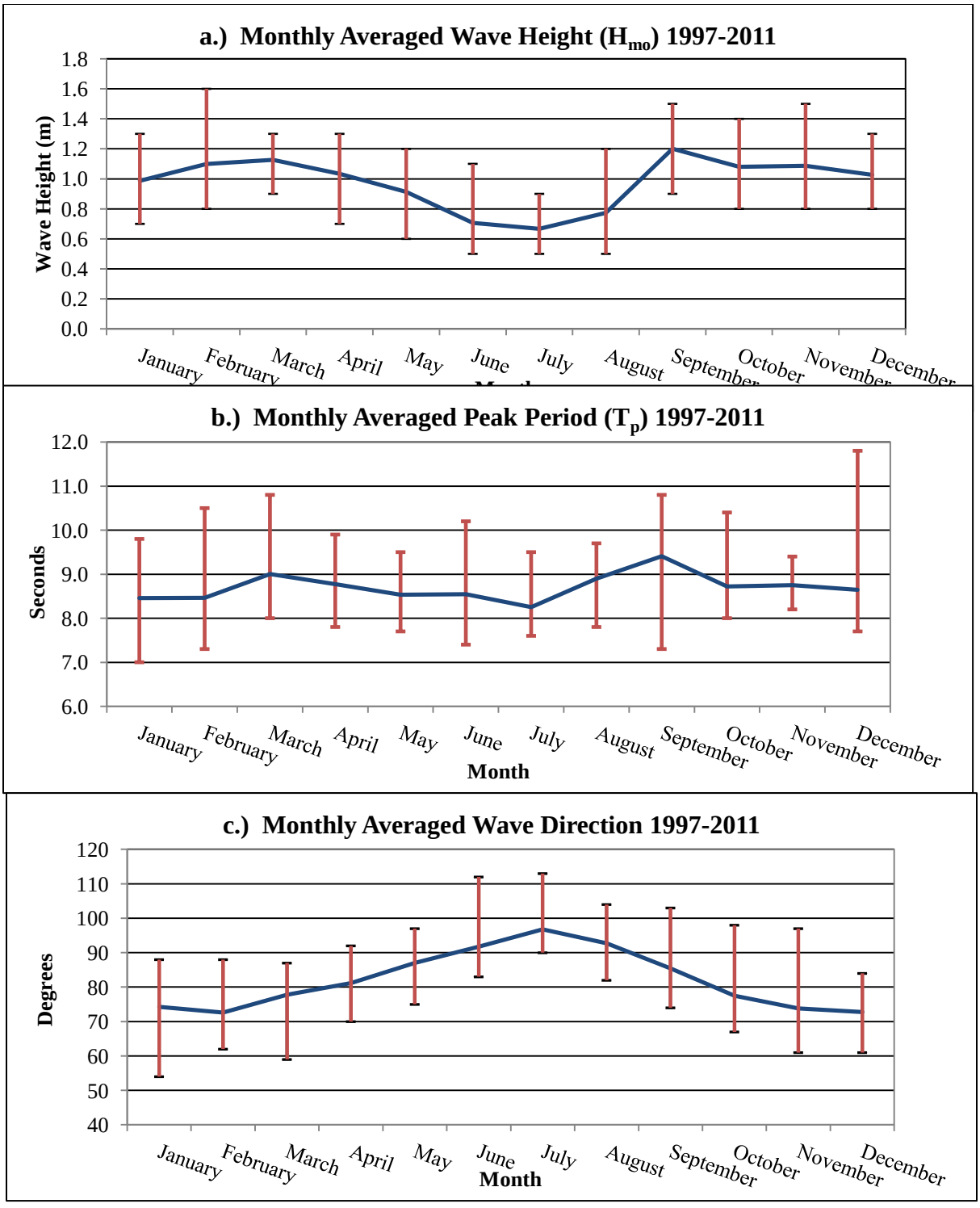

Figure II-2.6: a.) Monthly Averaged Wave Height (H_{mo}), b.) Peak Period (T_p), and c.) Direction over entire directional history of the Waverider 630 buoy

The blue line represents the mean value over the history and the red line represents the range over the history of each month. The mean monthly averaged wave heights in figure II-2.6a show evidence of a seasonal trend. The months at the beginning of the year and end of the year have a higher mean wave height with a trough of lower wave heights in between. Further analysis of this seasonality will be discussed in the following section. The mean monthly averaged peak period is fairly consistent throughout the year. The minimum and maximum values of the mean monthly averaged wave height and peak period are shown in table II-2.3 with their associated months.

Table II-2.3: Mean monthly averaged wave parameters summary

Wave Property	Minimum	Minimum Month	Maximum	Maximum Month
Mean Wave Height (H_{mo}, m)	0.67	July	1.20	September
Mean Peak Period (T_p, sec)	8.25	July	9.41	September
Mean Wave Direction (deg)	72.6	February	96.7	July

The month of September was identified as the most active month on average with the highest mean monthly averaged wave height and peak period. The month of July was identified as the least active month on average with the lowest mean monthly averaged wave height and peak period. The mean wave directions that are associated with the active months are closer to shore perpendicular. The mean wave direction during less active time of year was predominately from the southeast.

2.2.2.1 Seasonality

To analyze the seasonal variations of wave parameters, the historical hourly wave record at the Waverider 630 buoy was divided into the four seasons: winter, spring, summer, and fall. The winter months consisted of December, January, and February. The spring months consisted of March, April, and May. The summer months consisted of June, July, and August. The fall months consisted of September, October, and November. Wave height, peak period and direction were divided into the four seasons over the entire history from 1997 to 2011. A histogram was created for each of the wave parameters to examine the distribution throughout each season. The wave height histograms are shown below in figures II-2.7 through II-2.10. The bin width for each of the wave height histograms was set as 0.2 meters.

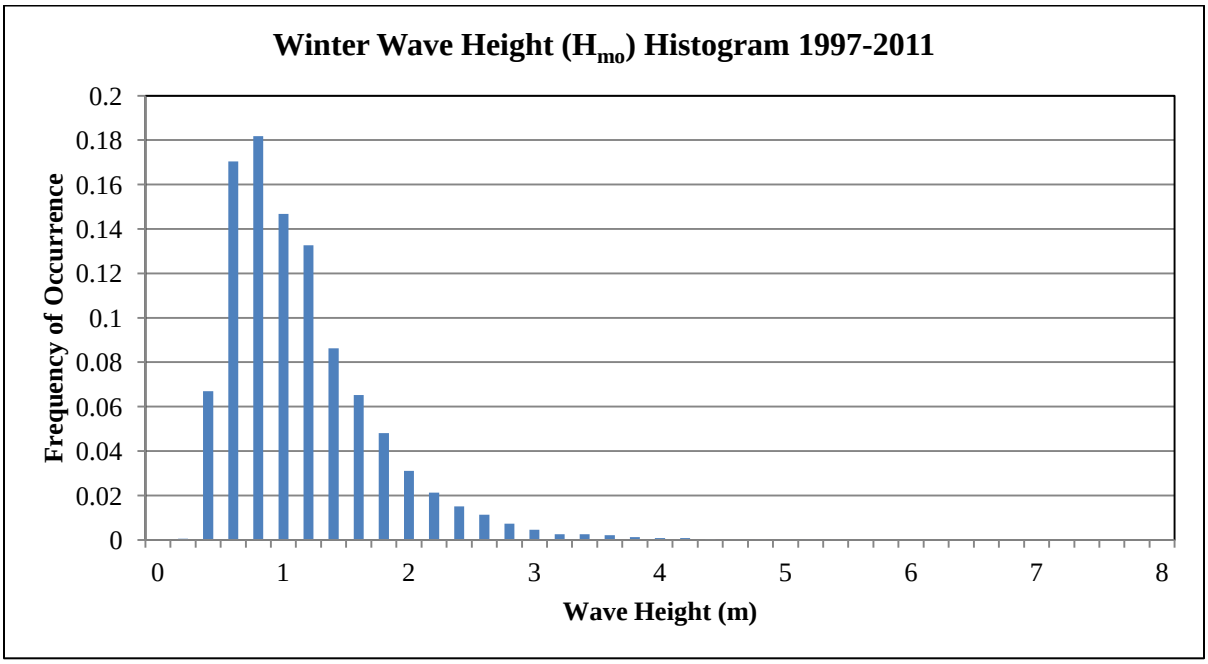

Figure II-2.7: Winter Wave Height (H_{mo}) Histogram over entire directional history of Waverider 630 buoy

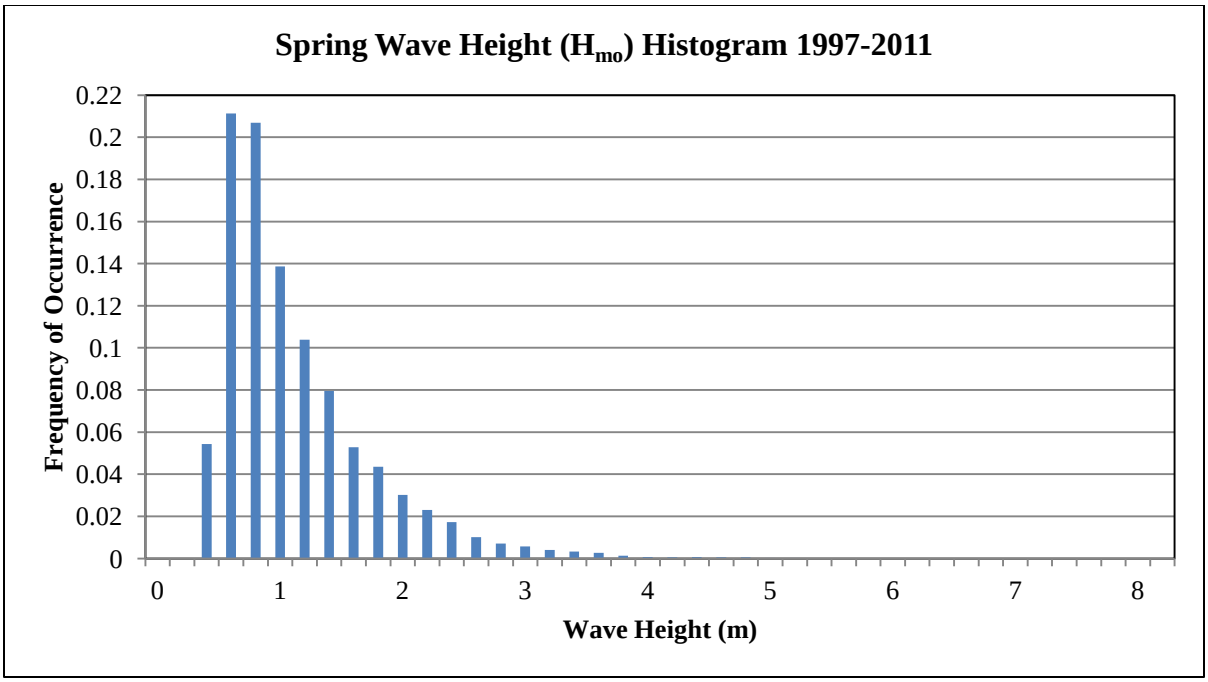

Figure II-2.8: Spring Wave Height (H_{mo}) Histogram over entire directional history of Waverider 630 buoy

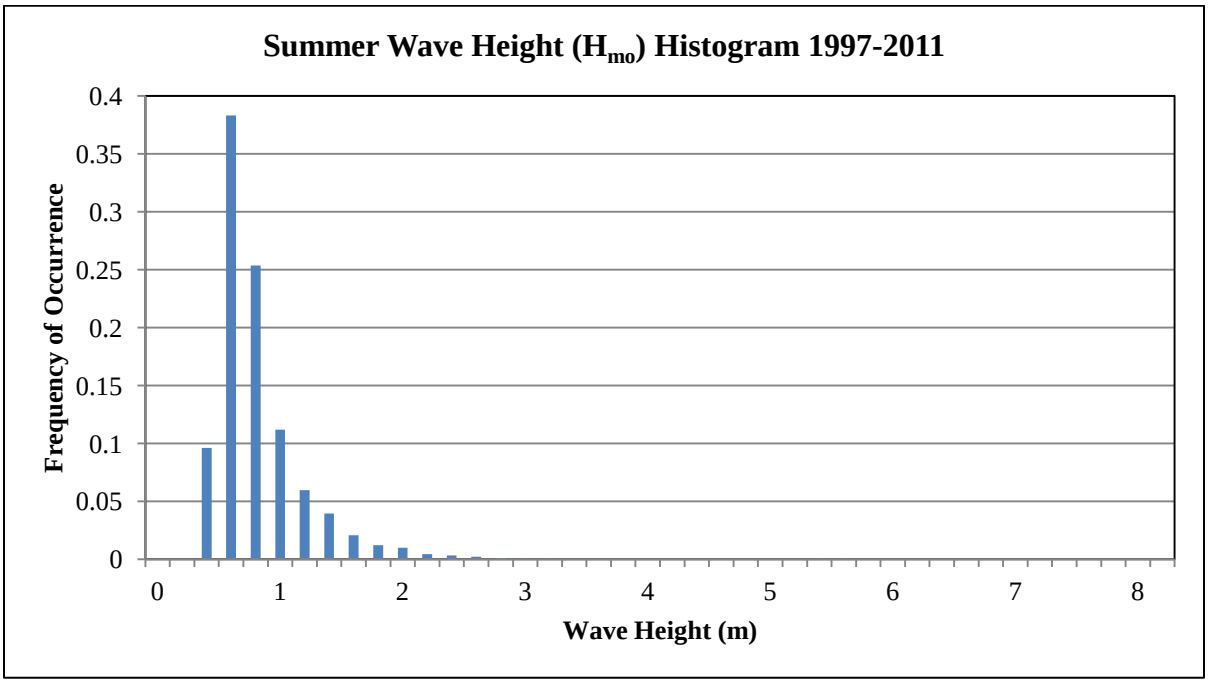

Figure II-2.9: Summer Wave Height (H_{mo}) Histogram over entire directional history of Waverider 630 buoy

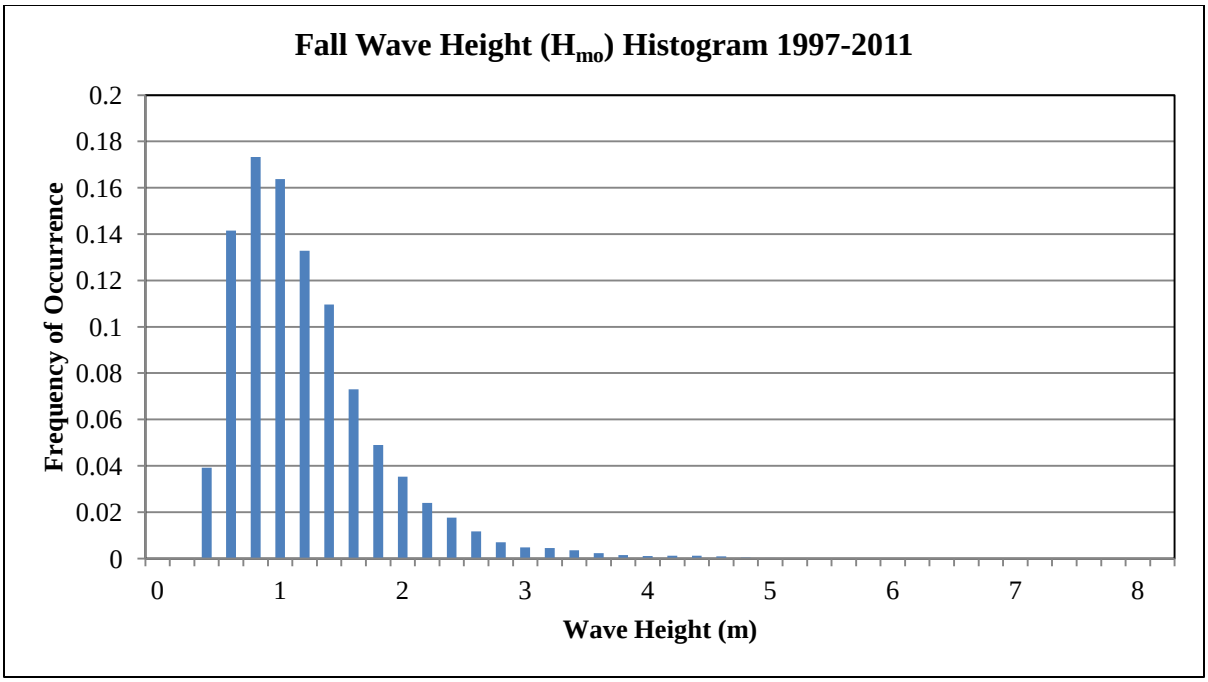

Figure II-2.10: Fall Wave Height (H_{mo}) Histogram over entire directional history of Waverider 630 buoy

The wave height distribution for the winter, spring, and fall seasons is very similar. The wave height data for the summer season has a much narrower spread than the other seasons. The summer has a very high frequency of occurrence for very low wave heights indicating a very minimal wave climate where wave heights rarely exceed 1.2 meters. The distribution of the wave heights for the winter, spring, and summer seasons have a much wider spread relative to the summer indicating a higher frequency of storm events.

The peak wave period histograms are shown below in figures II-2.11 through II-2.14. The bin width for these histograms was set as 1 second.

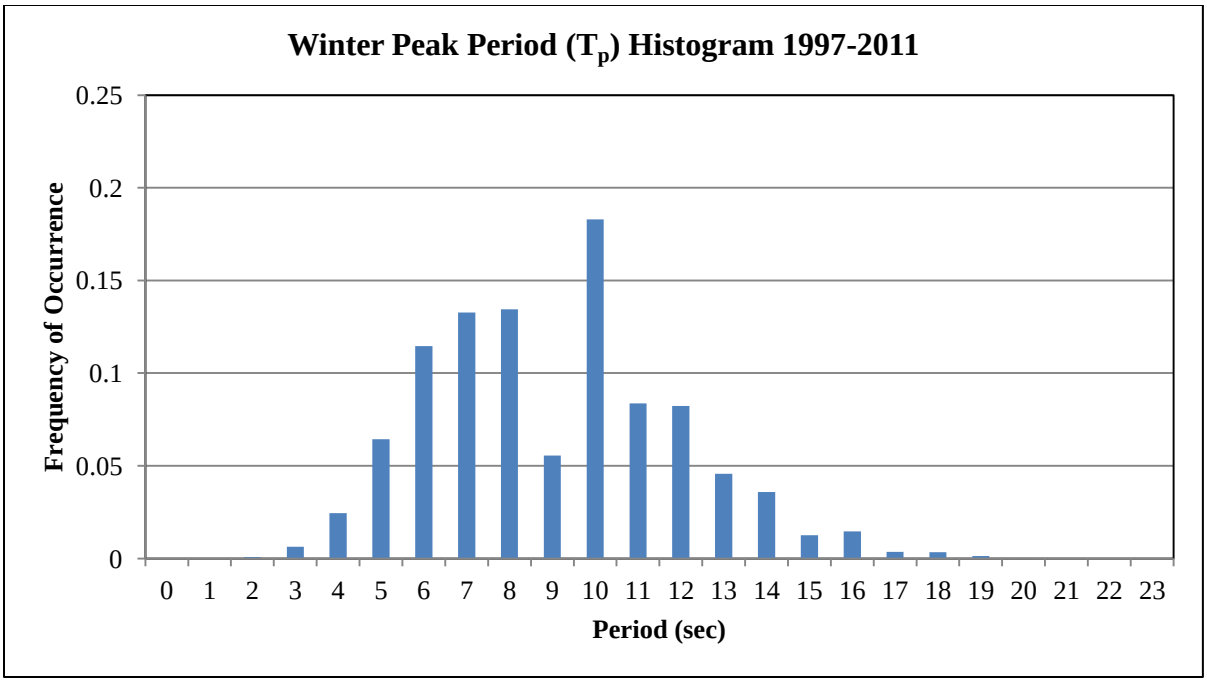

Figure II-2.11: Winter Peak Period (T_p) Histogram over entire directional history of Waverider 630 buoy

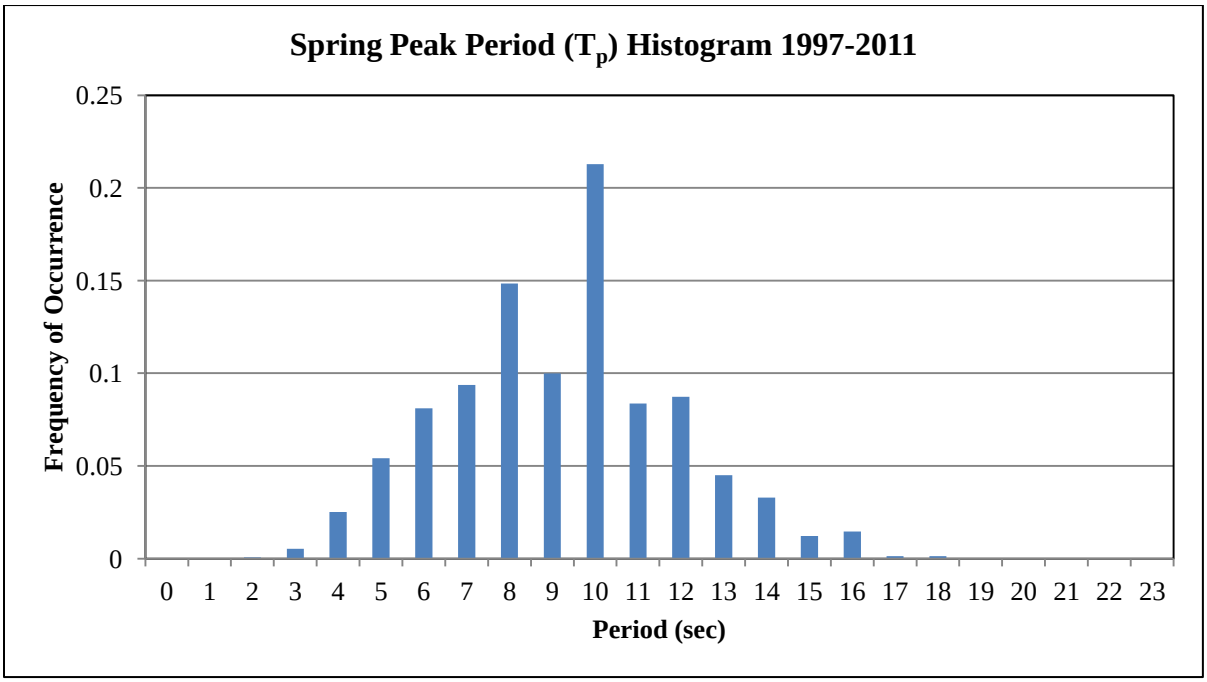

Figure II-2.12: Spring Peak Period (T_p) Histogram over entire directional history of Waverider 630 buoy

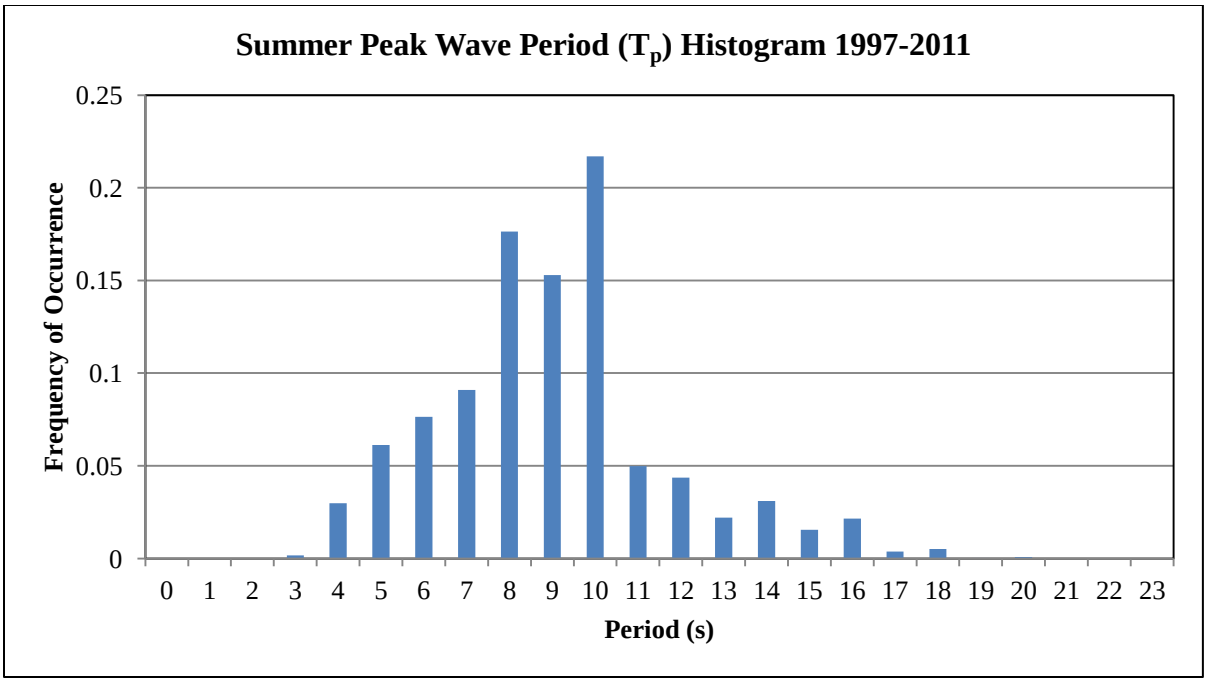

Figure II-2.1: Summer Peak Period (T_p) Histogram over entire directional history of Waverider 630 buoy

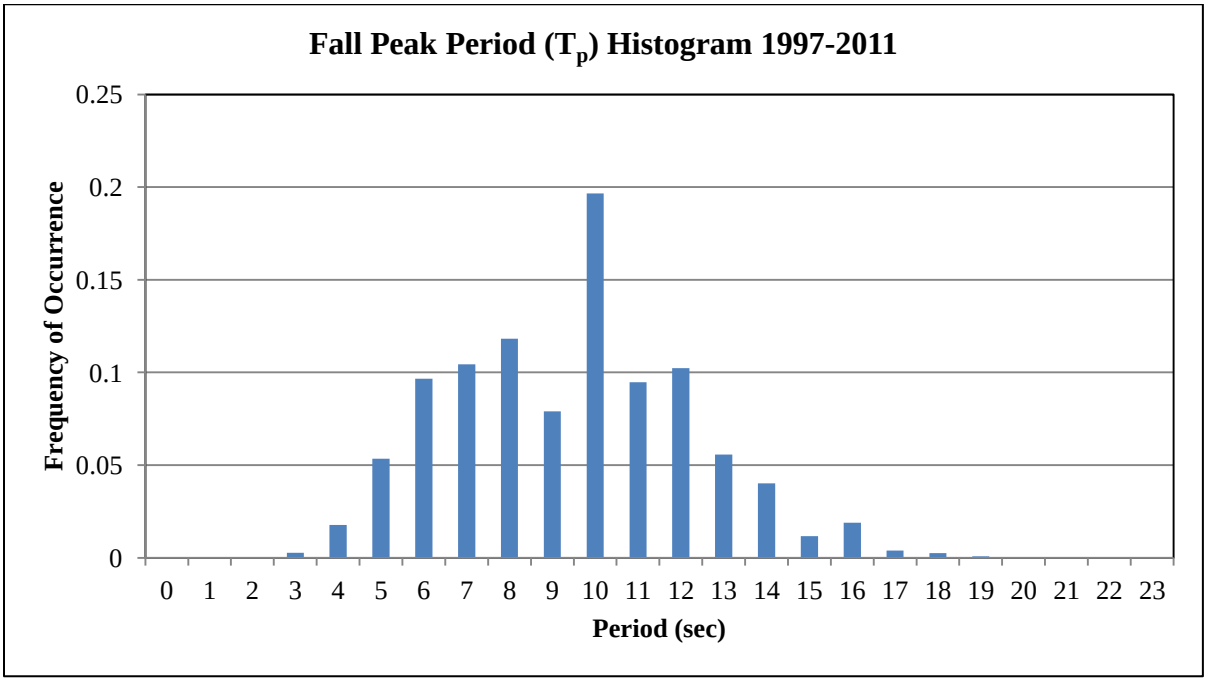

Figure II-2.2: Fall Peak Period (T_p) Histogram over entire directional history of Waverider 630 buoy

The peak of the peak period histogram for all four seasons was the bin of 9 to 10 seconds. The peak period distribution for the winter, spring, and fall seasons is very similar. For the summer season, the peak period distribution is slightly different than the other seasons in that the occurrences of a peak period greater than 10 seconds occur less frequently.

The wave roses are shown below in figures II-2.15 through II-2.18. The bin width for these histograms was set as 15 degrees.

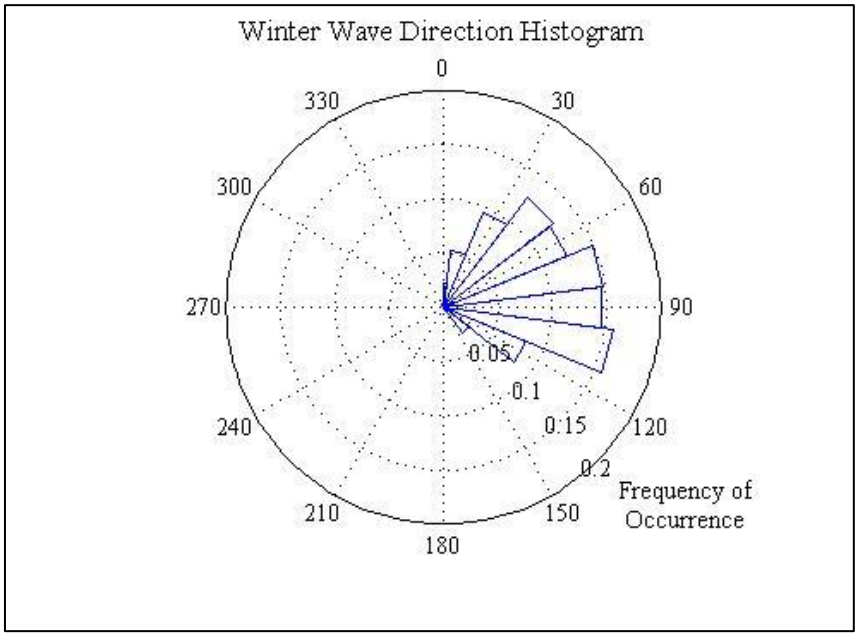

Figure II-2.3: Winter wave rose of Waverider 630

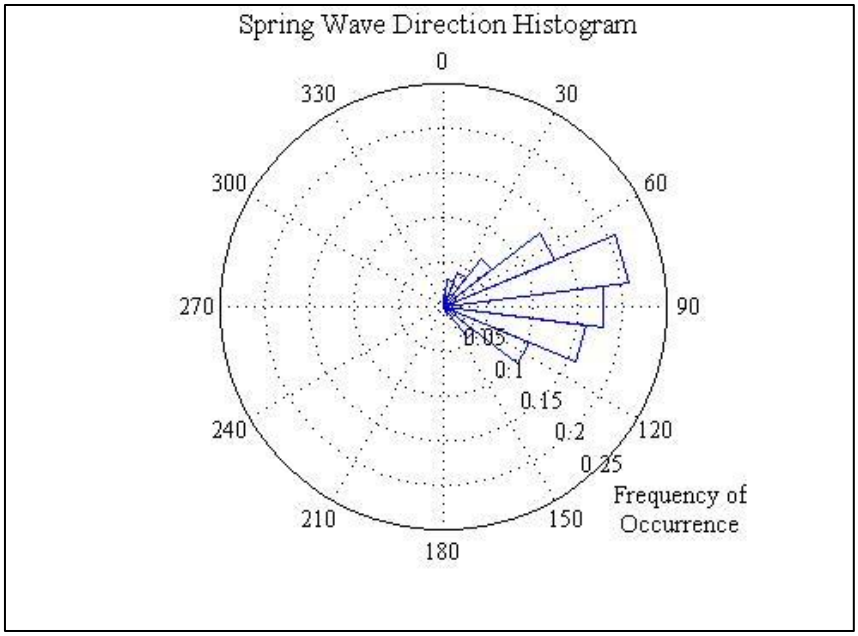

Figure II-2.4: Spring wave rose of Waverider 630

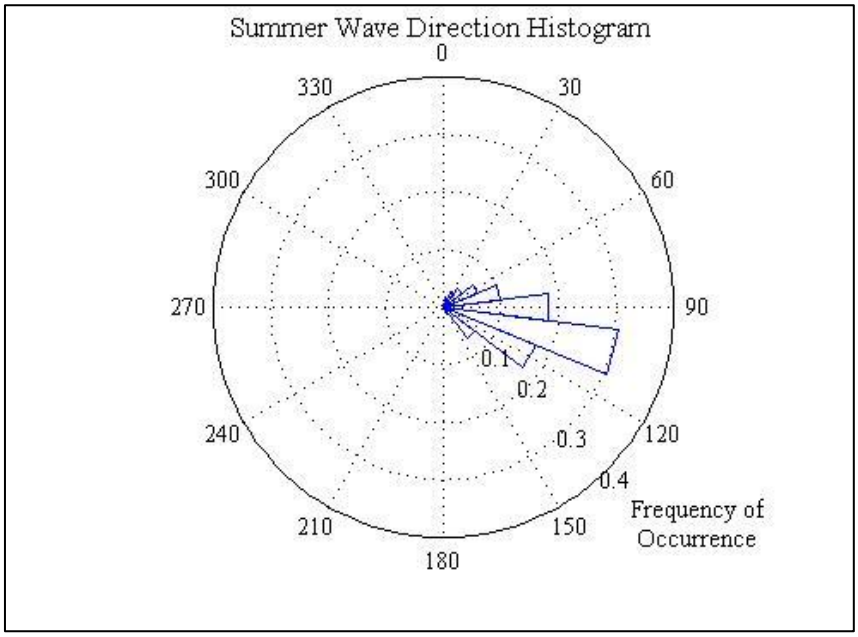

Figure II-2.5: Summer wave rose of Waverider 630

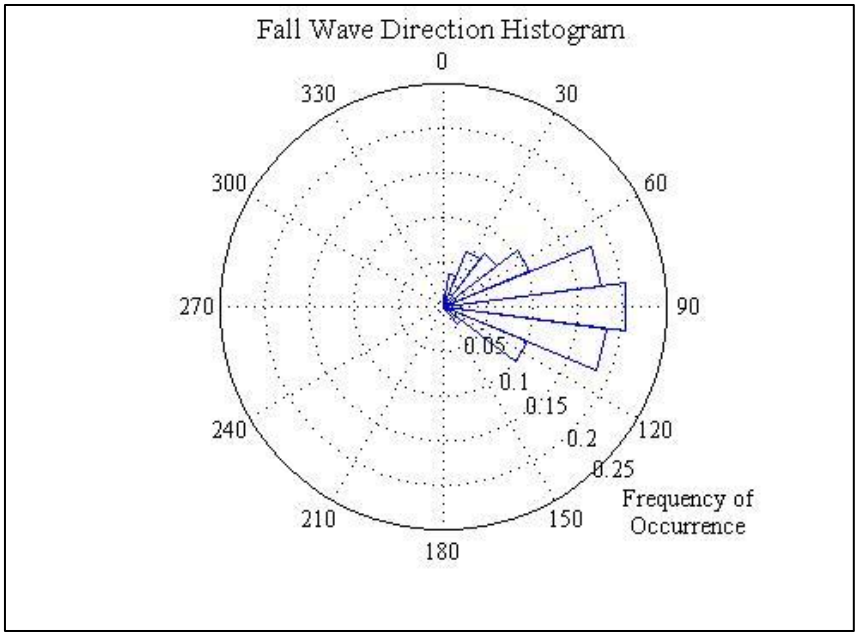

Figure II-2.6: Fall wave rose of Waverider 630

The wave direction during the winter season was evenly distributed between 37.5° and 112.5°. The wave direction during the spring season was distributed between 67.5° and 97.5°. The wave direction during the summer season shows a clear dominant direction between 97.5° and 112.5°. Finally, the wave direction during the fall was predominantly between 67.5° and 112.5°.

The average wave height over the entire year of the full history from the previous section was 0.98 meters. An estimate of 1 meter was used as a benchmark to analyze the histogram distribution. The percentage of wave heights less than one meter, between one meter and two meters, and greater than two meters for each season are shown in Table II-2.4. These percentages recorded are of the available hourly data recorded at the Waverider 630 buoy not including hours where the buoy was inoperable. A two meter wave meets the requirement

for wave height of a storm wave by the FRF. The seasonal mean wave height and peak wave period are also shown in the same table below.

Table II-2.4: Seasonality Summary

Season	H_{mo} Mean (m)	% H_{mo} < 1m	1m < %H_{mo} < 2m	%H_{mo} > 2m	T_p Mean (sec)	Dir Mean (deg)
Winter	1.04	56.6%	36.3%	7.0%	8.56	75.8
Spring	1.03	61.1%	31.0%	7.9%	8.73	83.5
Summer	0.73	84.4%	14.1%	1.4%	8.50	95.6
Fall	1.12	51.8%	40.0%	8.2%	8.95	81.1

From this analysis, the fall season of September, October, and November, was identified as having the most active wave climate. The mean wave height and peak wave period was at its maximum during this season. Fall also had the lowest percentage of wave heights below 1 meter and highest percentage of wave heights between 1 meter and 2 meters.

2.3 Available Wave Power

2.3.1 Wave Information Studies Data

The Wave Information Studies was a project taken on by the United States Army Corps of Engineers (USACE) which produces an hourly wave climate for the Atlantic, Pacific, Gulf of Mexico, and Great Lakes coasts for at least a 20 year history from numerical wave hindcast models (US Army Corps of Engineers, 2011). The area of interest for this study is the Northeast coast of North Carolina from Cape Lookout in the South to the North Carolina Virginia border in the North. This region utilized the second generation wave model

WISWAVE to predict the wave parameters as well as the directional spectra from the historical wind data. The accuracy of this model has been verified by comparing the generated WISWAVE output with measured data. WISWAVE produces hourly significant wave height, peak wave period, and mean wave direction at each of the virtual buoy locations between the dates of 1980 and 1999. These virtual buoys are spaced throughout the North Carolina coastline between the depths of 15 and 29 meters. Figure II-3.1 shows the 12 stations chosen for this study overlaid with the bathymetry.

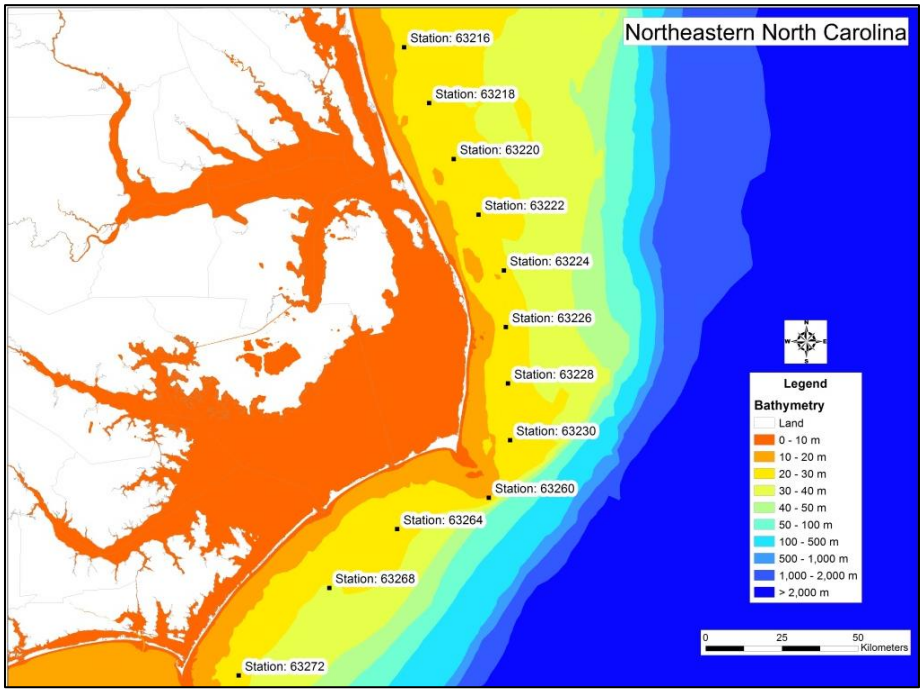

Figure II-3.1: WIS station locations with bathymetry

2.4 Wave Power Calculation from WIS Data

Wave power was calculated at each of the chosen WIS stations assuming Airy, or linear, wave theory as outlined in the USACE Coastal Engineering Manual (CEM) (U.S. Army

Corps of Engineers, 2002). Wave power, also known as wave energy flux, is the transmission rate of energy per unit crest length in the direction of a propagating monochromatic wave. The total amount of energy in a wave is defined by the sum of the potential and kinetic energy. Potential energy is a result of gravity acting on the water particles that are displaced from equilibrium between the trough and the crest of the wave. Kinetic energy is a result of the water particle velocities related to wave motion. The total wave energy in one wave length per unit crest width is given as

$$E = E_p + E_k = \frac{\rho g H^2 L}{16} + \frac{\rho g H^2 L}{16} = \frac{\rho g H^2 L}{8} \tag{2.3}$$

where E_p is the potential energy, E_k is the kinetic energy, H is the wave height, and L is the wave length. The total average wave energy per unit surface area, known as the energy density, is given by:

$$\bar{E} = \frac{E}{L} = \frac{\rho g H^2}{8} \tag{2.4}$$

where the energy density is proportional only to the wave height squared. The rate at which energy density is transmitted is the wave group velocity, which is given by:

$$C_g = nC = \frac{1}{2}\left[1 + \frac{4\pi d/L}{\sinh(4\pi d/L)}\right]\frac{L}{T} \tag{2.5}$$

where C is the wave celerity, n ranges between 0.5 for deep water and 1 for shallow water. Wave energy flux, or wave power, is then given by:

$$\bar{P} = \bar{E} C_g \tag{2.6}$$

Substituting equation (2.4) and equation (2.5) with n equal to 0.5 for the deep water condition into equation (2.6), deep wave power is then found by:

$$\bar{P} = \frac{\rho g^2 H^2 T}{32\pi} \tag{2.7}$$

where the deep water assumption was made so that the maximum amount of wave power available off the coast could be found. Equation 2.7 was used to calculate wave power at each of the 12 WIS stations in North Carolina for each year from 1980 through 1999. The sum of the hourly power calculations was taken to obtain the total wave power available for that year. This method was applied for each year of the historical data then averaged to give the average yearly power available in units of gigawatt hours per meter of shoreline per year (GW-hr/m/year) along the Outer Banks.

2.4 Results

2.4.1 Wave Power

The maximum yearly wave power along the coastline was 0.144 GW-hr/m/year located at station 63228 which is between the towns of Salvo and Avon. The minimum yearly wave power was 0.076 GW-hr/m/year located at station 63216 which is just north of the town of Corolla. The resulting values for the yearly wave power average for each station are shown below in Figure II-4.1.

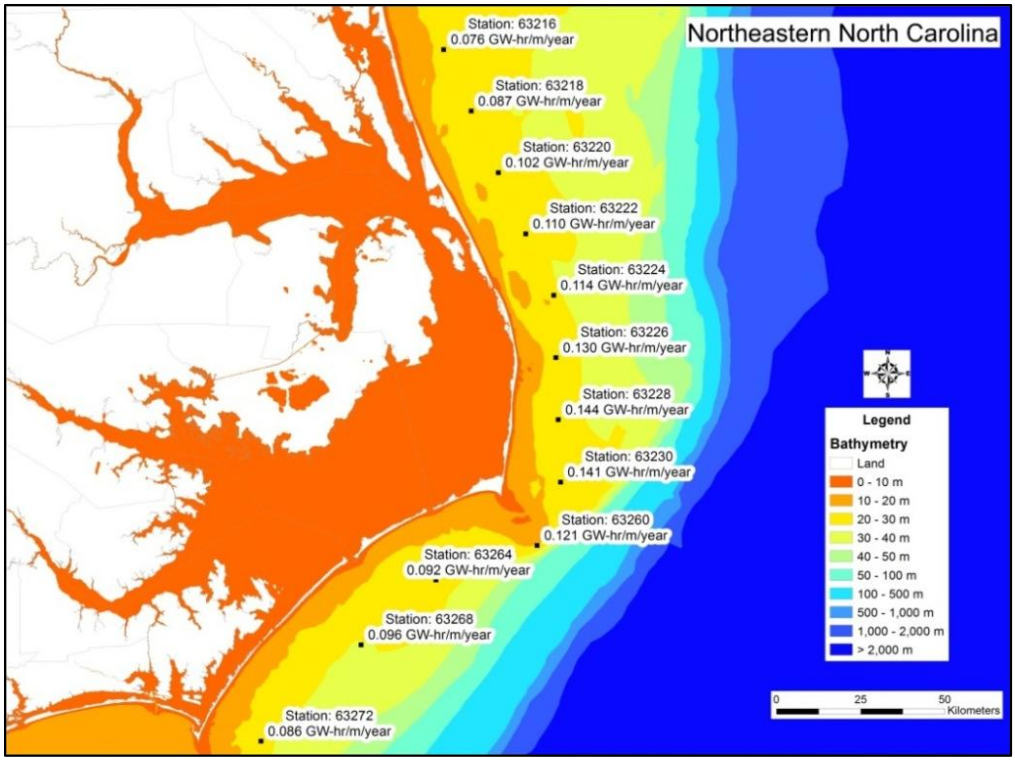

Figure II-4.1: Average yearly wave power from WIS stations with bathymetry

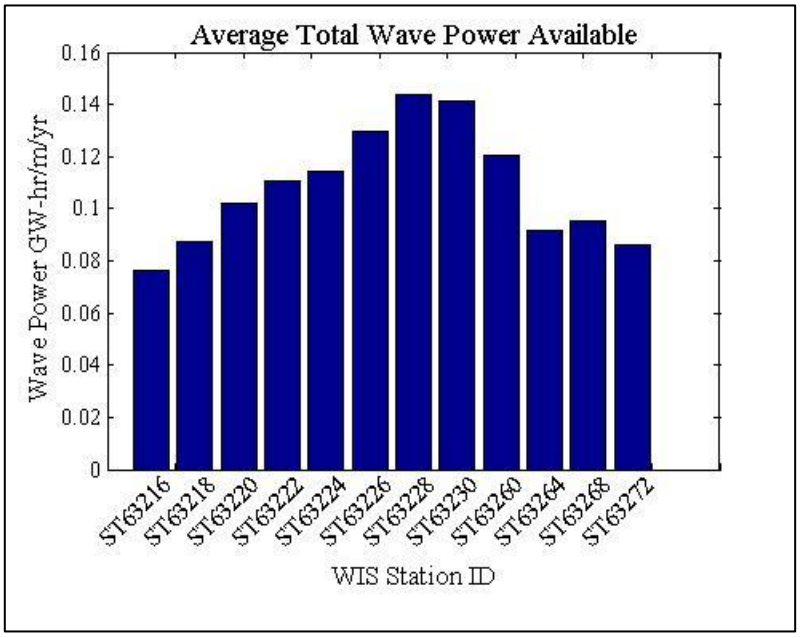

Figure II-4.2: Average yearly wave power

The wave power is greater along the section of the outer banks that is closest to the continental shelf. One of the reasons for this is because once the waves start propagating into shallower water, bottom friction starts to affect the power loss. Therefore, the wave power calculated in the areas south of Cape Lookout and north of Rodanthe decrease due to the divergence of the shoreline and continental shelf. The total power available from Cape Lookout to the North Carolina Virginia border was found by interpolating between WIS stations to equal 25.9 TW-hr/yr. The Electric Power Research Institute (EPRI) studied the New England and Mid-Atlantic regions and found the total wave energy resource to be 110 TW-hr/yr (Bedard, et al., 2007). The northern half of the Outer Banks alone accounts for 23.5% of the wave energy resource for the entire region studied by EPRI. Assuming the extraction of 15% wave to mechanical energy conversion, typical power train efficiencies of 90%, and plant availability of 90%, the total power for North Carolina would be reduced to 3.15 TW-hr/yr (Bedard, et al., 2007). According to the U.S. Department of Energy, the average monthly consumption of energy per household in North Carolina is 1,238 kW-hr (U.S. Department of Energy, 2012). This equates to approximately 0.015 GW-hr/year per household; therefore, there is enough wave power available to power a little over 212,000 homes for an entire year.

2.5 Conclusion

With the completion of the new Jennette's Pier in May of 2011, the Outer Banks is now equipped to facilitate ocean tests of WECs. Jennette's Pier is owned by the North Carolina Aquarium Society and was designed as a multiuse pier to include not only fishing, but public

outreach from the scientific community about current research projects on renewable energy in the local community. This opens up the opportunity for North Carolina to promote its facilities as a testing location for WECs nationwide. North Carolina also has an abundance of historical wave data thanks to the USACE FRF. From the previous analyses, an accurate description of the historical wave climate was made at this location. It was found that the fall season was the most active with the peak month being September. The wave climate was found to have season effects creating a mild wave climate during the summer months; however, maintaining a fairly moderate wave climate throughout the rest of the year. Even though there is a moderate wave climate at best in North Carolina, there is still a significant amount of energy available for extraction to help offset a portion of the energy requirements for the state. Further investigation should be done as to the cost of this pursuit.

CHAPTER 3: Nearshore Wave Modeling for Site Analysis Jennette's Pier

3.1. Introduction

The objective of this section of the study is to estimate the effects a WEC array would have on the shoreline or coastal processes. Jennette's pier, located in Nags Head, North Carolina, has been identified as the example site for this analysis. The nearshore wave model SWAN (Simulating WAves Nearshore) (Booij, Ris, & Holthuijsen, 1999) was used to propagate waves in from the offshore regime through a WEC array to the nearshore regime. As the waves propagate through the WEC array, energy will be absorbed therefore altering the nearshore wave climate. To examine the effects the WEC array has on coastal processes, SWAN was run for multiple wave conditions with and without the effects of the WEC array. The results from SWAN were used to identify coastal processes by examining the change in wave height and longshore current due to the WEC array. Previous studies have been done on a similar topic at a site off the north coast of Cornwall, UK (Millar, Smith, & Reeve, 2007) and at a site off the coast of Oregon (Oskamp & Ozkan-Haller, 2010). Both studies used SWAN to examine the change in shoreline wave climate due to an array of WECs. The WEC array in the Millar (2007) study was modeled in SWAN as a single partially transmitting obstacle with multiple transmission coefficients at the study site. Oskamp defined the WEC array as individual devices which were represented as rigid piles extending through the entire water column that absorbed 100% of the passing wave energy (Oskamp & Ozkan-Haller, 2010).

3.2. Simulating WAves Nearshore (SWAN) Wave Model

3.2.1. SWAN Overview

SWAN (Simulating WAves Nearshore) is a third-generation wave model that propagates short-crested waves over a given bathymetry in the nearshore region, driven by local winds and boundary conditions (Booij, Ris, & Holthuijsen, 1999). The physical processes that are explicitly represented are wave propagation in time and space, shoaling, refraction due to current and depth, frequency shifting due to currents and non-stationary depth, wind generated waves, triad and quadruplet wave-wave interactions, whitecapping, bottom friction and depth induced breaking, dissipation from vegetation, wave-induced set-up, transmission through obstacles, and diffraction (Booij, Ris, & Holthuijsen, 1999).

The evolution of the wave spectrum is described by the spectral action balance equation given in Cartesian coordinates by (Hasselmann, et al., 1973):

$$\frac{\partial}{\partial t}N + \frac{\partial}{\partial x}c_x N + \frac{\partial}{\partial y}c_y N + \frac{\partial}{\partial \sigma}c_\sigma N + \frac{\partial}{\partial \theta}c_\theta N = \frac{S}{\sigma} \tag{3.1}$$

The action density is defined as $N = {}^{E}/_{\sigma}$ where E is the energy density and σ is the wave frequency. Action density is used instead of energy density because action density is conserved during wave propagation when an ambient current is present (The SWAN team, 2012). The first term represents the local rate of change of action density, N, with respect to time. This term is neglected when running in stationary mode. The second and third term represent propagation of action in geographical space with propagation velocities, c_x and c_y, in x and y space respectively. The fourth term represents the shifting of the relative

frequency due to variations in depths and currents with propagation velocity, c_σ, in σ space. The fifth term represents depth-induced and current-induced refraction with propagation velocity, c_θ, in θ space. SWAN uses linear wave theory to calculate each of the propagation velocities.

SWAN accounts for diffraction based on the phase-decoupled refraction-diffraction approximation (Holthuijsen, Herman, & Booij, 2003).

The S term on the right side of the equation is the energy density source term representing the effects of generation, dissipation, and nonlinear wave-wave interactions (Booij, Ris, & Holthuijsen, 1999). Wave growth due to wind is described by the combination of a linear and exponential component. Linear wave growth due to wind is described by the expression shown in Cavaleri and Malanotte-Rizzoli (1981), which is used to eliminate wave growth at frequencies lower than the Pierson-Moskowitz frequency. SWAN allows for two optional expressions of exponential wave growth due to wind. The first incorporates the expression due to Snyder et al. (1981) which was rescaled in terms of friction velocity U_* by Komen et al. (1984). The second incorporates the expression due to Janssen (1991) which accounts for the interaction between the wind and the waves by considering atmospheric boundary layer effects and the roughness length of the sea surface.

The two forms of nonlinear wave-wave interactions are accounted for in SWAN are triad wave-wave interaction and quadruplet wave-wave interactions. Quadruplet wave-wave interactions dominate the evolution of the wave spectrum in deep water where they transfer

wave energy from the spectral peak to lower frequencies and to higher frequencies. In shallow water, triad wave-wave interactions transfer energy from lower frequencies to higher frequencies. SWAN computes both quadruplet and triad non-linear interactions based on Hasselmann et al. (1985) and Eldeberky (1996) respectively.

Wave energy dissipation is made up of three terms: whitecapping, bottom friction, and depth induced breaking. White capping is primarily controlled by the steepness of the waves which is described by the pulse-based model of Hasselmann (1974). The bottom friction models incorporated by SWAN are the empirical Joint North Sea Wave Project (JONSWAP) model of Hasselmann et al. (1973), the drag law of Collins (1972), and the eddy-viscosity model of Madsen et al. (1988). The effect of a mean current on wave energy dissipation is not taken into account in SWAN. Dissipation due to depth-induced wave breaking is accounted for in SWAN by the bore-based model of Battjes and Janssen (1978). The maximum wave height calculated in SWAN is shown by the following relationship:

$$H_{max} = \gamma_b d \tag{3.2}$$

where γ_b is the breaking coefficient and d is the water depth.

SWAN discretizes the action balance equation in the geographic (x,y), and spectral (σ, θ) domain which creates a system of linear equations (Zijlema & van der Westhuysen, 2005). This system of equations can then be solved using a Gauss-Seidel iterative procedure (Wesseling, 1992).

3.3. Model Setup

3.3.1. Computational Grid

SWAN is compatible with both structured and unstructured computational grids. The unstructured computational grid that was developed by Renaissance Computing Institute (RENCI) for the North Carolina floodplain-mapping project was used for this study (Blanton & Luettich, 2008). This grid was used in the storm surge and tidal model, ADvanced CIRCulation (ADCIRC), which combines the computational grid and the input bathymetric grid into one file. The bathymetric data is relative to NAVD 88 with positive values indicating depth below water surface. The vertical extents of the original grid ranged from 45.82°N, near Nova Scotia in the north to 8.43°N, near South America, in the south. The horizontal extents of the original grid ranged from 97.86°W, in the Gulf of Mexico, in the east to 60.04°W, in the mid-Atlantic ocean, in the west shown in Figure III-3.1 below (Blanton B. O., 2008).

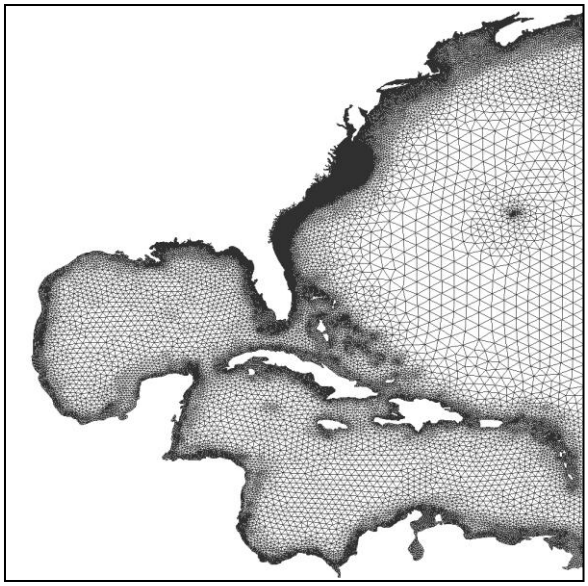

Figure III-3.1: RENCI computational grid (Blanton & Luettich, 2008)

This grid consists of 517,785 nodes and 1,020,109 elements. The extents of this domain were reduced to extend from the northern state boundary of North Carolina to just north of Cape Lookout in the south centering on Jennette's Pier in Nags Head. The vertical extents of the reduced grid were 36° 42.32' N to the north and 34° 45.73' N to the south. The horizontal extents of the reduced grid were 74° 30.10' W to the east and the North Carolina shoreline to the west. This was chosen based on the power distribution along the North Carolina coast based on the wave power analysis in section 2.3.2 as well as the emphasis of Jennette's Pier as a testing location. Also, the grid was refined in the vicinity of the virtual WEC array so SWAN could model the wave climate around the obstacles accurately. The final edited grid consisted of 30,573 nodes and 59,707 elements and transformed into State Plane NAD 83 projected coordinate system. The computational grid extends approximately 90 kilometers to the north and 126 kilometers to the south of Jennette's Pier in Nags Head.

Figure III-3.2 shows the location of the wave buoys used in this study and Jennette's Pier within the boundary of the computational grid.

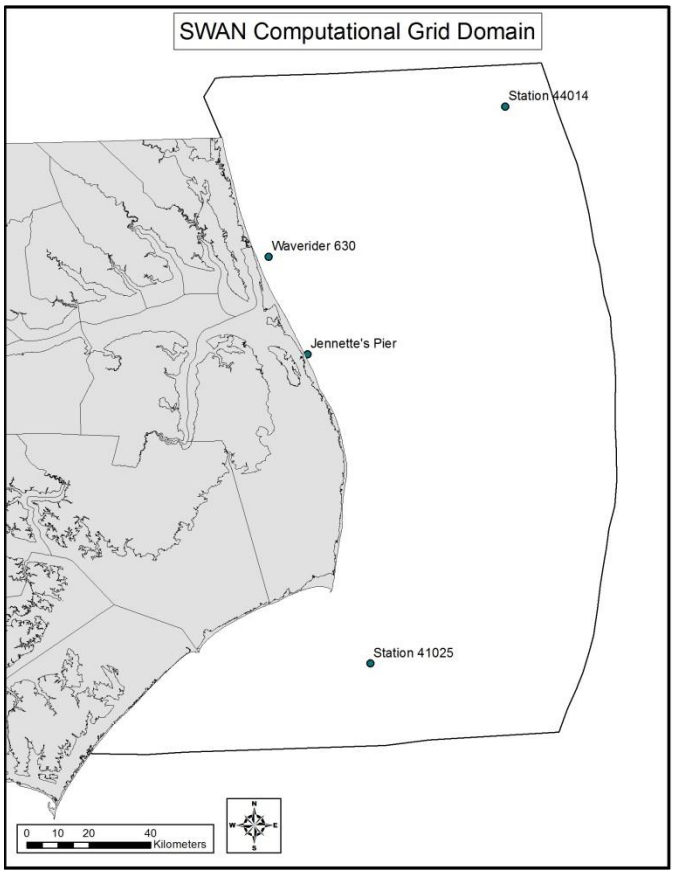

Figure III-3.2: Reduced RENCI computational grid and key locations for this study

The boundaries of the computational grid must also be defined in SWAN as either land or water. The land boundary does not generate any waves and it absorbs all incoming wave energy. The water boundary is where the boundary conditions are applied. Along sections of the water boundary where no boundary conditions are defined, SWAN assumes that no waves enter the computational grid and that waves can leave without obstruction. This

creates a shadow region where incorrect wave parameters would be calculated. The boundary was set far enough away from the site of interest to avoid an error propagating into this site.

3.3.2. Input Fields

The five input fields that SWAN accounts for are bathymetry, water level, current, friction, and wind. The bathymetric grid is combined with the ADCIRC unstructured computational grid. A constant water level of zero relative to NAVD 88 was assumed across the entire computational grid. An input grid for the current field was neglected due to a lack of data within the domain related to this parameter.

The bottom friction model chosen for SWAN to use was the empirical model of JONSWAP with a varying friction coefficient that depends on the frequency-dependent direction spreading (Hasselmann, et al., 1973). The friction coefficient was set to be $0.038 m^2 s^{-3}$ for frequencies with directional spreading less than or equal to 10 degrees which is identified with swell conditions (Hasselmann, et al., 1973). For frequencies with directional spreading greater than or equal to 30 degrees which is identified with wind-sea conditions, the friction coefficient was set to be $0.067\ m^2 s^{-3}$ (Bouws & Komen, 1983). For frequencies with the directional spreading between these values, the friction coefficient was linearly interpolated.

The wind input was defined as a constant across the entire computational grid. The wind data was taken from National Data Buoy Center at Station 44014. This location was chosen

due to its location offshore, which was assumed to be the driving wind force on the wave train propagating onshore. The wind data recorded at this location was measured at an elevation of five meters. SWAN requires a constant wind input to be measured at an elevation of 10 meters, which is the standard height used for wave hindcasting. The wind velocity profile is logarithmic in the vertical direction and equation 3.3 is used to convert to the appropriate anemometer height:

$$\frac{U_{10}}{U_z} = \left(\frac{10}{z}\right)^{1/7} \tag{3.3}$$

where U_{10} is the wind speed at 10 meters above water level, U_z is the wind speed at a given anemometry height z. Wind input was only used during the model validation runs.

3.3.3. Boundary Conditions

Boundary conditions are provided so that a numerical solution of the action balance equation can be obtained. This boundary condition is specified by a two-dimensional spectrum, which is applied to the up-wave boundaries in the SWAN model. The wave components of the up-wave boundaries can be accounted for in three ways: a parametric one-dimensional spectrum with a certain imposed directional distribution, a discrete one-dimensional spectrum with a certain imposed directional distribution, or a two-dimensional spectrum. The option used for this study is the parametric one-dimensional spectrum. Wave height, period, and direction were applied as the parametric data with an option to choose between three one-dimensional spectrum forms: a Pierson-Moskowitz spectrum (Pierson & Moskowitz, 1964), a JONSWAP

spectrum (Hasselmann, et al., 1973), and Gaussian-shaped spectrum. The JONSWAP spectrum was used to define the shape of the spectrum for this study and is defined as:

$$S_J(f) = \gamma^{e^a} \frac{\alpha_J g^2}{(2\pi)^4 f^5} e^{-\frac{5}{4}\left(\frac{f}{f_p}\right)^{-4}} \tag{3.4}$$

Where S_J is the JONSWAP spectrum for a given wave frequency f, γ is the peak enhancement factor, $\alpha_J$is the JONSWAP coefficient, g is the gravitational constant, and f_p is the peak frequency. The value assigned to α_J was 3.3. The imposed directional distribution was defined by:

$$D(\theta) = Acos^m(\theta - \theta_{peak}) \tag{3.5}$$

where m is related to the directional spread of the waves, A is a normalizing coefficient, θ is the wave direction, and θ_{peak} is the peak wave direction.

3.3.4. Model Physics

For this study, SWAN was run in third generation mode where the forms of wave generation, dissipation, and nonlinear wave-wave interactions are handled as previously described. Wave process, such as shoaling, refraction, and depth-induced breaking are included in the computation. The depth-induced breaking parameter, γ_b, was set to equal 0.78 based on McCowan (1891). Wave setup cannot be used when working with an unstructured grid; therefore, it was not included.

3.3.5. Output

Parametric

The three SWAN output wave parameters that were used were significant wave height, peak period, and mean wave direction. SWAN defines significant wave height as:

$$H_s = 4\sqrt{\iint E(\omega,\theta)d\omega d\theta} \tag{3.6}$$

where $E(\omega,\theta)$ is the variance density spectrum and ω is the absolute radian frequency and θ is the wave direction. This wave height is the same wave height measured at the wave buoys. The peak period is related to the absolute maximum bin of the variance density spectrum. The peak period output from SWAN is calculated the same way at the wave buoy. The peak direction is defined as the direction associated with the max of $E(\theta)$. The mean wave direction is defined as:

$$DIR = \arctan\left[\frac{\int \sin\theta E(\sigma,\theta)d\sigma d\theta}{\int \cos\theta E(\sigma,\theta)d\sigma d\theta}\right] \tag{3.7}$$

The direction was set to the nautical convention, which defines the direction where the waves are coming from and is measured clockwise from geographic north. This convention defines north as zero degrees, where the x-axis of the coordinate plane aligns to east. It was important to have the same output data from SWAN as was found at the buoys in order to compare the two data sets.

Spectral

SWAN is capable of calculating both one dimensional (m^2/Hz) spectrum and two dimensional (m^2/Hz/Deg) energy density spectrum based on the variance, both of which were

used in the model validation. The frequency range chosen for both the 1D and 2D spectral energy density plots was between 0.03 hertz and 1 hertz. For the computation of nonlinear quadruplet wave interactions to be accurate, the frequency resolution, $\Delta f/f$, must be set to equal 10%. The number of divisions between the frequency range (msc) was calculated by:

$$msc = \frac{\log\left(\frac{f_{high}}{f_{low}}\right)}{\log\left(1+{}^{\Delta f}/_{f}\right)} \tag{3.8}$$

which resulted in 37 division. The frequency distribution is unevenly spaced across the range because of the logarithmic relationship. The directional resolution was set to be five degrees over the full 360 degrees.

3.4. Modeling Methodology

3.4.1. Model Validation

It is important to validate that SWAN accurately represents the propagation of waves from the offshore regime to the nearshore regime at the study site before moving on to the next phase of this study. To validate the correct wave propagation across the bathymetry, multiple test cases were formed from the NOAA Station 44014. This station is located in deep water and will serve as the source for the boundary conditions for SWAN. The output parametric wave conditions from SWAN were compared to the measured wave conditions at two validation locations: the Waverider 630 buoy and NOAA Station 41025 off Diamond Shoals. The wave parameters used in this comparison were the significant wave height, peak wave period, and mean wave direction as defined in section 3.5. These parameters were manually chosen to meet specified criteria. First, one wave condition must be chosen at each of the

following wave directions: Northeast (approximately 45 degrees), East (approximately 90 degrees), and Southeast (approximately 135 degrees). Next, the conditions at the time steps a few hours before and after the condition chosen must be fairly consistent. The model performance analysis described by Ris et al. (1999) was used in this study to calculate the scatter index (SI) and the model performance index (MPI) of the model. To further validate the model, 1-D and 2-D spectral output data from SWAN was compared to measured spectral data at the two validation locations.

3.4.1.1. Boundary Conditions

The boundary conditions were chosen from Station 44014 from two different years due to the limited data available at the two validation locations. The 2-D spectral data at the Waverider 630 buoy was only available during 1999. Therefore, 1999 was chosen as the first year to locate the boundary conditions that meet the previous requirements. Since Station 41025 only has data available back to 2003, this station was not analyzed for the 1999 cases. The second year chosen was 2008 because the parametric wave data was available at both validation locations and the 1-D spectral data was available at Station 41025. The wind data was taken from Station 44014 and applied as a constant throughout the entire computational domain. The compiled list of boundary conditions is shown in Table III-4.1 below.

Table III-4.1: Boundary conditions for model validation

Case #	Date	Time (UTC)	H_{mo} (m)	T_p (sec)	Mean Wave Dir (deg)	Wind Speed U10 (m/s)	Wind Direction (deg)
1	6/17/1999	11:00	1.98	7.69	44.0	6.29	49.0
2	5/18/1999	12:00	2.04	10.00	96.0	5.52	10.0
3	9/7/1999	7:00	1.47	6.25	139.0	6.40	53.0
4	5/14/2008	3:50	3.92	12.90	49.0	4.09	337.0
5	3/18/2008	11:50	2.18	12.12	92.0	5.41	39.0
6	7/12/2008	6:50	1.18	12.12	135.0	4.97	41.0

These six boundary conditions were applied to the nodes along the boundary that correlated to deep water for each condition. This deep water limit was found by the deep water relationship of $d/L_o = 0.5$, where L_o is the deep water wave length calculated by:

$$L_o = \frac{gT^2}{2\pi} \tag{3.9}$$

3.4.2. Coastal Processes Analysis

SWAN was used to examine the effects a WEC array would have on coastal processes caused solely by wave action at Jennette's Pier. The three main effects of interest are wave height change, longshore current change, and longshore transport change along the shoreline. These changes could affect the sediment transport in this region. Wave height change alongshore was examined by Millar et al. (2007) to assess the impact on popular surfing locations. Being that the Outer Banks of North Carolina attracts surfers from across the nation, due diligence needs to be taken to analyze the possible effects a WEC array would have on popular surfing locations, including Jennette's Pier. Analysis nodes were defined

alongshore where the values of wave height, longshore current, and longshore transport were calculated. These nodes were centered on Jennette's pier to analyze the effective range that the WEC array would have on the areas north and south of the pier. The average spacing of these nodes was 132 meters, which is representative of the grid resolution along the shoreline in this region. The main differences between the modeling approach taken by Millar et al. (2007) and Oskamp et al. (2010), and the modeling approach in this study, is in the application of the unstructured computational grid. The unstructured grid allows for a variable resolution throughout the grid with areas of higher resolution for complex regions. This negates the need for grid nesting to achieve a higher resolution around the WEC array.

3.4.2.1. Boundary Conditions

The boundary conditions for the coastal processes analysis portion of the study were chosen based on the wave record at Station 44014. Wave data was acquired from 2005 through 2010 and analyzed based on specific wave directions. The wave directions were set to be 45 degrees (Northeast), 90 degrees (East), and 135 degrees (Southeast) to represent the three general approach angles of waves into this region. Each direction was set as the midpoint of a 30 degree bin. Only the wave heights and periods that fell into the directional bin were taken. The mean of the remaining wave parameters was taken over the six year history, which produced a representative wave height and period for each of the directional bins. To analyze the response of the WEC array from a single wave height and period, the average of the three mean values was taken. The resulting wave parameters used for the boundary conditions in the shoreline change analysis are listed in Table III-4.2.

Table III-4.2: Boundary conditions for shoreline change analysis

Boundary Condition	Wave Height H_{mo} (m)	Peak Period T_p (sec)	Direction (deg)
Northeast	1.5	8.8 s	45
East	1.5	8.8 s	90
Southeast	1.5	8.8 s	135

No wind input was defined for this section of the analysis because of the emphasis to show wave-induced shoreline change. These boundary conditions were applied to the nodes along the boundary of the computational grid associated with deep water. This was done by using equation 3.9 and the deep water relationship.

3.4.2.2. Obstacle

SWAN has the ability to model wave transmission through coastal structures such breakwaters. For this study, the WECs were represented as a line structure using the Obstacle command in SWAN. For SWAN to accurately model an obstacle, the obstacle line must intersect a computational grid line and must not intersect a computational grid node. SWAN reduces the wave height of the wave propagating through the obstacle and takes into account wave diffraction around the ends of the obstacle. The specific wave-device interactions are not modeled in SWAN. Each line was assigned a constant transmission coefficient that ranges between zero, meaning no transmission, and one, meaning complete transmission. The transmission coefficient represents the efficiency of the device, which is the percentage of wave energy that is converted to mechanical energy by the device. Each

device has a defined transmission coefficient of 0.85. This was based on the assumption of a 15% wave to mechanical energy conversion (Bedard, et al., 2007).

3.4.2.2.1. WEC Array Layout

The dimensions of each device were set to represent a surge WEC. The length of each WEC was set to 16 meters and was oriented parallel to the shoreline approximately one kilometer offshore in a depth of 12 meters. The midpoint of each WEC was set directly off a computational grid node within the refined region to ensure that the obstacle line crosses a computational grid line. The spacing between each node was approximately 40 meters leaving a gap of 24 meters between each WEC. The WEC array consisted of 36 devices that were arranged into three groups of 12. Each group of 12 devices consists of two rows of six as shown in Figure III-4.1.

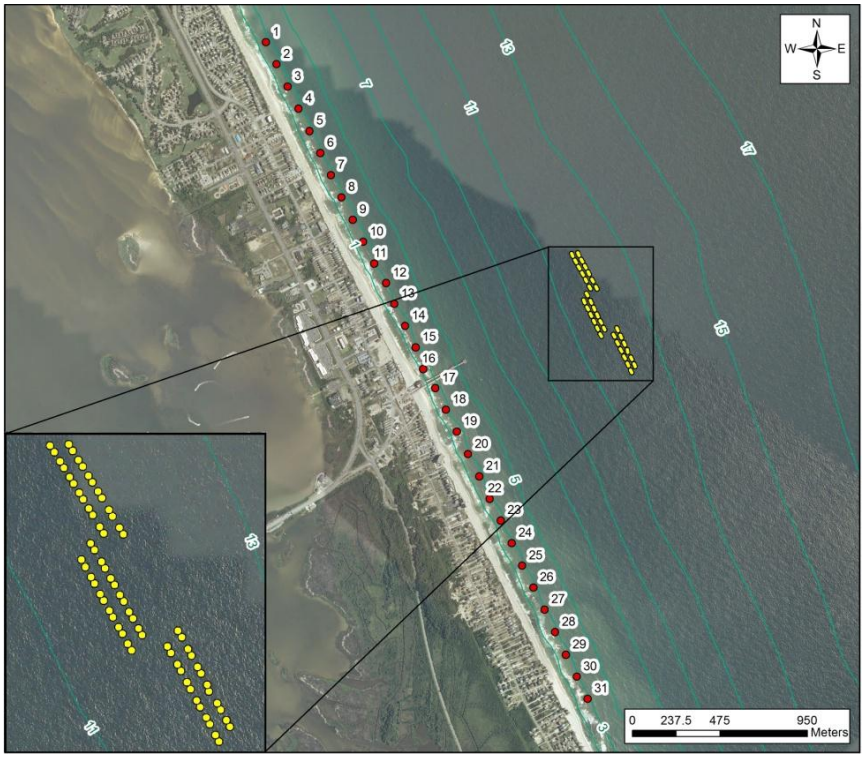

Figure III-4.1: WEC array and the 31 analysis nodes

3.4.2.3. Longshore Current

Longshore currents are generated by waves traveling at an oblique angle relative to the shoreline orientation. These currents are associated with the longshore transport of sand, which is one of the most important nearshore processes contributing to beach morphology (U.S. Army Corps of Engineers, 2002). A sound understanding of how these processes change due to the deployment of a WEC array is crucial for determining potential areas of erosion and accretion. Longshore current values are at their maximum in the surf zone (U.S. Army Corps of Engineers, 2002). The cross-shore gradient in the radiation stress (S_{xy}) is the wave driving force behind the longshore current and is calculated using linear wave theory by:

$$S_{xy} = \frac{n}{8}\rho g H^2 \cos\alpha \sin\alpha \tag{3.10}$$

where n is the ratio of wave group speed and phase speed, H is wave height, and α is the wave crest angle relative to the bottom contours (Longuet-Higgins, 1970). Assuming longshore homogeneity in bathymetry and wave height, linear wave theory, small breaking wave angle, uniformly sloping beach, no lateral mixing, and saturated wave breaking through the surf zone, an analytical solution of longshore current was given by Longuet-Higgins (1970):

$$V = \frac{5\pi}{16}\frac{\tan\beta^*}{C_f}\gamma_b\sqrt{gd}\ \sin\alpha\cos\alpha \tag{3.11}$$

where V is the longshore current in m/s, C_f is the bottom friction coefficient, γ_b is the breaking coefficient, α is the wave crest angle relative to the bottom contours, and $\tan\beta^*$ is the beach slope modified for wave setup given by:

$$\tan\beta^* = \frac{\tan\beta}{1+(3\gamma_b^2/8)} \tag{3.12}$$

where $\tan\beta$ is the beach slope. The bottom friction coefficient was set to 0.01 (U.S. Army Corps of Engineers, 2002). Beach slope was measured based on the bathymetry starting at the WEC array and continuing to the zero contour. This value was found to be 0.011 and was applied to each of the calculations at the analysis nodes. Positive values of longshore current represent a shore parallel velocity to the north and negative values of longshore current represent a shore parallel velocity to the south. This is a conservative estimate where the calculated values of longshore current will be larger than the actual conditions. Even though this may be the case, the process of showing the potential effects is an important first step in analyzing the change in coastal processes.

3.4.2.4. Longshore Transport

To estimate the volumetric flow rate of sediment alongshore, Longshore transport should be examined. Longshore sediment transport was calculated using the CERC formula, which is based upon the longshore component of wave energy flux as outlined in the Coastal Engineering Manual (U.S. Army Corps of Engineers, 2002). Wave energy flux, or wave power, is calculated by:

$$P_l = \left(EC_g\right)_b \sin\alpha_b \cos\alpha_b$$

where E_b is the wave energy at breaking, and $C_{gb}$is the group velocity at breaking. The CERC formula calculates the immersed weight transport rate by:

$$I_l = KP_l$$

where K is the empirical proportionality coefficient. This coefficient was calculated based on the sediment size as defined by del Valle, Medina, and Losada (1993) by:

$$K = 1.4e^{(-2.5D_{50})}$$

where D_{50} is the median grain size. The median grain size in the northern Outer Banks was found to be between 0.25 and 0.5 millimeters (Rice, 2003). Therefore, 0.3 millimeters was chosen for this analysis. The immersed weight transport rate was converted to a volumetric flow rate by:

$$Q_l = \frac{I_l}{(\rho_s - \rho)g(1-n)}$$

where ρ_s is the density of the sediment, ρ is the density of water, g is the acceleration due to gravity, and n is the sediment porosity. A positive value of longshore transport represents a

shore parallel motion to the north and a negative value represents a shore parallel motion to the south.

3.5. Scour around WEC

The type of device that has been identified to suit North Carolina the best is the surge device. Since these devices are anchored to the sea floor, scour becomes an area of concern and its effects on the stability of the structure. To analyze the effects of scour, the WEC was assumed to behave similarly to a submerged breakwater. The wave field around a submerged breakwater has been evaluated on a mobile bed by Sanchez-Arcilla et al. (2000) with a specific emphasis on the scour on the front side. This was done in a large scale (1/6 scale) wave flume for five cases, which included a submerged and permeable breakwater with a freeboard of 0.25 meters, a permeable and impermeable breakwater with a freeboard of 0.0 meters, and an emerged permeable and impermeable breakwater with a freeboard of -0.75 meters. This correlates well to the different types of surge WEC designs, where some are completely submerged and impermeable, like the SurgeWEC from RME, and others are surface piercing and permeable, like the Oyster. The results from these runs identified breakwaters with higher reflective properties, such as negative freeboard and impermeability, as having the greatest amount of scour at the toe of the breakwater. The scour hole for this case was located under the antinode of the standing wave. As the freeboard decreased to zero, the scour influence moved farther offshore under the node of the standing wave. This case caused an accretion of sediment at the toe of the breakwater. For the 0.25 meter freeboard condition, the scour hole was located at the toe of the breakwater; however, it was

very small. The dominant factor contributing to large amounts of scour was the negative freeboard. The magnitude and location of the scour hole did not change significantly due to the permeability of the breakwater. Depending on the type of surge style WEC used, proper scour protection measures should be taken. Two forms of scour protection given by Sumer & Fredsøe (2002) are either a toe berm or a berm with an additional apron.

3.5.1. Analysis based on PEP Reef

The Town of Palm Beach, Florida installed a line of submerged breakwaters, known as a PEP (Prefabricated Erosion Prevention) reef, in attempts to stabilize a historically erosive beach (Dean, Chen, & Browder, 1997). The project area consisted of 330 units with dimensions of 1.8 meters high, 3.7 meters long and 4.6 m wide per unit. These units were deployed in a straight line with a total length of the 1260 meters with a gap of 66 meters near the north end. The units were located 73 meters from the seawall in a depth of 3 meters resulting in a freeboard of 1.2 meters. Twenty eight scour rods were deployed throughout the area on both sides of the PEP reef and were inspected 6 times throughout the project life from July 29, 1993 through June 6, 1995. Results from the scour measurements found an average scour rate of 13 centimeters per month. Wave gages deployed within the study region measured a 10% reduction in wave height on average resulting in a transmission coefficient ranging between 0.85 and 0.95. The PEP reef had the opposite effect of what was intended. The beach behind the PEP reef eroded significantly creating an additional erosion rate above the background erosion by approximately 130% (Dean, Chen, & Browder, 1997). Laboratory testing was carried out to understand the reasons for such a negative effect. The

three-dimensional wave basin modeling of the PEP reef showed the mass transport of waves pushed water over the reef created ponding effects in the lee of the reef. This was due to the impeding of the return flow by the submerged breakwater. Strong longshore currents were created which drove the longshore transport of sediment towards the end of the reef and offshore. These results are important to keep in mind when designing an array of nearshore WECs due to the similarities between these devices and submerged breakwaters. These results can be avoided if proper design steps are taken to understand the full range of processes occurring. This type of effect does not seem likely at the example WEC array off Jennette's pier. The main reason for this is because the WEC array is set in approximately 11 meters of depth and the depth of closure for North Carolina Outer Banks is 8 meters (Nicholls, Birkemeier, & Lee, 1998).

3.6. Results

3.6.1. Model Validation

SWAN was run for each of the six boundary conditions listed in Table III-4.1. The first model performance parameter used was the scatter index (SI) which is defined by:

$$SI = \frac{rms_{error}}{\bar{X}} \tag{3.13}$$

where:

$$rms_{error} = \sqrt{\frac{1}{N}\sum_N (X_n - Y_n)^2} \tag{3.14}$$

where X_n is the observed values, and Y_n is the computed values, N is the number of observations, and $\bar{X}$ is the averaged observation value. A scatter index value of zero

represents a perfect match. The second performance parameter used in this analysis is the model performance index (MPI). This index indicates the degree to which the model reproduces the observed wave change (Ris, Holthuijsen, & Booij, 1999). The MPI is defined by:

$$MPI = 1 - \frac{rms_{error}}{rms_{change}} \tag{3.15}$$

where:

$$rms_{change} = \sqrt{\frac{1}{N}\sum_N (X_n - X_i)^2} \tag{3.16}$$

where X_n is the observed value and X_i is the observed incident value. A perfect MPI value would be equal to 1 which would represent an exact match of the value. The two parameters that the MPI and SI were calculated for in the study by Ris et al. (1999) were significant wave height and mean wave period. Due to the lack of data for the mean wave period, MPI was only calculated for the wave height in this study. To compare the peak wave period and mean wave direction, the SI was calculated.

The parametric results from SWAN for each case are shown in Tables III-6.1 through III-6.6. The spectral results from SWAN for each case are shown below in Figures III-6.1 through III-6.6. The model performance parameters calculated are shown in Table III-6.7.

Table III-6.1: Case #1 results of wave parameters at observation location

Case #1	**H_{mo} (m)**	**T_p (s)**	**MWD (deg)**
NOAA Station 44014 11:00 UTC	1.98	7.69	44.0
Waverider 630 Observed 11:16 UTC	1.32	7.69	58.0
Waverider 630 SWAN Output	1.30	7.32	69.1

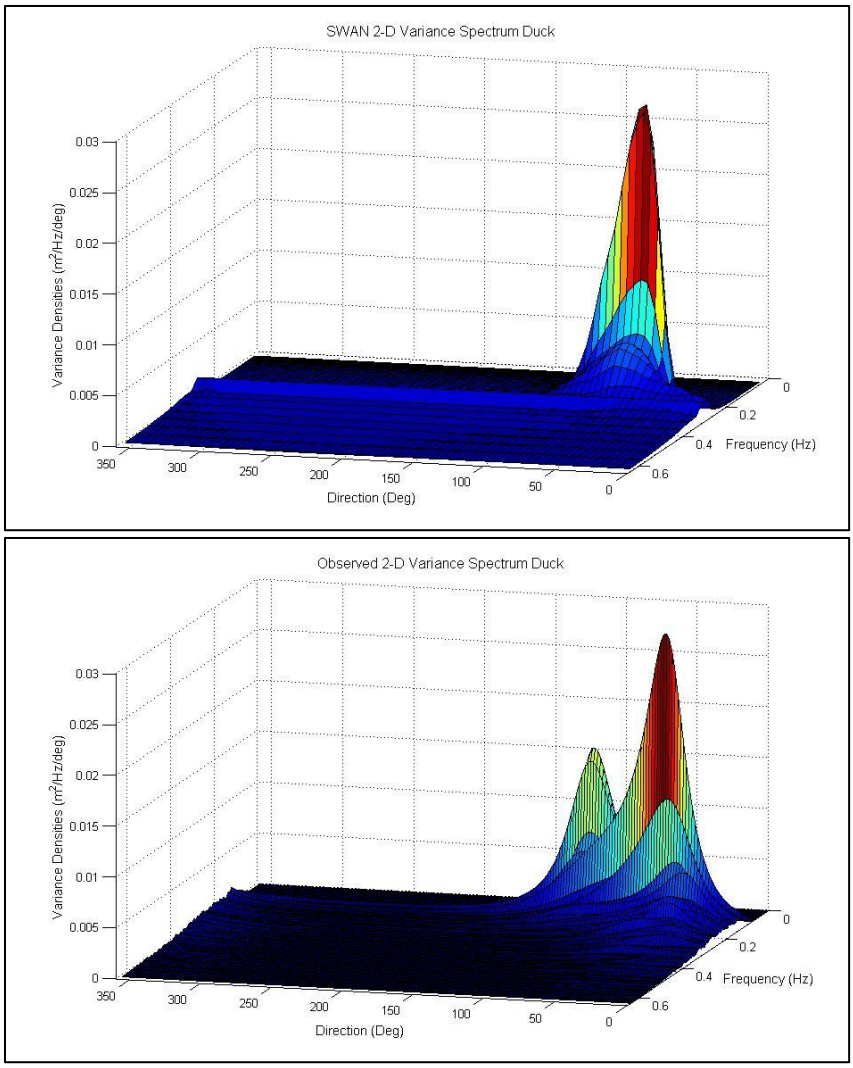

Figure III-6.1: Case #1 Observed 2-D (11:46 UTC) spectrum and SWAN 2-D Spectrum

Table III-6.2: Case #2 results of wave parameters at observation location

Case #2	H_{mo} (m)	T_p (s)	MWD (deg)
NOAA Station 4014 12:00 UTC	2.04	10.00	96.0
Waverider 630 Observed 12:35 UTC	1.53	10.00	90.0
Waverider 630 SWAN Output	1.54	9.72	80.0

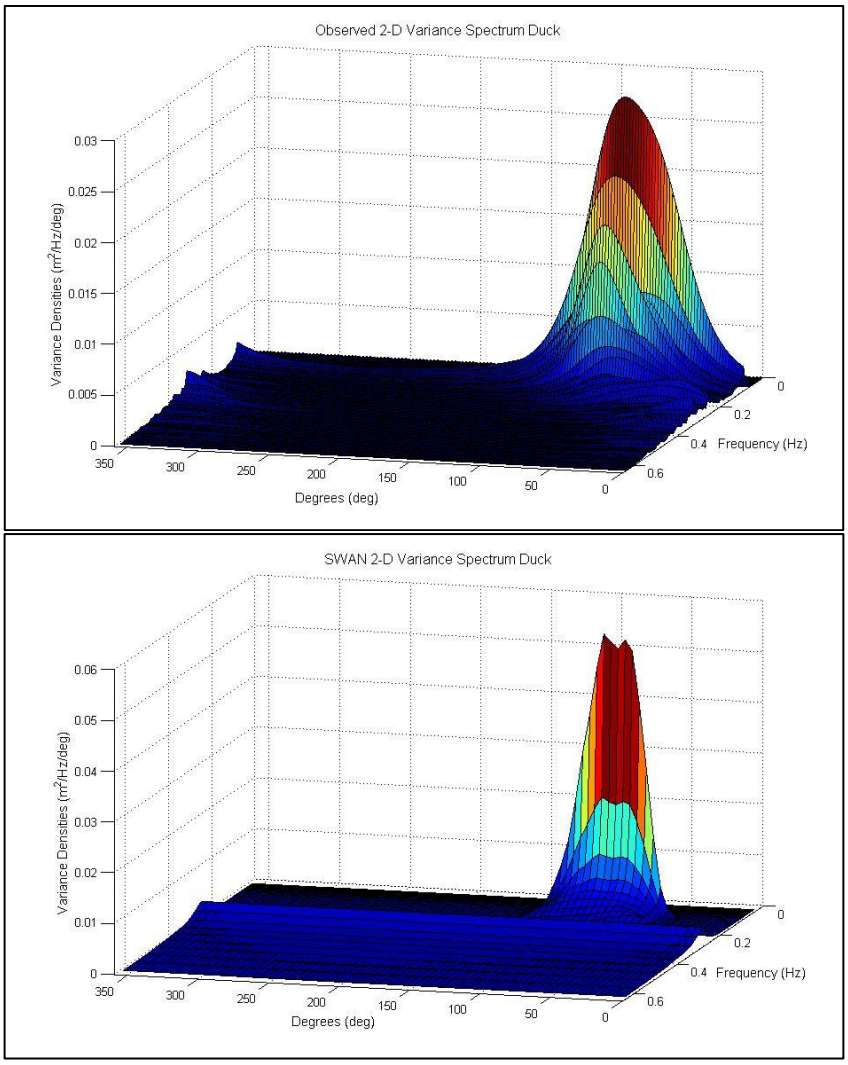

Figure III-6.2: Case #2 Observed 2-D (13:00 UTC) spectrum and SWAN 2-D Spectrum

Table III-6.3: Case #3 results of wave parameters at observation location

Case #3	H_{mo} (m)	T_p (s)	MWD (deg)
NOAA Station 44014 7:00 UTC	1.47	6.25	139.0
Waverider 630 Observed 7:08 UTC	1.08	6.25	114.0
Waverider 630 SWAN Output	1.03	6.05	122.4

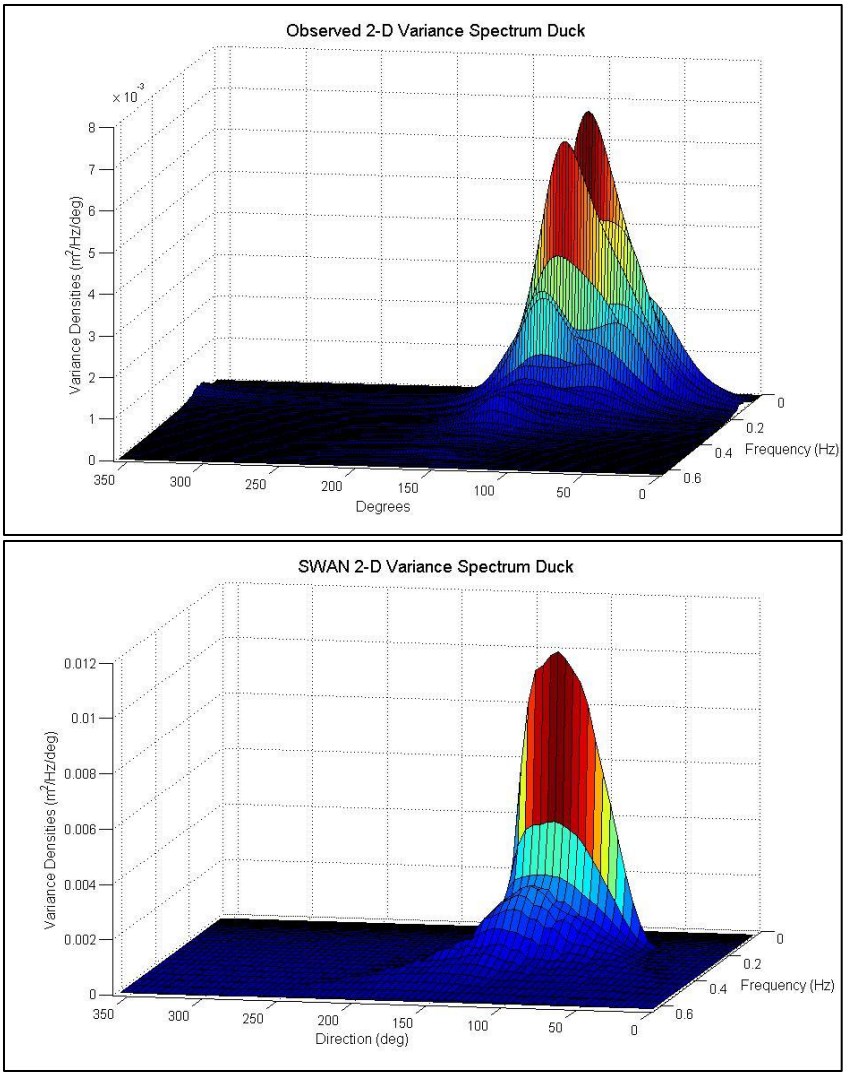

Figure III-6.3: Case #3 Observed 2-D (7:00 UTC) spectrum and SWAN 2-D Spectrum

Table III-6.4: Case #4 results of wave parameters at observation locations

Case #4	H_{mo} (m)	T_p (s)	MWD (deg)
NOAA Station 44014 3:50 UTC	3.92	12.90	49.0
Waverider 630 Observed 4:00 UTC	2.45	12.50	62.5
Waverider 630 SWAN Output	2.08	12.92	77.8
NOAA Station 41025 Observed 3:50 UTC	3.09	12.12	NA
NOAA Station 41025 SWAN Output	2.67	12.92	76.1

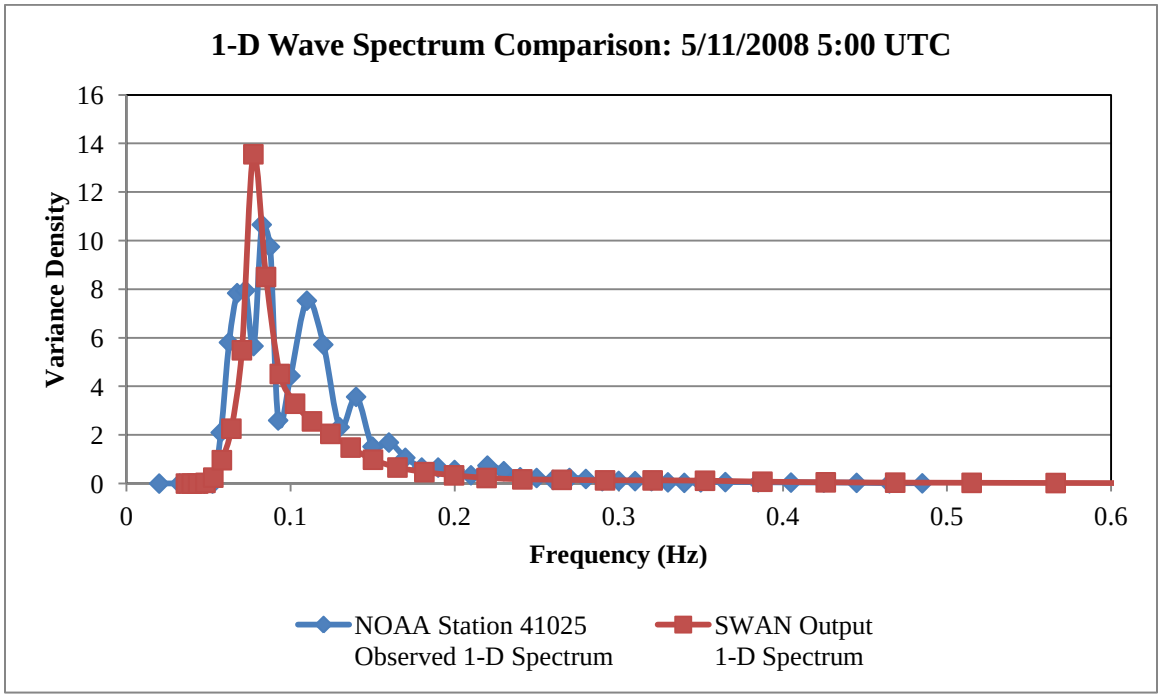

Figure III-6.4: Case #4 Observed 1-D spectrum and SWAN 1-D Spectrum

Table III-6.5: Case #5 results of wave parameters at observation location

Case #5	H_{mo} (m)	T_p (s)	MWD (deg)
NOAA Station 44014 11:50 UTC	2.18	12.12	92.0
Waverider 630 Observed 12:00 UTC	1.50	12.50	79.1
Waverider 630 SWAN Output	1.65	11.75	82.9
NOAA Station 41025 Observed 11:50 UTC	2.16	11.43	NA
NOAA Station 41025 SWAN Output	2.17	11.75	93.2

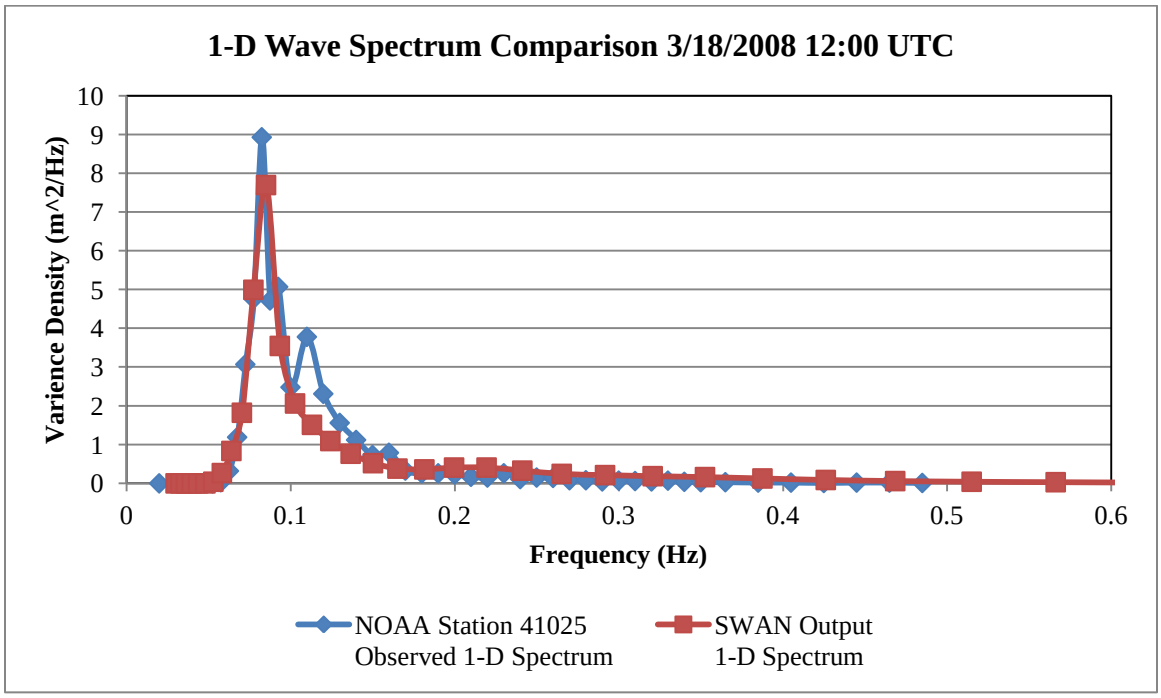

Figure III-6.5: Case #5 Observed 1-D spectrum and SWAN 1-D Spectrum

Table III-6.6: Case #6 results of wave parameters at observation location

Case #6	H_{mo} (m)	T_p (s)	MWD (deg)
NOAA Station 44014 6:50 UTC	1.18	12.12	135.0
Waverider 630 Observed 7:00 UTC	1.04	12.50	101.1
Waverider 630 SWAN Output	1.00	11.75	85.6
NOAA Station 41025 Observed 6:50 UTC	1.27	10.81	NA
NOAA Station 41025 SWAN Output	1.38	11.75	115.3

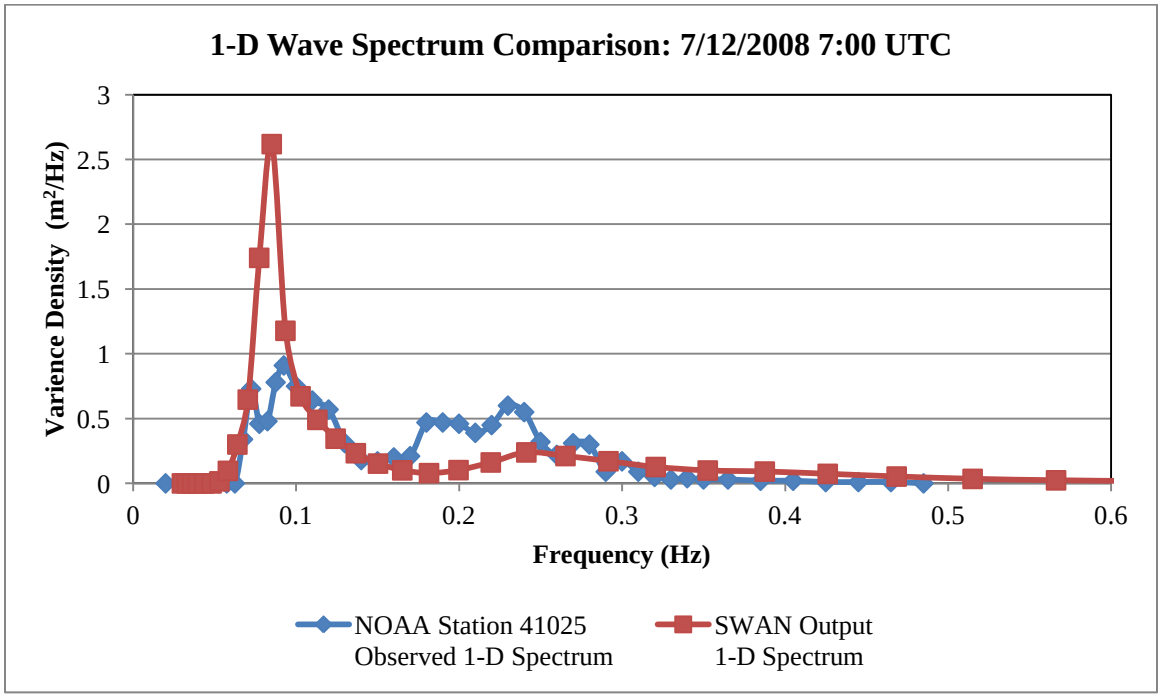

Figure III-6.6: Case #6 Observed 1-D spectrum and SWAN 1-D Spectrum

Table III-6.7: MPI and SI summary for each case

Case #	H_{mo} MPI	H_{mo} SI	T_p SI	MWD SI
1	0.97	0.02	0.05	0.19
2	0.98	0.01	0.03	0.11
3	0.87	0.05	0.03	0.07
4	0.75	0.17	0.04	0.25
5	0.72	0.08	0.01	0.05
6	0.54	0.08	0.01	0.15
Average	0.81	0.07	0.03	0.14

The values of MPI and SI found for H_{mo} and T_p in Cases 1-6 show a high performance of SWAN to model these parameters in this study area. The values of SI for mean wave direction showed a slightly higher error; however, not large enough to discount the validation of SWAN modeling this parameter. The spectral results from SWAN match the shape and peak values of the observed spectrum fairly well with an exception to Case #2, Case #3, and Case #6. In all three of these cases, the peak was over estimated. In Case #6, SWAN did not pick up the higher frequency wave conditions. The inconsistency could be accounted for in the assumptions made for the representation of the wind field over the domain, the lack of current data, or an accurate distribution of the wave climate along the boundary of the domain. Overall, the model performance was acceptable over the domain; therefore, the results from the wave analysis can be trusted as an accurate representation of the wave modeling for this study area.

3.6.2. Coastal Processes Analysis

The changes in wave height, longshore current, and longshore transport were calculated at each analysis node along the shoreline due to the WEC array. These nodes are located between 50 and 90 meters offshore in a depth between 2.17 and 3.41 meters and extend two kilometers to the north and south of Jennette's Pier. These changes were calculated by:

$$\Delta H_s = H_s - H_s'$$

$$\Delta V = V - V'$$

$$\Delta Q = Q - Q' \tag{3.17}$$

where H_s, V, and Q are the values of significant wave height and longshore current with the effects of the WEC array and H_s', V', and Q' are the values without the effects of the WEC array (Millar, Smith, & Reeve, 2007). The influence area of the WEC was established based on the percent change of the significant wave height calculated by:

$$\frac{\Delta H_s}{H_s} = \frac{H_s - H_s'}{H_s} \times 100\% \tag{3.18}$$

3.6.2.1. Wave Height Distribution

Northeast

Figure III-6.7 shows the effects of the WEC array had on the significant wave height from the northeast condition. The nodes shown in the figure labeled 1 through 31 are where the wave heights were recorded. As the waves propagate past the WEC array, the wave height dropped significantly behind the array, then began to rebuild as it continued to propagate towards the shoreline due to diffraction. This process was consistent for each of the three

wave conditions. This rebuilding process decreased the area of influence along the shoreline. The effects the WEC array had on the significant wave height were centered directly behind the array.

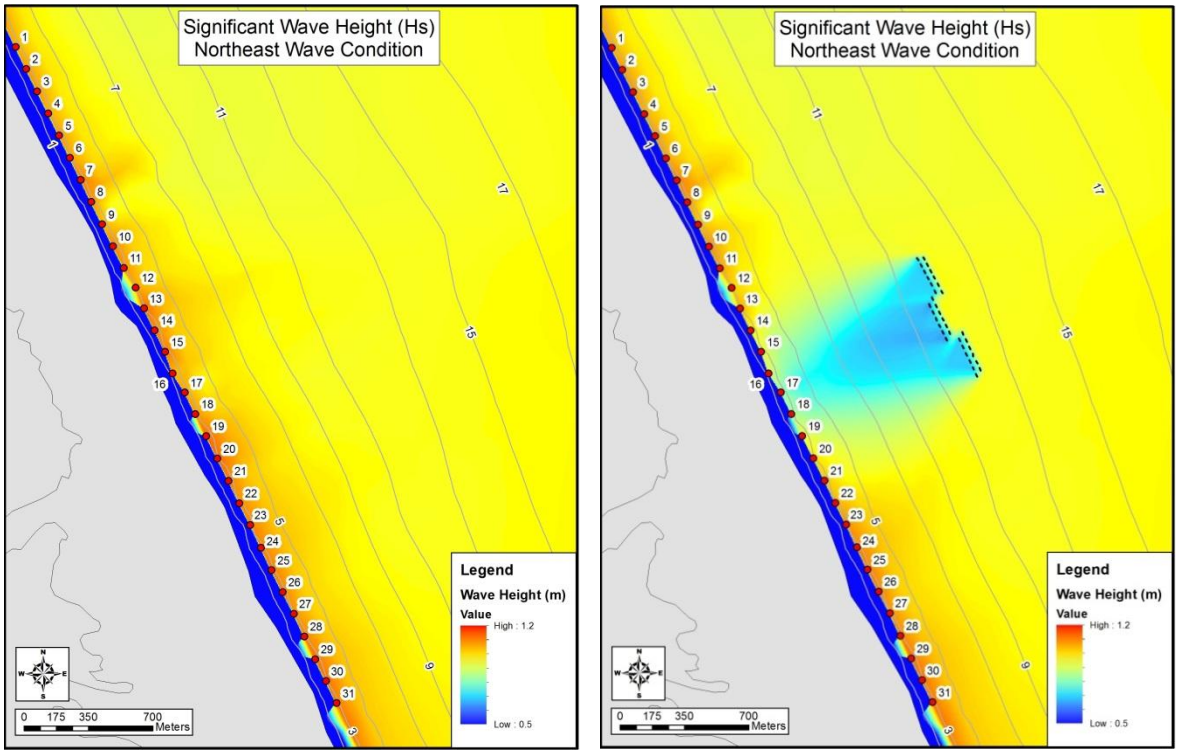

Figure III-6.7: WEC array influence on Hs from northeast wave condition

Figure III-6.8 shows the distribution of the significant wave height pre and post WEC, the difference of the two wave heights, and the percent change of the wave heights alongshore at the analysis nodes for the east condition. The maximum difference found from the northeast condition was a decrease of 0.24 meters which correlated to a 22.5% change from the initial condition. This was located at node 16 which was 84 meters north of Jennette's pier. The minimum value of the wave height due to the effects of the WEC array was 0.82 meters and was also located at node 16. The extent to which the percent change was at least 10% was

set as the area of influence. For the northeast condition, this was found to include nodes 13 through 20, which is approximately 772 meters wide. This condition has the widest area of influence out of the three conditions. The effects outside of this node range were minimal.

a.)

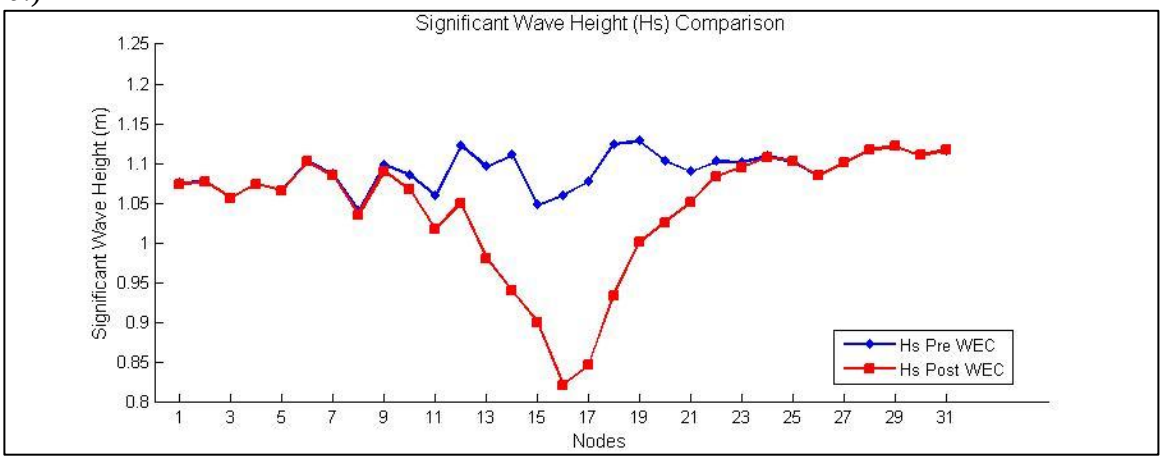

b.)

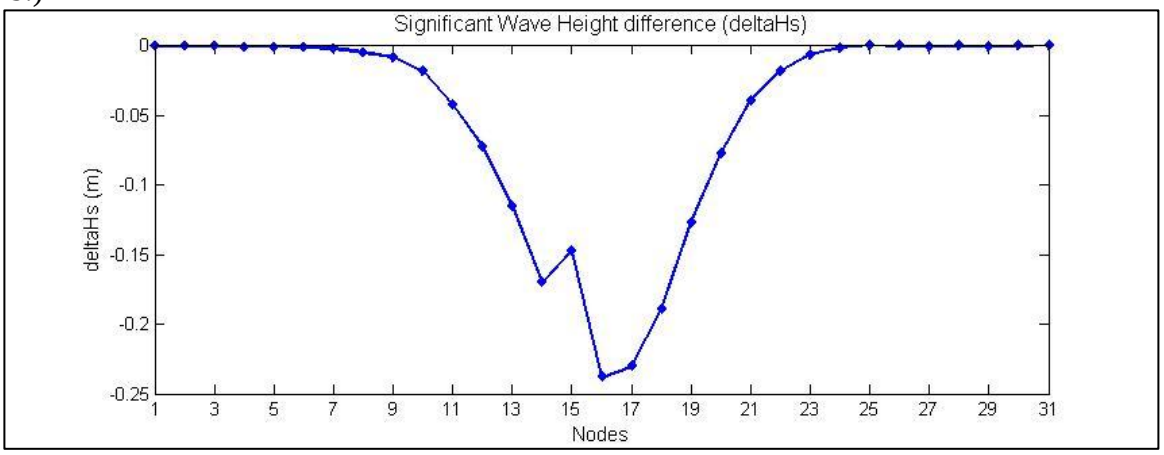

c.)

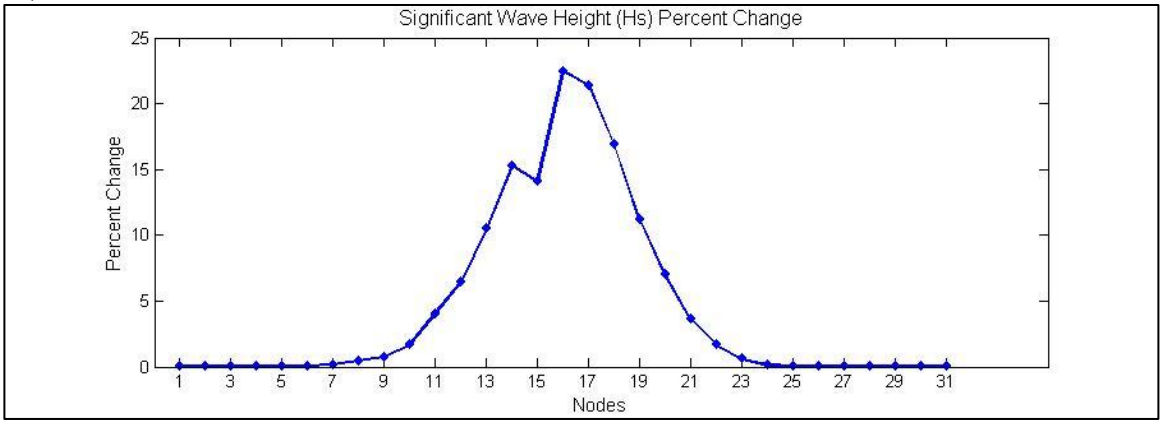

Figure III-6.8: Northeast condition results a) Significant wave height distribution along nodes Pre and Post WEC array b.) ΔH_s at the analysis nodes c.) $(\Delta Hs)/Hs$ at the analysis nodes

East

Figure III-6.9 shows the effects of the WEC array on the significant wave height for the east condition. The incident significant wave height at the WEC array from the east condition was larger than the northeast condition. The area affected by the WEC array was shifted to the north due to the larger incident angle.

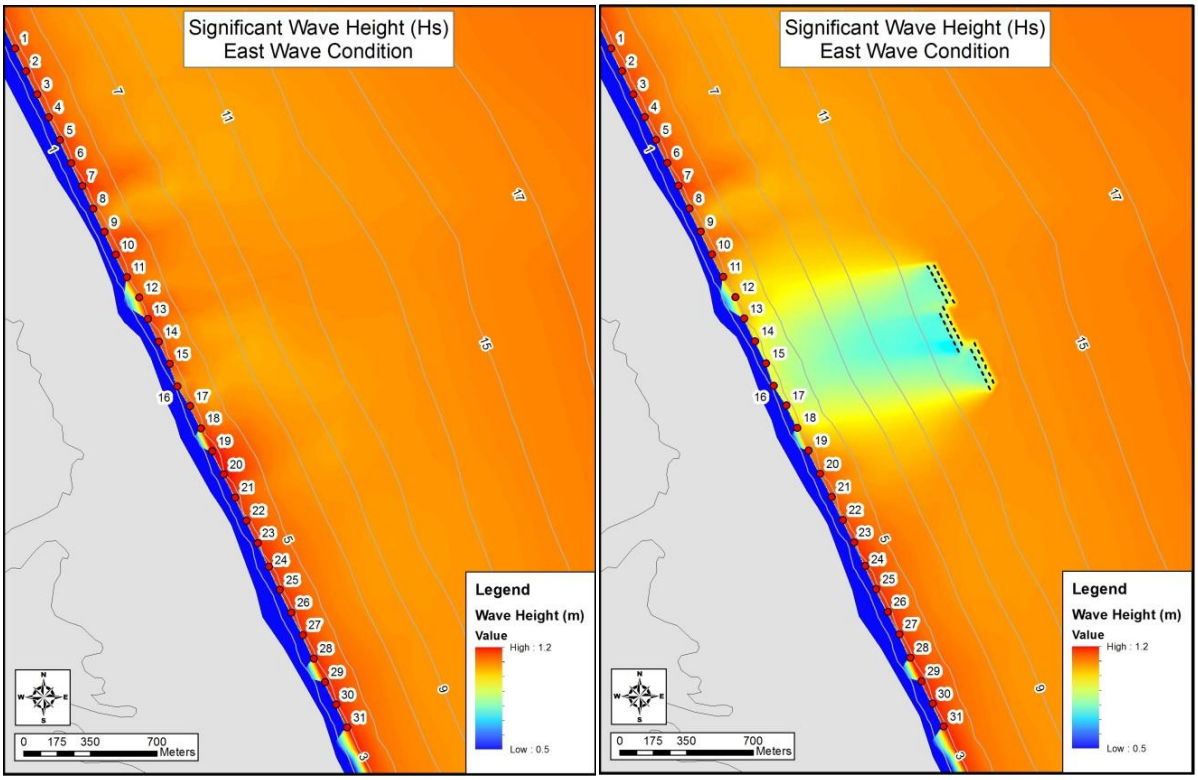

Figure III-6.9: WEC array influence on Hs from east wave condition

Figure III-6.10 shows the distribution of the significant wave height pre and post WEC array, the difference of the two wave heights, and the percent change of the wave heights alongshore at the analysis nodes for the east condition. The maximum difference found from the east condition was a decrease of 0.21 meters which correlated to an 18.0% change from

the initial condition. This was located at node 14, which was 318 meters to the north of Jennette's pier. The significant wave height with the effects of the WEC array at node 14 was 0.96; however, this was not the minimum wave height measured alongshore. The minimum significant wave height was found to be 0.93 meters and was located at node 15. The area of influence for the northeast condition was found to include nodes 11 through 17, which is approximately 753 meters wide. The wave heights found outside of this node range are very close to the wave heights found without the effects of the WEC array.

a.)

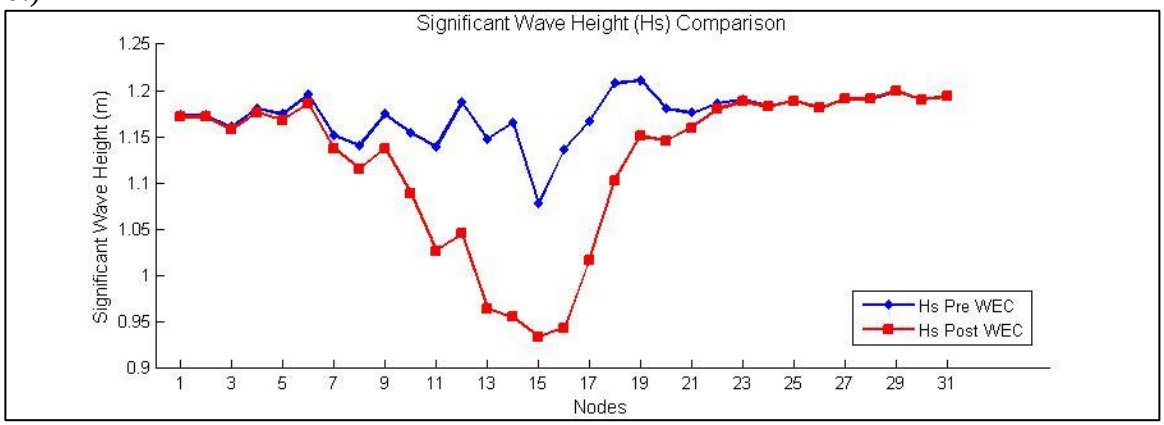

b.)

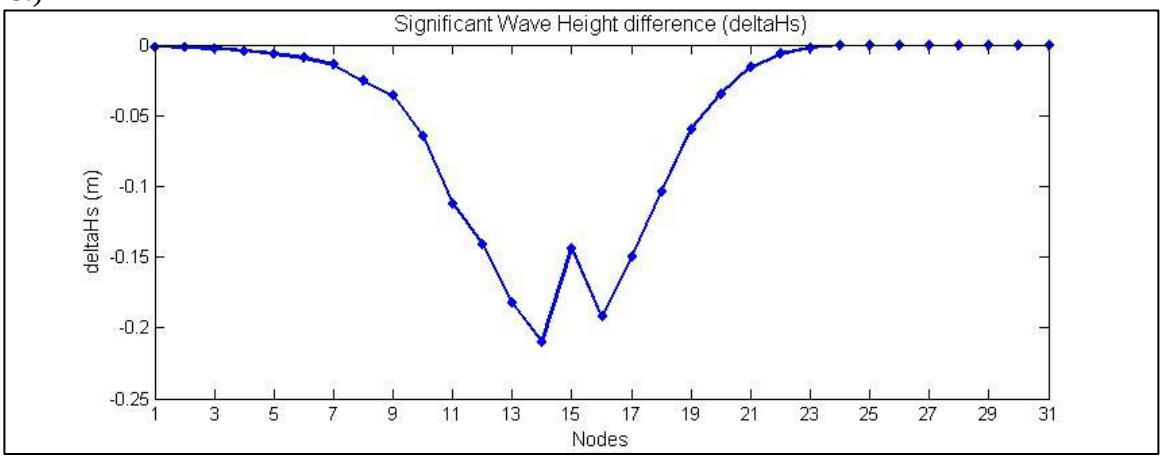

c.)

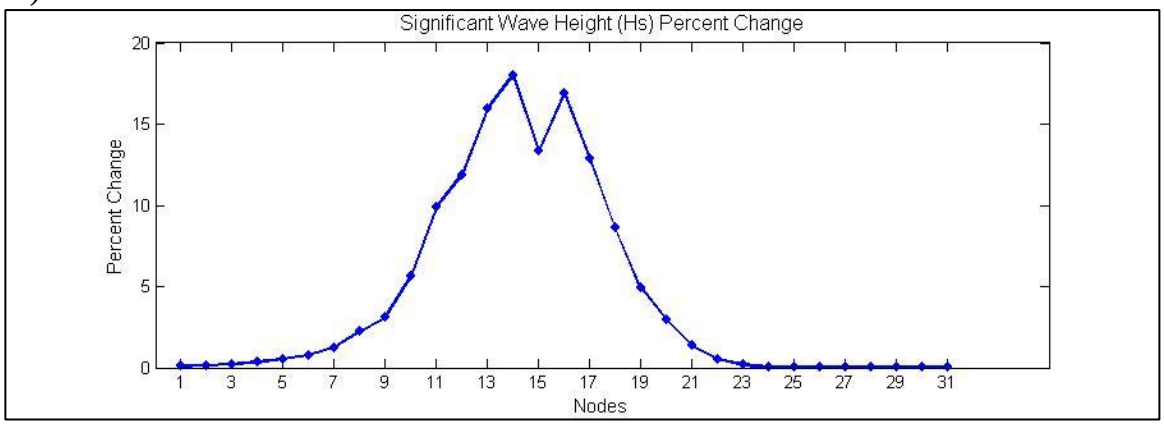

Figure III-6.10: East condition results a) Significant wave height distribution along nodes Pre and Post WEC array b.) ΔH_s at the analysis nodes c.) $(\Delta Hs)/Hs$ at the analysis nodes

Southeast

Figure III-6.11 shows the effects of the WEC array on the significant wave height for the southeast condition. The incident wave height at the WEC array from the southeast condition was the smallest of all three conditions. Being that this condition had the largest wave direction for the boundary condition, the area affected by the WEC array was shifted the farthest to the north.

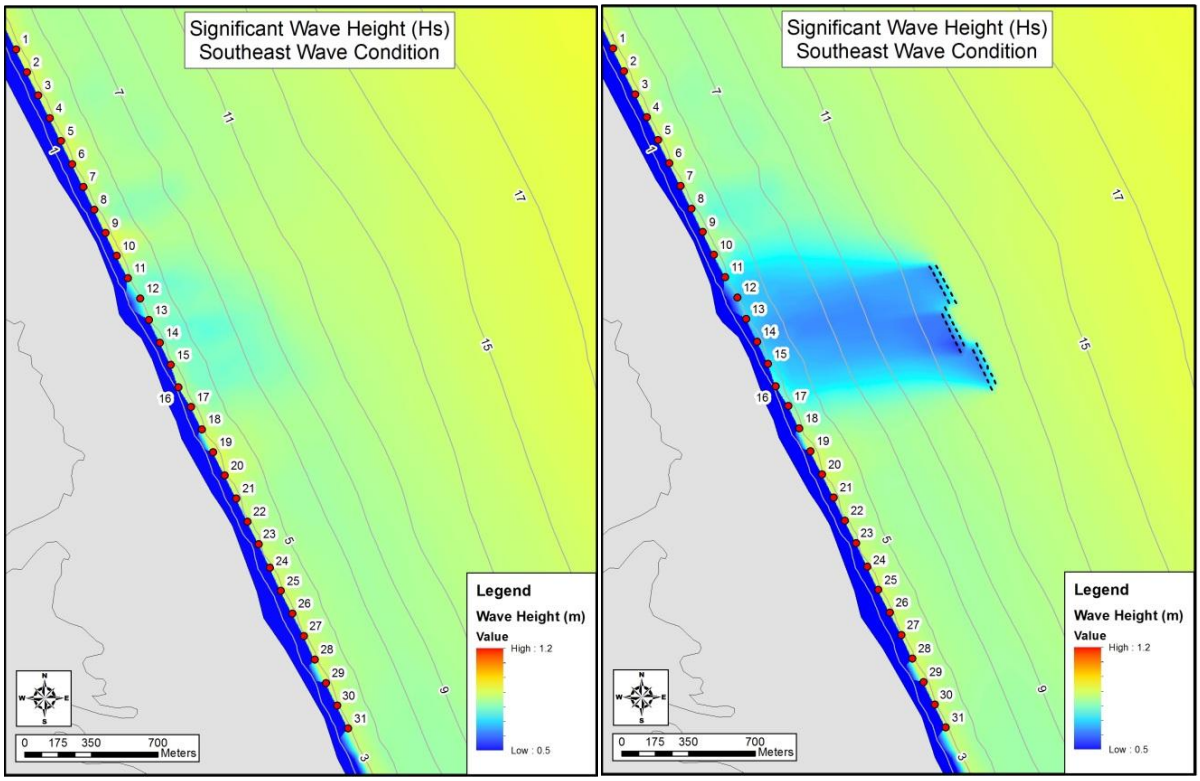

Figure III-6.11: WEC array influence on Hs from southeast wave condition

Figure III-6.12 shows the significant wave height pre and post WEC array, the difference of the two wave heights, and the percent change of the wave heights at the analysis nodes for the southeast condition. The maximum change found from the southeast condition was a

decrease of 0.13 meters, which correlated to a 15.7% change from the initial condition. This was located at node 13 which was 449 meters to the north of Jennette's pier. The significant wave height with the effects of the WEC array at node 13 was also the minimum alongshore and was found to be 0.96 meters. The area of influence for the southeast condition was found to include nodes 10 through 15, which is approximately 639 meters wide. This condition has the narrowest area of influence out of the three conditions. The wave heights found outside of this node range are very close to the wave heights found without the effects of the WEC array.

a.)

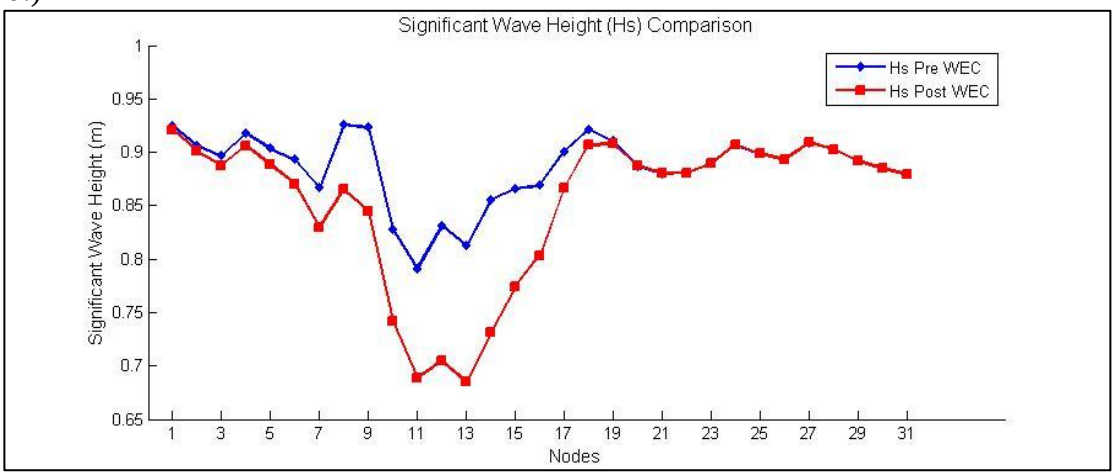

b.)

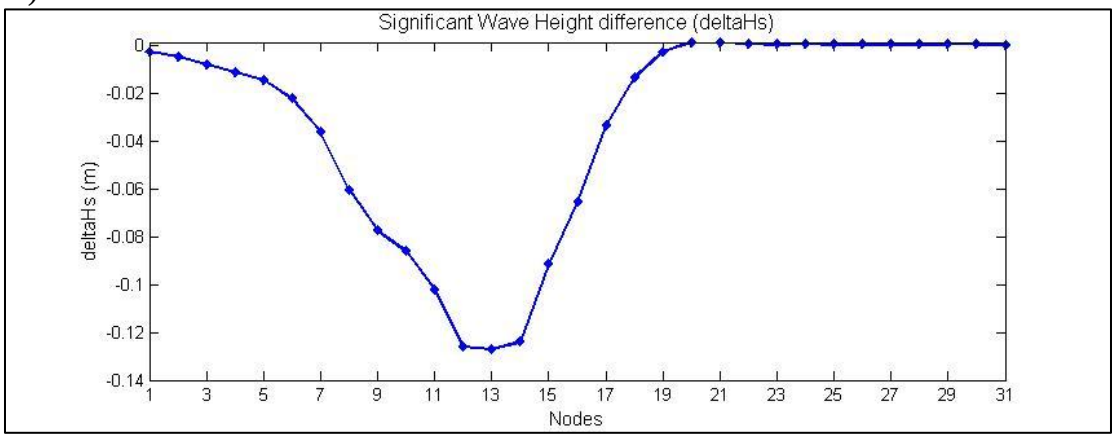

c.)

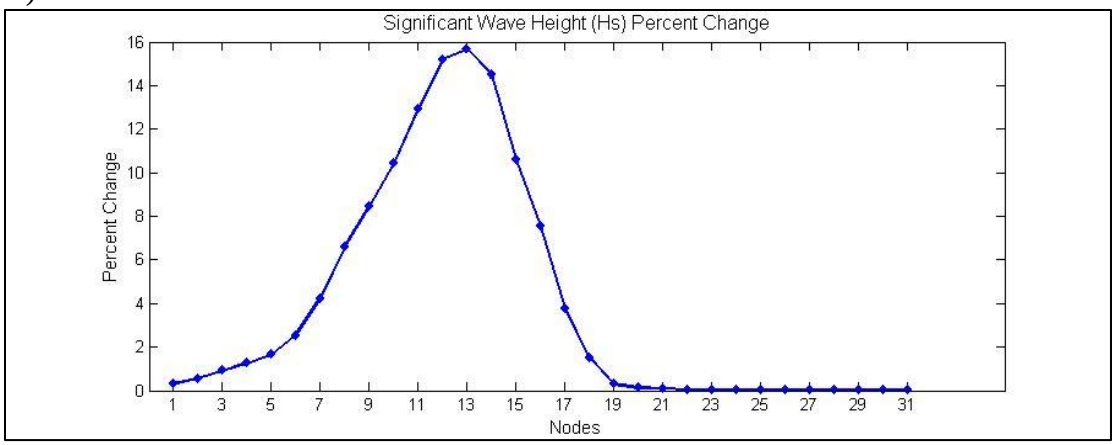

Figure III-6.12: Southeast condition results a) Significant wave height distribution along nodes Pre and Post WEC array b.) ΔH_s at the analysis nodes c.) $(\Delta Hs)/Hs$ at the analysis nodes

The areas of influence from each condition were combined yielding an overall area of influence. This was found by identifying the northernmost and southernmost node from all three conditions that had at least a 10% change in wave height. Those nodes were 10 and 19 and the distance between the two was 1148 meters. The center of the overall area of influence was located 254 meters north of Jennette's pier. This indicates that the majority of the impact on the nearshore wave height due to a WEC array deployed at this location will be shifted to the north.

3.6.2.2. Longshore Current

Northeast

The effects the WEC array had on the mean wave direction due to diffraction is shown in Figure III-6.13. The incident mean wave direction directly offshore of the WEC array was 66 degrees, which was approximately shore parallel. As the wave propagates past the WEC array, the mean wave direction decreases around the northern end of the array and increases around the southern end. Since longshore current is dependent on wave direction, this could impact the flow of sediment nearshore of the WEC array. From a visual analysis of Figure III-6.13, the effects of both ends of the WEC array meet in the middle nearshore of the array, which is consistent with the incident wave crest angle being parallel to the bottom contours.

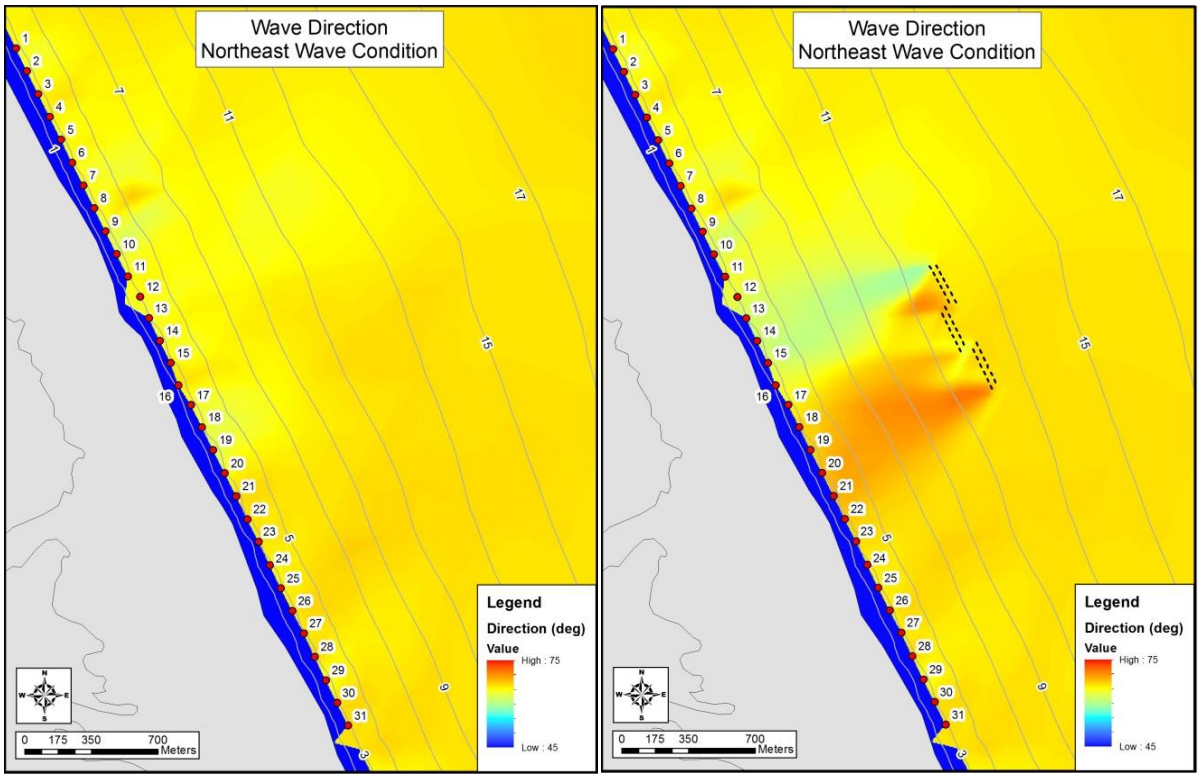

Figure III-6.13: WEC array influence on mean wave direction from northeast wave condition

Figure III-6.14 shows the longshore current generated from the northeast condition pre and post WEC array and their difference at the analysis nodes. The longshore current calculated without the influence of the WEC array oscillated about zero indicating a minimal current generated from the northeast condition. The effects of the WEC array produce a longshore current that is shore parallel to the north from the south end of the array and shore parallel to the south from the north end of the array. The maximum velocity calculated from the effects of the north end of the array was 16.4 cm/s to the south and was located at node 12. The maximum velocity calculated from the effects of the south end of the WEC array was 18.3 cm/s to the north and was located at node 20. These locations do not match the locations of the maximum and minimum change in longshore current. The magnitude and location of

these values due to the effects of the north and south end of the WEC array were an increase of 11.8 cm/s to the south at node 13 and an increase of 16.7 cm/s to the north at node 18 respectively. As the distance increases away from Jennette's Pier, the longshore current values with the effect of the WEC array align back up with the values without the array.

a.)

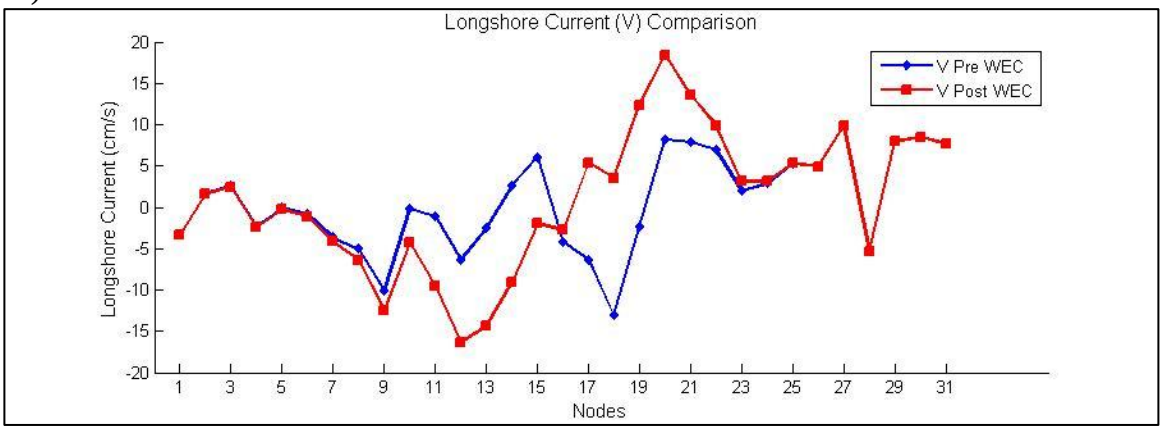

b.)

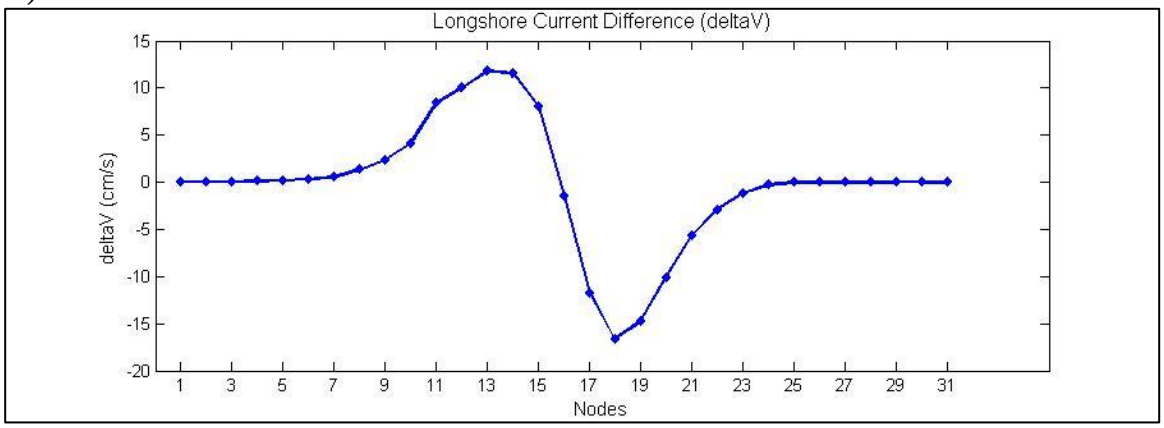

Figure III-6.14: Northeast condition results a) Longshore current distribution along nodes Pre and Post WEC array b.) ΔV at the analysis nodes

East

The effects the WEC array had on the mean wave direction is shown in Figure III-6.15. The evidence of diffraction can clearly be seen around the northern end and southern end of the array. The incident mean wave direction directly offshore of the array was 83 degrees, which was larger than the northeast condition. From a visual analysis of Figure III-6.15, the diffraction effects from the south end of the WEC array were dominant directly behind the WEC array. The diffraction effects from the north end of the WEC array were concentrated slightly north of the array. This was due to the incident wave angel being larger than the bottom contours.

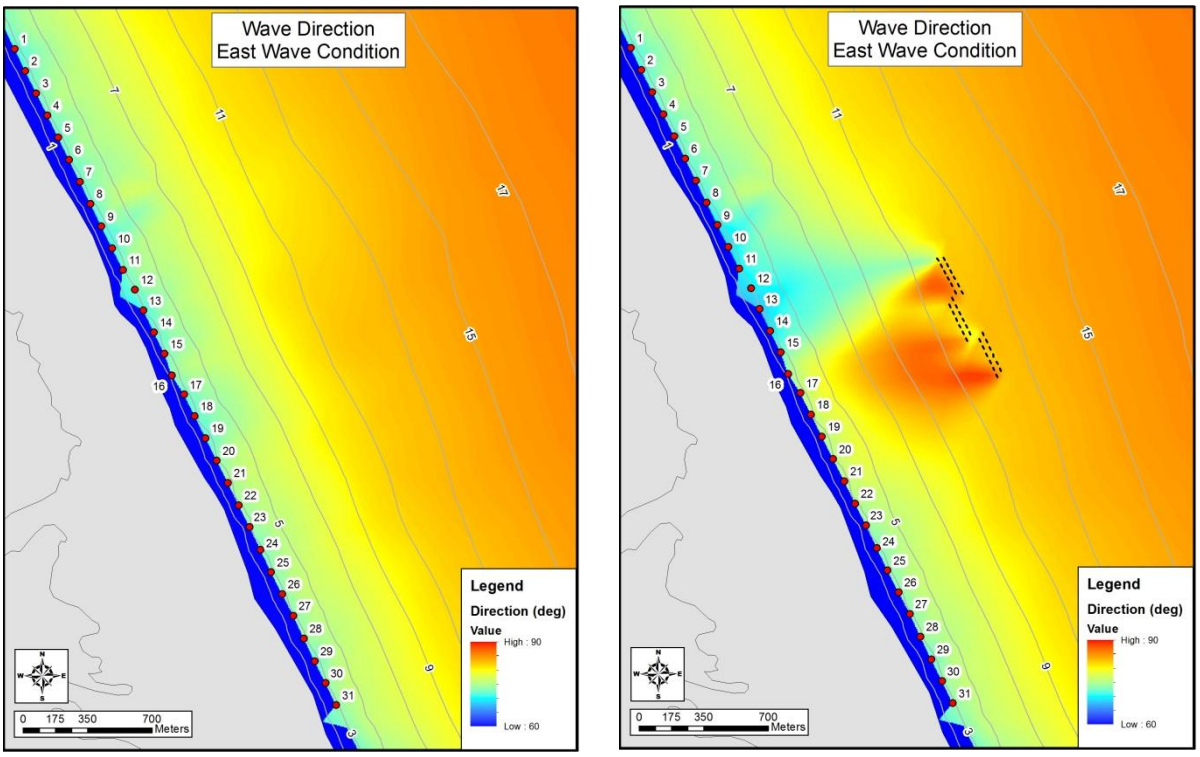

Figure III-6.15: WEC array influence on mean wave direction from east wave condition

Figure III-6.16 shows the longshore current generated from the east condition pre and post WEC array and their difference at the analysis nodes. The longshore current calculated without the influence of the WEC array had a net north direction. The effects of the WEC array increase the current velocity at the south end of the array and decrease the current velocity at the north end of the array. The WEC array does not decrease the longshore current enough to reverse the direction; therefore, the current remains in a net north direction. The maximum velocity calculated from the effects of the north end of the WEC array was 23.3 cm/s to the north and was located at node 12. The maximum velocity calculated from the effects of the south end of the WEC array was 64.1 cm/s to the north and was located at node 20. These locations do not match the locations of the maximum and minimum change in longshore current. The magnitude and location of these values due to the effects of the north and south end of the WEC array were a decrease of 15.6 cm/s to the north at node 11 and an increase of 16.4 cm/s to the north at node 17 respectively. As the distance from Jennette's pier increased in both directions, the longshore current due to the effect of the WEC array aligned with the values without the array.

a.)

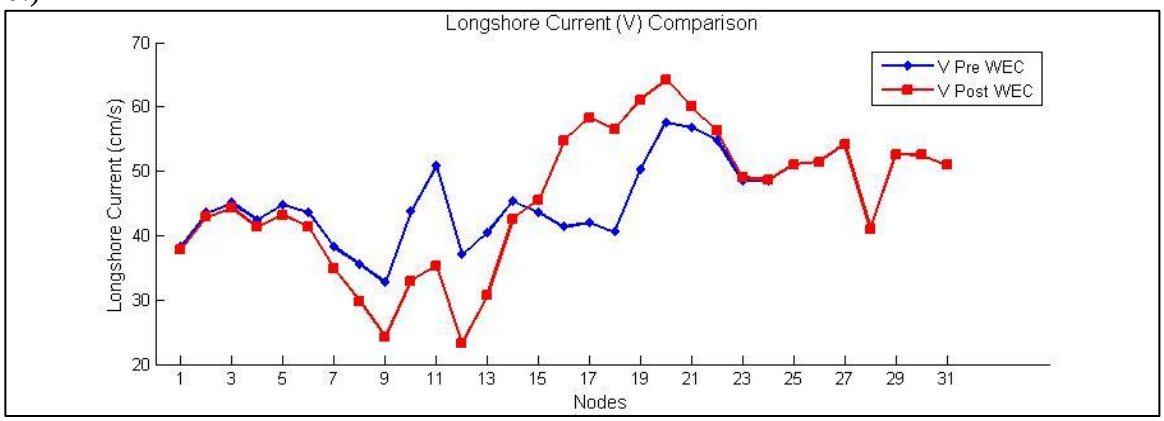

b.)

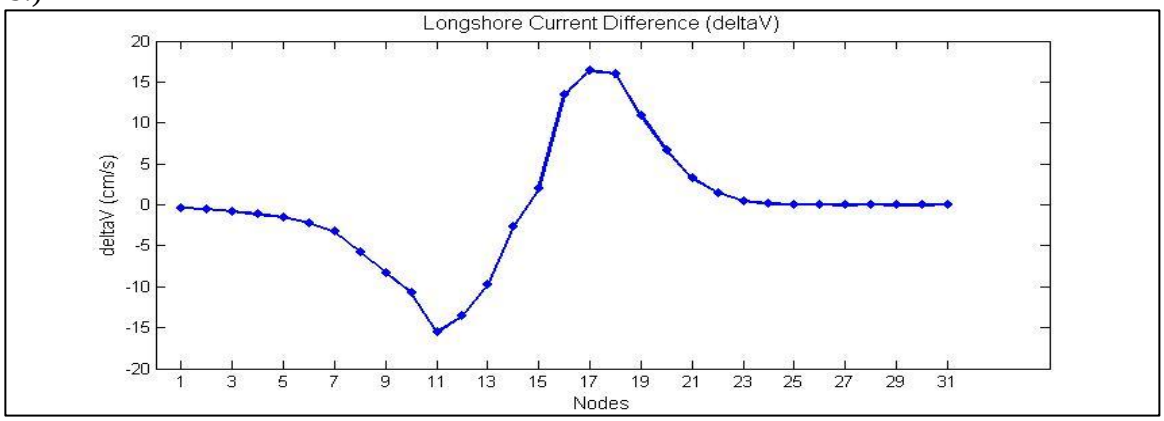

Figure III-6.16: East condition results a) Longshore current distribution along nodes Pre and Post WEC array b.) ΔV at the analysis nodes

Southeast

The effects the WEC array had on the mean wave direction is shown in Figure III-6.17. The incident mean wave direction directly offshore of the WEC array was approximately 103 degrees. As the wave propagates past the WEC array, the diffraction effects due to the southern end dominate nearshore. The diffraction effects due to the northern end are minimal because of the high incident wave angle. Due to the large difference between the

incident wave crest angle and the angle of the WEC array, the longshore current change due to diffraction is negligible.

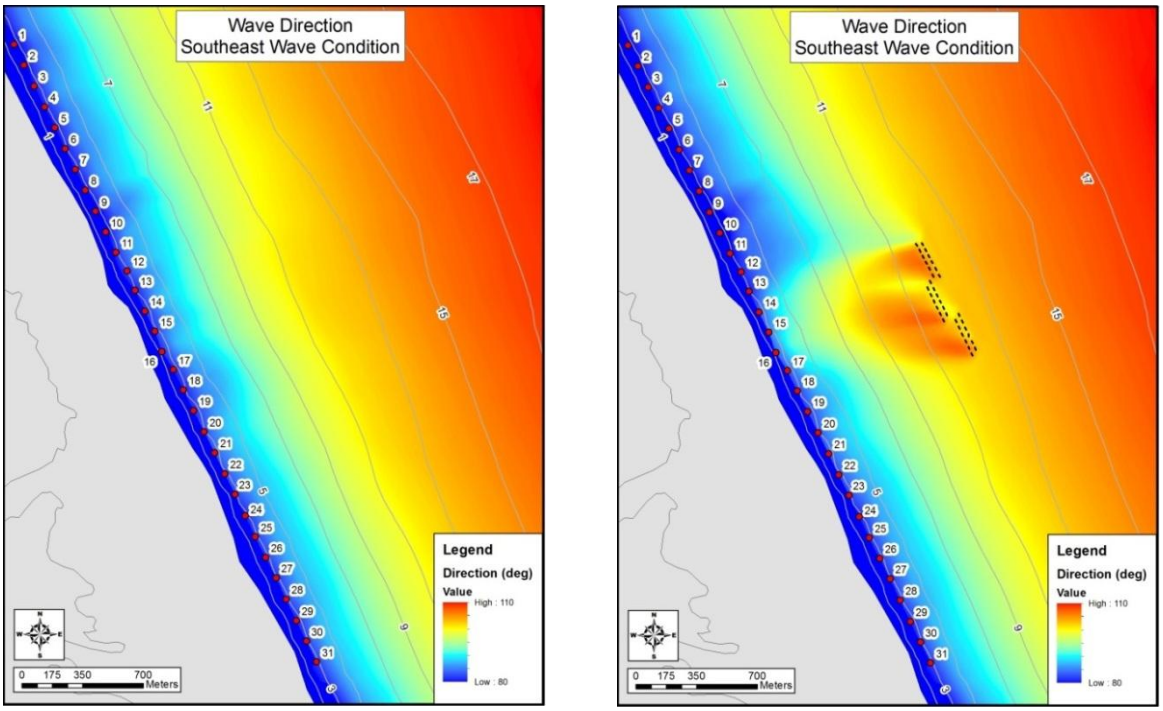

Figure III-6.17: WEC array influence on mean wave direction from southeast wave condition

Figure III-6.18 shows the longshore current generated from the southeast condition pre and post WEC array and their difference at the analysis nodes. The longshore current calculated without the influence of the WEC array had a net north direction, which was similar to the east condition. The effects of the WEC array increase the current velocity at the south end of the array and decrease the current velocity at the north end of the array. The WEC array does not affect the strong longshore current generated by the southeast condition enough to reverse the direction; therefore, the net direction of the current remains to the north. The maximum velocity calculated from the effects of the north end of the WEC array was 71.6

cm/s to the north and was located at node 8. The maximum velocity calculated from the effects of the south end of the WEC array was 110.5 cm/s to the north and was located at node 20. These locations do not match the locations of the maximum and minimum change in longshore current. The magnitude and location of these values due to the effects of the north and south end of the WEC array were a decrease of 7.4 cm/s to the south at node 9 and a decrease of 9.1 cm/s to the north at node 14 respectively. These differences are minimal compared to the strong current velocity. As the distance away from Jennette's pier increased, the longshore current due to the effect of the WEC array aligned back up with the values without the array.

a.)

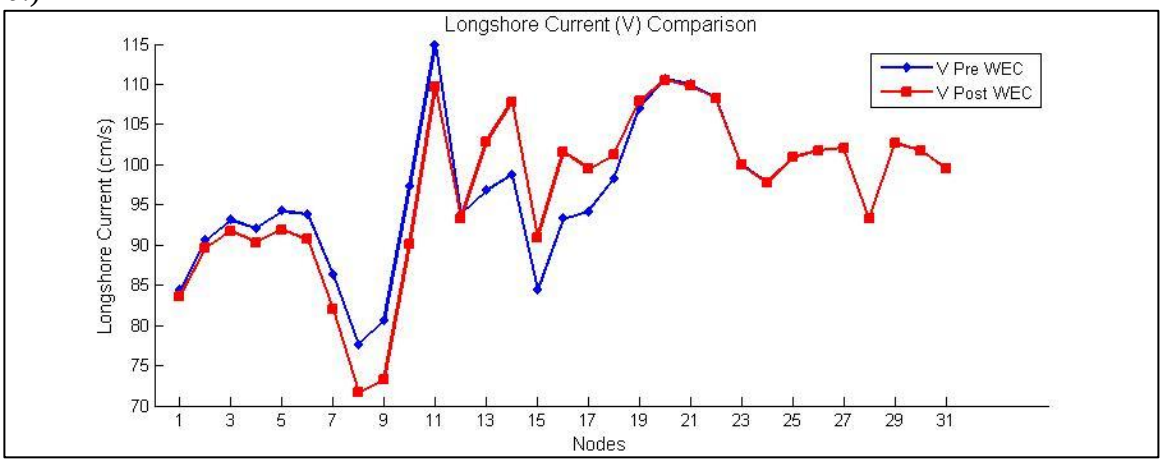

b.)

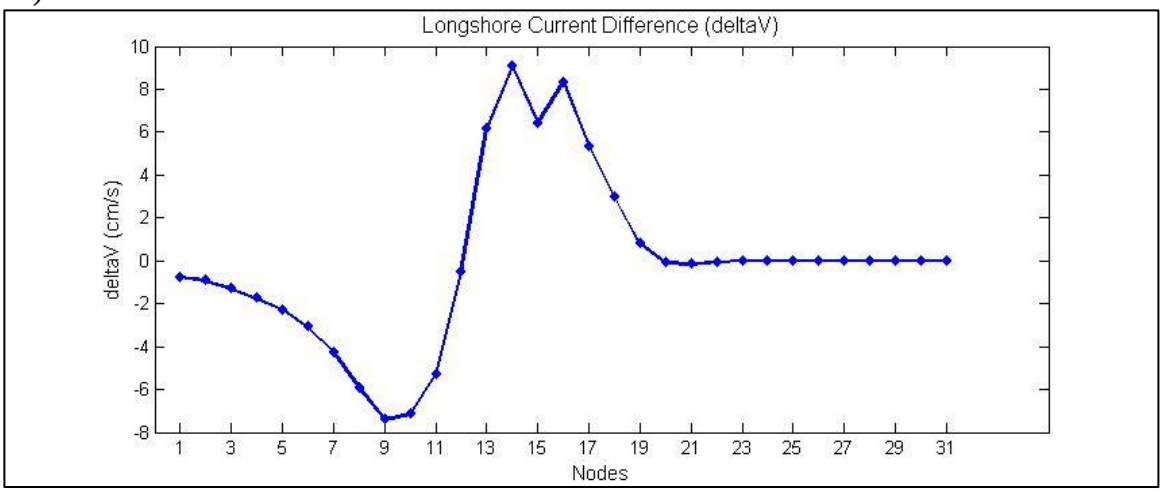

Figure III-6.18: Southeast condition results a) Longshore current distribution along nodes Pre and Post WEC array b.) ΔV at the analysis nodes

3.6.2.3. Longshore Transport

Northeast

Figure III-6.19 shows the longshore transport generated from the northeast condition pre and post WEC array and their difference at the analysis nodes. The longshore transport calculated without the influence of the WEC array oscillated about zero. The effects of the

array produce an increase in the transport rate to the south around the northern end of the array and an increase in the transport rate to the north around the southern end of the array. The maximum transport rate with the effects from the array is 1,401 cubic meters per day to the north at node 20 and 1,340 cubic meters per day to the south at node 12. As the distance away from Jennette's pier to the north and south increased, the longshore transport due to the effect of the WEC array aligned back up with the values without the array. The maximum positive and negative differences were 1,495 cubic meters per day at node 18 and -825 cubic meters per day at node 14 respectively.

a.)

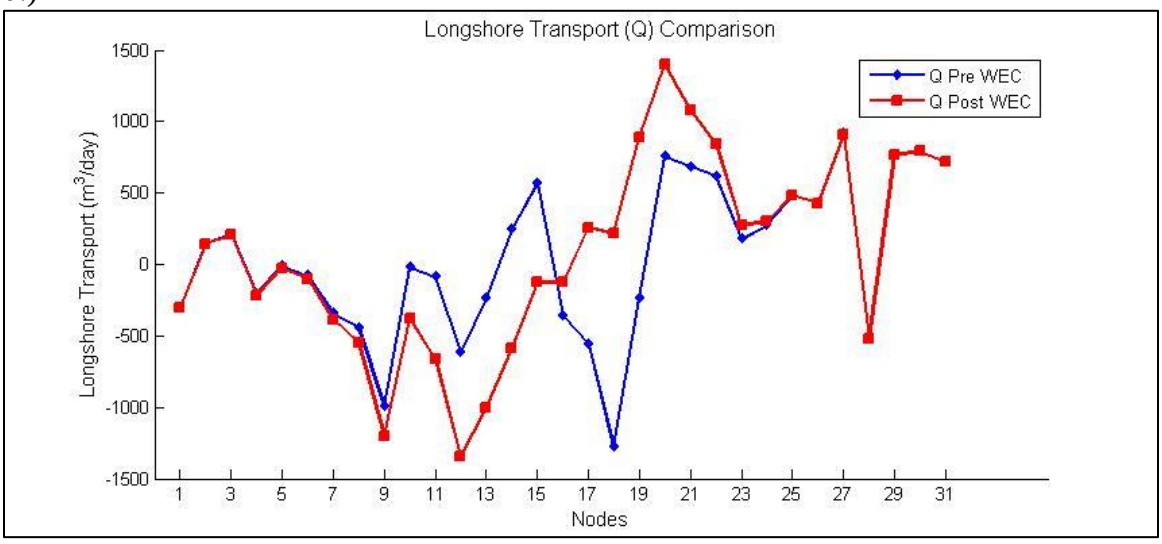

b.)

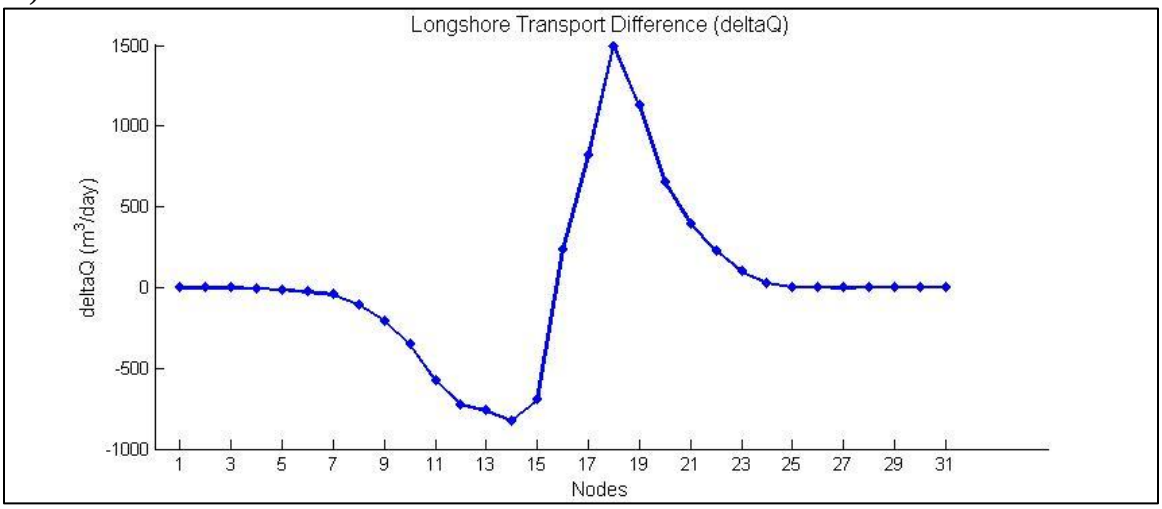

Figure III-6. 19: Northeast condition results a) Longshore transport distribution along nodes Pre and Post WEC array b.) ΔQ at the analysis nodes

East

Figure III-6.20 shows the longshore transport generated from the east condition pre and post WEC array and their difference at the analysis nodes. The longshore transport calculated without the effects of the example WEC array showed and net northward flow of sediment in this region. The maximum and minimum values of longshore transport found were 6,455

cubic meters per day at node 20 and 1,888 cubic meters per day at node 12 respectively. There was a slight increase in longshore transport around the southern end of the WEC array of 532 cubic meters per day at node 18. The majority of the influence was found around the northern end of the array. The maximum decrease was 2,217 cubic meters per day, which was located at node 12.

a.)

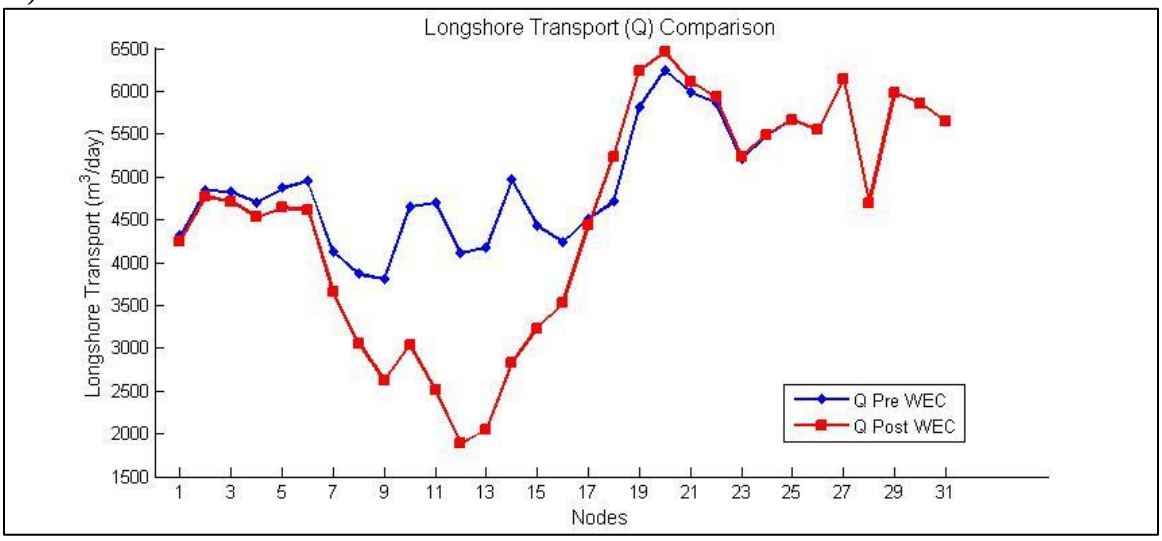

b.)

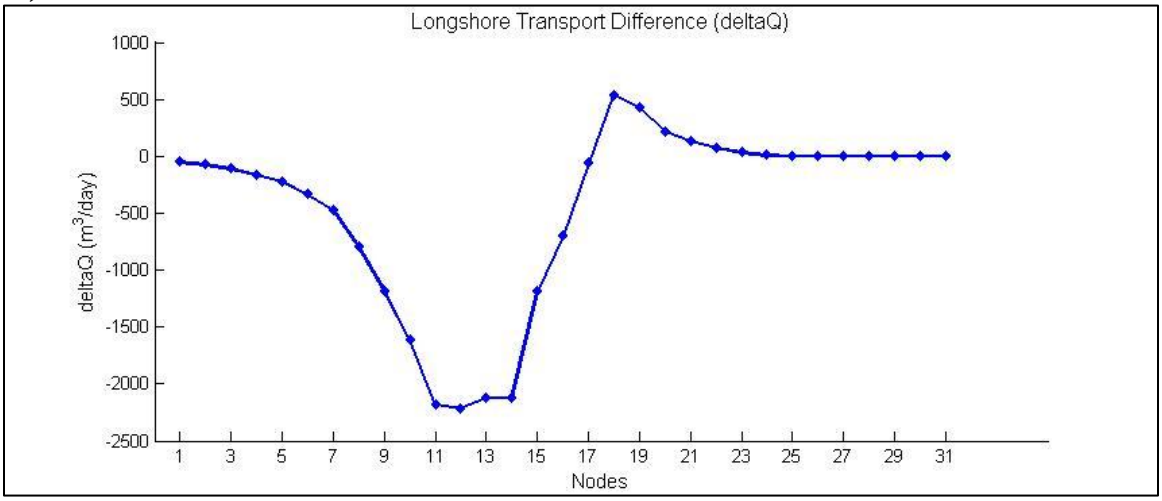

Figure III-6. 20: East condition results a) Longshore transport distribution along nodes Pre and Post WEC array b.) ΔQ at the analysis nodes

Southeast

Figure III-6.21 shows the longshore transport calculated with and without the effects from the example WEC array due to the southeast wave condition. The distribution of longshore transport produced from the east condition is similar to the southeast condition with a net north flow of sediment. The maximum and minimum values of longshore transport are 6,081 cubic meters per day at node 19 and 2,815 cubic meters per day at node 12 respectively. The laregest decrease in longshore transport was found to be 1,460 cubic meters per day and was located at node 12. For this wave condition, there was no increase in longshore transport around the southern end of the WEC array due to the high incident wave angle.

a.)

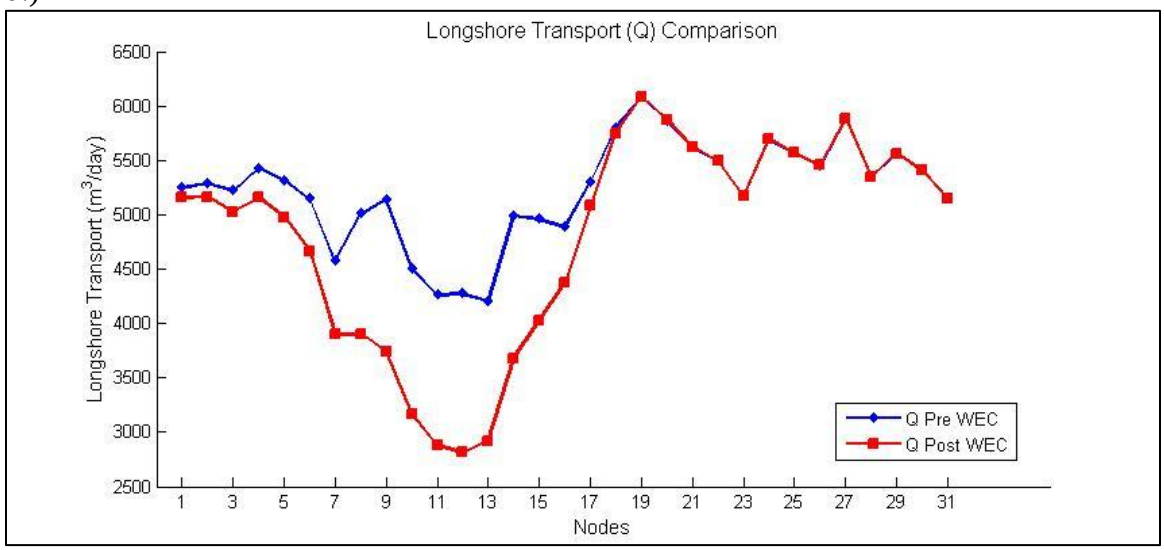

b.)

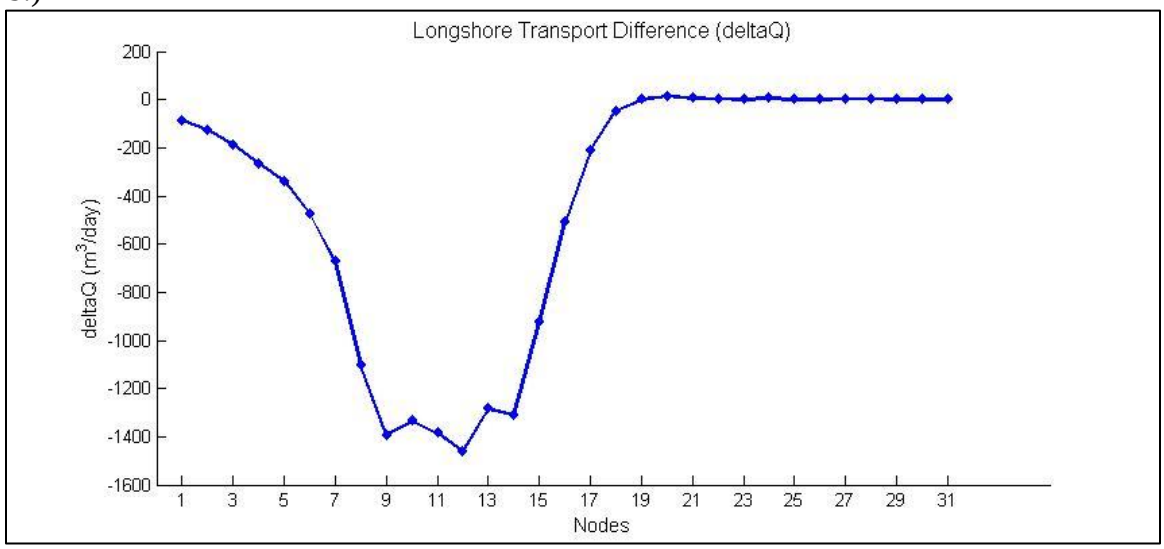

Figure III-6. 21: Southeast condition results a) Longshore transport distribution along nodes Pre and Post WEC array b.) ΔQ at the analysis nodes

3.7. Conclusion

This study has shown that there are many factors that affect coastal processes due to the deployment of a WEC array. First, the distance the WEC array is deployed offshore would have an effect on the change in wave height, longshore current, and longshore transport at the

shoreline. This was evident from the positive significant wave height gradient nearshore of the example WEC array, and the continued refraction and diffraction processes turning the wave crest more shore parallel. Therefore, if the WEC array were located farther offshore, there would be less impact on the shoreline from these three processes. The transmission coefficient assigned to each device was an estimate and can be used as a base assessment of shoreline change. If the transmission coefficient were decreased to allow only 50 percent of the wave energy through, then one could expect to see a larger decrease in wave height as well as a larger area of influence behind the example WEC array. Developers could use these results from the given transmission coefficient as a comparison to their device efficiencies as to how an array of their devices would affect coastal processes. Finally, the incident wave angle had a large effect as to the magnitude and location of the wave height, longshore current, and longshore transport change. The northeast condition had the largest percent decrease in wave height because the incident wave crest angle was parallel to the angle of the WEC array. It also produced a flow of sediment from either end of the WEC array to the center of the array. The WEC array primarily decreased the longshore transport rate with no reversal of flow for the east and southeast conditions. The southeast condition had the smallest percent decrease in wave height due to the large difference between the incident wave crest angle and the angle of the WEC array. This indicates that the best direction for the maximum energy extraction would be waves coming from the northeast. This is also the direction that will have the most impact on coastal processes. The greater the difference between the wave crest angle and the WEC array, the less effect on wave height, longshore current, and longshore transport. Overall, the effects on coastal processes from the

given WEC array are minimal and limited to the location behind the array, which should not affect this location negatively.

REFERENCES

AW-Energy. (2012, September). *Concept.* Retrieved from AW-Energy: http://www.aw-energy.com/concept.html

AW-Energy. (2012, September). *Media.* Retrieved from AW-Energy: http://www.aw-energy.com/media.html

AW-Energy. (2012, August 27). *projectSURGE blog.* Retrieved from AW-Energy: http://www.aw-energy.com/pdf/projectSURGEnews_aug2012.pdf

Battjes, J. A., & Janssen, J. P. (1978). Energy loss and set-up due to breaking of random waves. *International Conference on Coastal Engineering* (pp. 569-587). ASCE.

Bedard, R., Hagerman, G., Previsic, M., Siddiqui, O., Thresher, R., & Ram, B. (2005). *WP 009 - US Final Summary Report.*

Bedard, R., Previsic, M., Hagerman, G., Polagye, B., Musial, W., Klure, J., . . . Amsden, S. (2007). North American Ocean Energy Status - March 2007. *7th European Wave Tidal Energy Conference.*

Blanton, B. O. (2008, September 12). *Technical Reports.* Retrieved from Renaissance Computing Institute: http://www.renci.org/publications/techreports/TR-08-04.pdf

Blanton, B. O., & Luettich, R. A. (2008, September 12). *Technical Reports.* Retrieved from Renaissance Computing Institute: http://www.renci.org/wp-content/pub/techreports/TR-08-05.pdf

Booij, N., Ris, R. C., & Holthuijsen, L. H. (1999). A third-generation wave model for coastal regions 1. Model description and validation. *Journal of Geophysical Research, 104*(C4), 7649-7666.

Bouws, E., & Komen, G. J. (1983). On the Balance Between Growth and Dissipation in an Extreme Depth-Limited Wind-Sea in the Southern North Sea. *Journal of Physical Oceanography, 13*, 1653-1658.

Cavaleri, L., & Malanotte-Rizzoli, P. (1981). Wind Wave Prediction in Shallow Water: Theory and Applications. *Journal of Geophysical Research, 86*, 10961-10973.

Coastal Studies Institute. (2012, January). *Renewable Ocean Energy Program*. Retrieved from Coastal Studies Institute: http://csi.northcarolina.edu/content/research/renewableoceanenergyprogram.htm

Collins, J. I. (1972). Prediction of Shallow Water Spectra. *Journal of Geophysical Research, 77*, 2693-2707.

Dean, R. G., & Dalrymple, R. A. (1991). *Water Wave Mechanics for Engineers and Scientists.* World Scientific Publishing Co.

Dean, R. G., & Dalrymple, R. A. (2002). *Coastal Processes with Engineering Applications.* Cambridge, United Kingdom: Cambridge University Press.

Dean, R. G., Chen, R., & Browder, A. E. (1997). Full scale monitoring study of a submerged breakwater, Palm Beach, Florida, USA. *Coastal Engineering*, *29*, 291-315.

del Valle, R., Medina, R., & Losada, M. A. (1993). Dependence of Coefficient K on Grain Size. *Journal of Waterway, Port, Coastal, and Ocean Engineering*, *119*(5), 568-574.

Elderberky, Y., & Battjes, J. A. (1996). Spectral modeling of wave breaking: Application to Boussinesq equations. *Journal of Geophysical Research, 101*, 1253-1264.

European Marine Energy Centre. (2012, February 11). *Wave Developers*. Retrieved from EMEC Orkney: http://www.emec.org.uk/marine-energy/wave-developers/

Evans, D. V. (1976). A theory for wav-power absorption by oscillating bodies. *Journal of Fluid Mechanics, 77*, 1-25.

Falcao, A. F. (2010). Wave energy utilization: A review of the technologies. *Renewable and Sustainable Energy Reviews, 14*(3), 899-918.

Folley, M., & Whittaker, T. J. (2009). Analysis of the nearshore wave energy resource. *Renewable Energy, 34*, 1709-1715.

Folley, M., Whittaker, T. J., & Henry, A. (2007). The effect of water depth on the performance of a small surging wave energy converter. *Ocean Engineering, 34*, 1265-1274.

Folley, M., Whittaker, T., & Henry, A. (2005). The Performance of a Wave Energy Converter in Shallow Water. *6th European Wave and Tidal Energy Conference.* Glasgow.

Hasselmann, K. (1974). On the spectral dissipation of ocean waves due to whitecapping. *Boundary-Layer Meterology, 6*, 107-127.

Hasselmann, K., Barnett, T. P., Bouws, E., Carlson, H., Cartwright, D. E., Enke, K., . . . Walden, H. (1973). Measurements of wind-wave growth and swell decay during the Joint North Sea Wave Project (JONSWAP). *Ergnzungsheft zur Deutschen Hydrographischen Zeitschrift Reihe, 8*(12).

Hasselmann, S., Hasselmann, K., Allender, J. H., & Barnett, T. P. (1985). Computations and Parameterizations of the Nonlinear Energy Transfer in a Gravity-Wave Spectrum. Part II: Parameterizations of the Nonlinear Energy Transfer for Application in Wave Models. *Journal of Physical Oceanography*, 1378-1391.

Holthuijsen, L. H., Herman, A., & Booij, N. (2003). Phase-decoupled refraction-diffraction for spectral wave models. *Coastal Engineering*, 291-305.

Janssen, P. A. (1991). Quasi-linear Theory of Wind-Wave Generation Applied to Wave Forecasting. *Journal of Physical Oceanography, 21*, 1631-1642.

Kamphuis, J. W. (2010). *Introduction to Coastal Engineering and Management.* Singapore: World Scientific Publishing Co.

Komen, G. J., Hasselmann, S., & Hasselmann, K. (1984). On the Existence of a Fully Developed Wind-Sea Spectrum. *Journal of Physical Oceanography, 14*, 1271-1285.

Longuet-Higgins, M. S. (1970). Longshore Currents Generated by Obliquely Incident Sea Waves,1. *Journal of Geophysical Research*, 6778-6789.

Madsen, O. S., Poon, Y. K., & Graber, H. C. (1988). Spectral wave attenuation by bottom friction: Theory. *International Conference on Coastal Engineering* (pp. 492-504). ASCE.

McCowan, J. (1891). VII. On the solitary wave. *Philosophical Magazine Series 5, 32*(194), pp. 45-58.

Millar, D. L., Smith, H., & Reeve, D. E. (2007). Modelling analysis of the sensitivity of shoreline change to a wave farm. *Ocean Engineering, 34*(5-6), 884-901.

Nicholls, R. J., Birkemeier, W. A., & Lee, G.-h. (1998). Evaluation of depth of closure using data from Duck, NC, USA. *Marine Geology, 148*, 179-201.

Ocean Power Technologies. (2012). *Completed Projects: Scotland*. Retrieved from Ocean Power Technologies: http://www.oceanpowertechnologies.com/scotland.html

Ocean Power Technologies. (2012, February). *Products.* Retrieved from Ocean Power Technologies: http://www.oceanpowertechnologies.com/PDF/PB150_February2012.pdf

Oskamp, J. A., & Ozkan-Haller, H. T. (2010). Wave Predictions at the Site of a Wave Energy Conversion Array. *Proc. of 32nd International Conference on Coastal Engineering* (pp. 1-8). Shanghai: World Scientific.

Pelamis Wave Power. (2012, 2 10). *Downloads.* Retrieved from Pelamis Wave Power Ltd.: http://www.pelamiswave.com/upload/document/PWP-brochure-online.pdf

Pierson, W. J., & Moskowitz, L. (1964). A Proposed Spectral Form for Fully Developed Wind Seas Based on the Similarity Theory of S. A. Kiitaigorodskii. *Journal of Geophysical Research, 69*(24), 5181-5190.

Resolute Marine Energy. (2012, September). *News*. Retrieved from Resolute Marine Energy: http://www.resolutemarine.com/news/u-s-commerce-department-selects-rme-to-participate-in-south-african-trade-mission

Ris, R. C., Holthuijsen, L. H., & Booij, N. (1999). A third-generation wave model for coastal regions 2. Verification. *Journal of Geophysical Research, 104*, 7667-7681.

Sanchez-Arcilla, A., Gironella, X., Verges, D., Sierra, J. P., Pena, C., & Moreno, L. (2000). Submerged Breakwaters and "Bars". From Hydrodynamics to Functional Design. *27th International Conference on Coastal Engineering. 2*, pp. 1821-1835. Sydney: ASCE.

Snyder, R. L., Dobson, F. W., Elliott, J. A., & Long, R. B. (1981). Array measurement of atmospheric pressure fluctuations above surface gravity waves. *Journal of Fluid Mechanics, 102*, 1-59.

Sumer, B. M., & Fredsoe, J. (2002). *The Mechanics of Scour in the Marine Environment.* New Jersey: World Scientific.

Sumer, B. M., Whitehouse, R. J., & Torum, A. (2001). Scour around coastal structures: a summary of recent research. *Coastal Engineering, 44*, 153-190.

The Royal Academy of Engineering. (2004). The Costs of Generating Electricity. London: The Royal Acadamy of Engineering.

The SWAN team. (2012, September). *Spectral action balance equation*. Retrieved from Scientific and Technical Documentation SWAN Cycle III version 40.91: http://swanmodel.sourceforge.net/online_doc/swantech/node12.html

U.S. Army Corps of Engineers. (2002). *Coastal Engineering Manual 11100-2-1100.* Washington, D.C.: U.S. Army Corps of Engineers.

U.S. Department of Energy. (2012, March). *Electricity*. Retrieved from U.S. Energy Information Administration: http://www.eia.gov/electricity/sales_revenue_price/index.cfm

US Army Corps of Engineers. (2011, February). *Wave Information Studies*. Retrieved from http://wis.usace.army.mil/

US Army Corps of Engineers. (2012, March 11). *Data*. Retrieved from Field Research Facility: http://www.frf.usace.army.mil/waverdr630/realtime.shtml

US Army Corps of Engineers. (2012, March 1). *FRF Surveys*. Retrieved from http://www.frf.usace.army.mil/survey/frfsurvey.html

van den Berg, J., Ricci, P., Santos, M., Rico, A., & Lopez, J. (2010). Hydrodynamic performance of heaving wave energy converters in wave climates. *3rd International Conference on Ocean Energy.* Bilbao, Spain.

Wesseling, P. (1992). *An introduction to multigrid methods.* Chichester: John Wiley and Sons.

Whittaker, T., Collier, D., Folley, M., Osterried, M., Henry, A., & Crowley, M. (2005). The development of Oyster - A shallow water surging wave energy converter. *7th Annual European Wave & Tidal Conference.* Porto.

Zijlema, M., & van der Westhuysen, A. J. (2005). On convergence behaviour and numerical accuracy in stationary SWAN simulation of nearshore wind wave spectra. *Coastal Engineering*, 237-256.